

THESIS FOR THE DEGREE OF DOCTOR OF PHILOSOPHY

Characterization of MIMO Antennas and Terminals: Measurements in Reverberation Chambers

Xiaoming Chen



CHALMERS

Antenna Group
Department of Signals and Systems
Chalmers University of Technology
SE-41296 Gothenburg, Sweden

Gothenburg, 2012

Characterization of MIMO Antennas and Terminals: Measurements in Reverberation Chambers

Xiaoming Chen

ISBN 978-91-7385-679-9

@ XIAOMING CHEN, 2012.

Doktorsavhandlingar vid Chalmers tekniska högskola

Ny serie nr 3360

ISSN 0346-718X

Antenna Group

Department of Signals and Systems

Chalmers University of Technology

SE-412 96 Gothenburg, Sweden

Telephone: +46 (0) 31 772 1000

Printed in Sweden by Chalmers Reproservice
Gothenburg, Sweden, April 2012.

To my family

Abstract

The reverberation chamber (RC) has drawn considerable attention as a multipath emulator over the past decade for both passive and active over-the-air (OTA) tests. This thesis is about RCs for OTA applications. The overview of this thesis is given in Chapter 1.

Although the main purpose of this thesis is characterizations of MIMO (multiple-input multiple-output) terminals based on RC measurements, it is of importance to know under which channel condition the device under test (DUT) has been measured. Parameters that are used to characterize the channel in a multipath environment are coherence bandwidth, delay spread, coherence time, Doppler spread, coherence distance and angular spread. In a normal RC, the angular of arrival (AoA) distribution is almost uniform. The corresponding coherence distances for different antennas can be derived readily based on the a priori knowledge of the uniform angular distribution. Therefore, the main tasks of RC channel characterizations are to determine the channel's coherence bandwidth, RMS delay spread, coherence time and Doppler spread. These studies are presented in Chapter 2.

For multi-port antennas used in MIMO systems, relevant characterization parameters are correlation, embedded radiation efficiency, diversity gain, and MIMO capacity, all of which can be measured in a RC. In order to compare a RC measurement with that of an anechoic chamber (AC), two methods for evaluations of AC measurement-based maximum ratio combining (MRC) diversity gain and MIMO capacity are presented correspondingly. After examining these two methods, they are applied, respectively, to a wideband multi-port antenna that is measured in both AC and RC. Comparisons show good agreements. Furthermore, a throughput measurement of a LTE (long term evolution) dongle is tested in the RC. A corresponding throughput model is presented. Simple as it is, this model can well predict the measurement result. All of these are studied in Chapter 3.

For both passive and active OTA tests, the measurement accuracy is of great importance. Previous RC measurement uncertainty work believed that the RC accuracy depends only on the independent sample number. This thesis, however, shows that the RC accuracy depends not only on the independent sample number, but also on the Rician K-factor, i.e. the power ratio of unstirred electromagnetic (EM) fields to the stirred ones, and that the K-factor represents a residual error in RC measurements. It is also proven using two RCs that accuracy can be improved either by reducing the K-factor or by introducing stirring methods that reduce it, such as platform and polarization stirring. These studies are presented in Chapter 4.

Chapter 5 concludes this thesis.

Keywords: Reverberation chamber (RC), channel characterization, maximum ratio combining (MRC) diversity gain, multiple-input multiple-output (MIMO) capacity, measurement uncertainty.

Contents

| | |
|---|------------|
| Abstract | i |
| Contents | iii |
| List of Publications | v |
| Acknowledgement | ix |
| Abbreviations and Notations | xi |
| 1. Overview | 1 |
| 1.1 Channel Characterizations | 1 |
| 1.2 Measurements of MIMO Terminals | 1 |
| 1.3 Measurement Uncertainty Characterizations | 2 |
| 2. Channel Characterizations | 3 |
| 2.1 Coherence Bandwidth and Delay Spread | 4 |
| 2.2 Average Mode Bandwidth and Decay Time | 7 |
| 2.3 Doppler Spread | 9 |
| 3. Measurements of MIMO Terminals | 13 |
| 3.1 Measurement of Single-Port Antenna | 13 |
| 3.2 Diversity Gain Evaluation | 17 |
| 3.2.1 Covariance-Eigenvalue Approach | 17 |
| 3.2.2 Eleven Antenna under Test | 22 |
| 3.2.3 RC and AC Measurements | 23 |
| 3.2.4 Measurement Results | 24 |
| 3.3 MIMO Capacity Evaluation | 27 |
| 3.3.1 Embedded Far-Field Function Method | 28 |
| 3.3.2 Comparison with Z-Parameter Method | 29 |
| 3.3.3 S-Parameter Method | 31 |
| 3.3.4 RC and AC Measurement Results | 33 |
| 3.4 Throughput Measurement | 38 |
| 4. Measurement Uncertainty Characterizations | 41 |
| 4.1 Procedure of Uncertainty Assessment | 41 |
| 4.2 Uncertainty Model | 41 |
| 4.2.1 Stirred Fields and Independent Sample Number | 42 |
| 4.2.2 Unstirred Fields and Average K-factor | 44 |
| 4.3 Measurements and Results | 45 |
| 5. Conclusions | 54 |
| Appendix A | 56 |
| Appendix B | 60 |
| Appendix C | 63 |
| Appendix D | 65 |
| References | 67 |

List of Publications

This thesis is based on the following publications (but only Papers A-E are appended to this thesis):

Journal Papers:

- A. X. Chen, P.-S. Kildal, J. Carlsson, and J. Yang, "MRC diversity and MIMO capacity evaluations of multi-port antennas using reverberation chamber and anechoic chamber," Submitted to IEEE Transactions on Antennas and Propagation, April, 2012.
- B. X. Chen, P.-S. Kildal, and S.-H. Lai, "Estimation of average Rician K-factor and average mode bandwidth in loaded reverberation chamber," IEEE Antennas and Wireless Propagation Letters, vol. 10, pp. 1437-1440, 2011.
- C. X. Chen, P.-S. Kildal, and J. Carlsson, "Fast converging measurement of MRC diversity gain in reverberation chamber using covariance-eigenvalue approach," IEICE Transactions on Electronics, vol. E94-C, no.10, pp.1657-1660, Oct. 2011. (Special Section on Microwave and Millimeter-Wave Technology.)
- D. X. Chen, P.-S. Kildal, J. Carlsson, and J. Yang, "Comparison of ergodic capacities from wideband MIMO antenna measurements in reverberation chamber and anechoic chamber," IEEE Antennas and Wireless Propagation Letters, vol. 10, pp. 446-449, 2011.
- E. X. Chen, P.-S. Kildal, C. Orlenius, and J. Carlsson, "Channel sounding of loaded reverberation chamber for Over-the-Air testing of wireless devices - coherence bandwidth and delay spread versus average mode bandwidth," IEEE Antennas and Wireless Propagation Letters, vol. 8, pp. 678-681, 2009.
- F. P.-S. Kildal, X. Chen, C. Orlenius, M. Franzén, and C. Lötbäck Patané, "Characterization of reverberation chambers for OTA measurements of wireless devices: physical formulations of channel matrix and new uncertainty formula", accepted for publication in IEEE Transactions on Antennas and Propagation, 2012.
- G. P.-S. Kildal, A. Hussain, X. Chen, C. Orlenius, A. Skårbratt, J. Asberg, T. Svensson, and T. Eriksson, "Threshold receiver model for throughput of wireless devices with MIMO and frequency diversity measured in reverberation chamber," IEEE Antennas and Wireless Propagation Letters, vol. 10, pp. 1201-1204, 2011.
- H. K. Karlsson, X. Chen, P.-S. Kildal, and J. Carlsson, "Doppler spread in reverberation chamber predicted from measurements during step-wise stationary stirring," IEEE Antennas and Wireless Propagation Letters, vol. 9, pp. 497-500, 2010.
- I. J. Yang, X. Chen, N. Wadefalk, and P.-S. Kildal, "Design and realization of a linearly polarized Eleven feed for 1-10 GHz," IEEE Antennas and Wireless Propagation Letters, vol.8, pp. 64-68. 2009.

Selected Conference Papers:

- J. X. Chen, P.-S. Kildal, J. Carlsson, and J. Yang, "Capacity characterization of Eleven antenna in different configurations for MIMO applications using reverberation chamber," 6th European Conference on Antennas and Propagation, Prague, Czech, 26-30 Mar. 2012.
- K. X. Chen, P.-S. Kildal, and J. Carlsson, "Measurement uncertainties of capacities of multi-antenna system in anechoic chamber and reverberation chamber," 8th International Symposium on Wireless Communication Systems, Aachen, Germany, 6 - 9 Nov., 2011, pp. 216-220.
- L. X. Chen, P.-S. Kildal, and J. Carlsson, "Simple calculation of ergodic capacity of lossless two-port antenna system using only S-parameters – Comparison with Common Z-parameter approach," 2011 IEEE International Symposium on Antennas and Propagation, Spokane, USA, 3-8 July, 2011, pp. 1885-1888.
- M. X. Chen, P.-S. Kildal, and J. Carlsson, "Determination of maximum Doppler shift in reverberation chamber using level crossing rate," 5th European Conference on Antennas and Propagation, Rome, Italy, 11-15 April 2011, pp. 62-65.
- N. X. Chen, P.-S. Kildal, and J. Carlsson, "Comparisons of different methods to determine correlation applied to multi-port UWB Eleven antenna," 5th European Conference on Antennas and Propagation, Rome, Italy, 11-15 April 2011, pp. 1776-1780.
- O. X. Chen, P.-S. Kildal, and J. Carlsson, "Spatial correlations of incremental sources in isotropic environment such as reverberation chamber," 5th European Conference on Antennas and Propagation, Rome, Italy, 11-15 April 2011, pp. 1753-1757.
- P. X. Chen and P.-S. Kildal, "Frequency-dependent effects of platform and wall antenna stirring on measurement uncertainty in reverberation chamber," 4th European Conference on Antennas and Propagation, Barcelona, Spain, 12-16 April 2010.
- Q. X. Chen and P.-S. Kildal, "Comparison of RMS delay spread and decay time measured in reverberation chamber," 4th European Conference on Antennas and Propagation, Barcelona, Spain, 12-16 April 2010.
- R. X. Chen and P.-S. Kildal, "Accuracy of antenna mismatch factor and input reflection coefficient measured in reverberation chamber," 3rd European Conference on Antennas and Propagation, 23-27 March 2009, Berlin, Germany, pp. 2678-2681.
- S. X. Chen and P.-S. Kildal, "Theoretical derivation and measurements of the relationship between coherence bandwidth and RMS delay spread in reverberation chamber," 3rd European Conference on Antennas and Propagation, 23-27 March 2009, Berlin, Germany, pp. 2687-2690.

Preface

This report is a thesis for the degree of Doctor of philosophy at Chalmers University of Technology, Gothenburg, Sweden. The thesis is divided into three main parts: channel characterizations, measurements of MIMO terminals, and measurement uncertainty characterizations, all in reverberation chambers. This work has been supported by the Swedish Governmental Agency for Innovation Systems (VINNOVA) within the VINN Excellence Centre Chase at Chalmers. My main supervisor is Prof. Per-Simon Kildal, who is also the examiner; my additional supervisors are Prof. Jan Carlsson and Assoc. Prof. Jian Yang. The work was carried out between January 2008 and May 2012 at the antenna group of Chalmers University of Technology.

Acknowledgement

First of all, I would like to thank my supervisor (and examiner) Prof. Per-Simon Kildal for accepting me into his group. In spite of his busy schedule, we had fruitful discussions, which eventually lead to this PhD thesis. I am also grateful for the nice antenna group ski trips that he organized. I would also like to thank my secondary supervisor, Prof. Jan Carlsson, for his constant interests and support in my work. Special thanks also go to my additional supervisor, Assoc. Prof. Jian Yang, who is always willing to help throughout my PhD study.

I am also indebted to current and past members of the antenna group, Ulf Carlberg, Yogesh Karandikar, Ashraf Zaman, Elena Pucci, Ahmed Hussain, Hasan Raza, Astrid Algaba Brazález, Eva Rajo-Iglesias, Esperanza Alfonso, Erik Geterud, Oleg Iupikov, Aidin Razavi, Nima Jamaly, Rob Maaskant, and Marianna Ivashina, for making the group a great place to work in. I am also grateful to my friends outside the antenna group, who bring many joys into my daily life.

I would like to thank Assoc. Prof. Buon Kiong (Vincent) Lau and Prof. Anja Skrivervik for their careful pre-inspection and helpful suggestions to improve the quality of this thesis.

The work in this thesis has been supported by The Swedish Governmental Agency for Innovation Systems (VINNOVA) within the VINN Excellence Center Chase. I would like to thank all the participants in the former MIMO terminals and OTA projects within the Chase VINN Excellence Center, for their interest and amicable attitude to my project presentations. Special thanks go to Dr. Kristian Karlsson at SP, Mats Kristoffersen, Magnus Franzén, and Charlie Orlenius at Bluetest AB, for their technique supports.

Last but not least, I would like to thank my wife and parents for their love and support.

Abbreviations and Notations

Abbreviations

AC: Anechoic Chamber
ACF: Autocorrelation function
AoA: Angle of Arrival
AUT: Antenna Under Test
ARQ: Automatic Repeat Request
BER: Bit Error Rate
CDF: Cumulative Distribution Function
CFO: Carrier Frequency Offset
CRB: Cramer-Rao Bound
CSI: Channel State Information
DUT: Device Under Test
EDG: Effective Diversity Gain
EGC: Equal Gain Combining
EM: Electromagnetic
EMC: Electromagnetic Compatibility
IF: Intermediate Frequency
IFFT: Inverse Fourier Transform
i.i.d.: Independent Identically Distributed
LS: Least Squares
LTE: Long Term Revolution
MIMO: Multiple-Input Multiple-Output
MISO: Multiple-Input Single-Output
ML: Maximum Likelihood
MRC: Maximum Ratio Combining
MRT: Maximum Ratio Transmission
MVU: Minimum Variance Unbiased
o.c.: Open Circuit
OFDM: Orthogonal Frequency Division Multiplexing
OTA: Over The Air
PDF: Probability Density Function
PDP: Power Delay Profile
PSD: Power Spectrum Density
PVC: Polyvinyl Chloride
RC: Reverberation Chamber
RMS: Root Mean Square
SC: Selection Combining
SIMO: Single-Input Multiple-Output
SISO: Single-Input single-Output
SNR: Signal-To-Noise Ratio
STD: Standard Deviation
US: Uncorrelated Scattering
VNA: Vector Network Analyzer
WSS: Wide Sense Stationary

Notations

B_c : Coherence Bandwidth
 C : Capacity
 \mathbf{e} : Embedded Radiation Efficiency Vector
 E : Mathematical Expectation
 e_{emb} : Embedded Radiation Efficiency
 e_{rad} : Radiation Efficiency
 e_{ref} : Radiation Efficiency of the Reference Antenna
 f : Frequency
 f_d : Doppler Frequency Shift
 F : CDF
 h : Channel Impulse Response
 \mathbf{h} : Channel vector
 H : Channel Transfer Function
 \mathbf{H} : Channel Matrix
 \mathbf{H}_w : Spatially White Channel Matrix
 \mathbf{I} : Identity Matrix
 \mathbf{g} : Embedded Far-File Function Vector
 G_{ref} : Average Power Transfer Function of the Reference Antenna
 K_{av} : Average Rician K-factor
 \ln : Natural Logarithm
 \log : Logarithm
 N_{ind} : Independent Sample Numbers
 p : PDF
 Q : Quality Factor
 \mathbf{R} : Covariance Matrix
 R_f : Frequency ACF
 R_t : Time ACF
 S_d : Doppler Spectrum
 t : Time
 T_c : Coherence Time
 τ : Delay
 ρ : Correlation Coefficient
 γ : SNR
 λ : Eigenvalue
 λ_c : Wavelength
 σ : STD
 σ_τ : RMD Delay Spread
 σ_d : RMD Doppler Spread
 Δf : Mode Bandwidth
 Ω : Solid Angle
 Φ : Correlation Coefficient Matrix
 ϕ : Characteristic Function

1. Overview

Multi-antenna systems have received considerable attention over the past decade due to their performance-enhancement capability in multipath environments [1]-[6]. Lots of studies have been carried out for measuring diversity gains and multiple-input multiple-output (MIMO) capacities of multi-antenna systems in real-life (outdoor and indoor) multipath environments [7]-[11]. As opposed to real-life measurements, reverberation chambers (RCs) are being considered for the standardization of over-the-air (OTA) measurements of MIMO terminals due to their fast, repeatable, and cost-effective measurements [12]-[14]. A RC is basically a metal cavity whose electromagnetic modes are stirred (by mechanical mode-stirrers) to emulate multipath fading environments [12]. RCs were traditionally used for electromagnetic compatibility (EMC) tests, but during the past decade they have found new applications in the characterizations of small antennas and wireless devices in multipath environments. The diversity gains and MIMO capacities of multi-antenna systems have been measured in RCs [13]-[24]. RCs have also been used to measure active MIMO terminals [21]-[24]. The Antenna group at Chalmers University of Technology (Chalmers for short) together with a spinoff company, Bluetest AB, has dedicated significant effort in developing reverberation chambers for OTA tests of wireless devices. Former PhD students in the group, Kent Rosengren, Ulf Carlberg, Kristian Karlsson and Daniel Nyberg had all worked on topics related to RCs. This thesis is a further study of RCs based on previous knowledge, especially on Rosengren's works [14]. This thesis consists of three main parts: channel characterizations, MIMO terminal measurements, and measurement uncertainty characterizations.

1.1 Channel Characterizations

For active OTA measurements, it is of importance to know under which channel condition the device under test (DUT) is measured. Parameters that are used to characterize channels in multipath environments are coherence bandwidth, delay spread, coherence time, Doppler spread, coherence distance and angular spread [6]. The coherence distance can be determined easily based on the a priori knowledge of the angular distribution of incident waves and embedded radiation patterns of the antennas [25]. Normally, in an unloaded RC, the angular distribution is three-dimensionally uniform (or isotropic) [14]. Therefore, determination of coherence distance in the RC only requires straightforward calculation once the antenna radiation patterns are known. The coherence bandwidth and the root-mean-square (RMS) delay spread in RCs have been studied in [25]-[29]. The Doppler spread (which is inversely proportional to coherence time) in RCs were studied in [30], [31]. It is well known that the channel in an unloaded and well-stirred RC is Rayleigh distributed [12]. By loading the RC, it is possible to have Rician fading [32]-[34]. The deviation from Rayleigh to Rician is measured by the (Rician) K-factor. However, it is shown in [35] that the K-factor represents a residual error for a stochastic RC measurement. Therefore, large K-factors (heavy loading) should be avoided in order to have an acceptable measurement uncertainty.

1.2 Measurements of MIMO Terminals

For a passive single-port antenna measurement in a RC, the radiation efficiency and the free-space mismatch factor are of interest. For a MIMO antenna measurement in a RC, correlation,

embedded radiation efficiency, diversity gain, and MIMO capacity are of interest. This thesis focuses on the maximum-ratio-combining (MRC) diversity gain and the ergodic MIMO capacity for the characterization of MIMO antennas. In addition to RC measurements, via which they can be readily calculated, it is also possible to evaluate the MRC diversity and the MIMO capacity based on the measured embedded radiation efficiency and far-field function at each antenna port in an anechoic chamber (AC) [18]. In this thesis, comparisons of diversity gains and MIMO capacities between RC and AC measurements are made. Good agreements are observed. In addition, single-input multiple-output (SIMO) and multiple-input single-output (MISO) throughput measurements are conducted and studied using RC measurements. A simple throughput model is presented, which agrees well with the measurement results [21].

1.3 Measurement Uncertainty Characterizations

For passive diversity and capacity measurements and active OTA measurements, we need to have an accurate estimation of the power level (or path loss) in the RC. Therefore, it is important to characterize the accuracy of the power level measured in the RC. The power level is basically an average (over all channel samples) power transfer function. It is well known from elementary statistics that a large number of independent samples are necessary for good measurement accuracies. However, the maximum number of independent electromagnetic (EM) modes in a RC is physically limited by the volume of the RC and the effectiveness of the mode-stirrers inside the RC [36]. As mentioned earlier, it is found that the K-factor in RC represents a residual error for the measurement accuracy. As pointed out in [35], loading the RC results in an increased K-factor, and therefore an increased measurement uncertainty. Based on this observation, the RC was redesigned (at Bluetest AB) to reduce the average K-factor. The resulting measurement accuracy is improved.

These three parts are studied in details in the following three chapters, respectively.

2. Channel Characterizations

As mentioned in Section 1.1, channel characterizations in RCs involve determining the coherence bandwidth and the Doppler spread, while the delay spread and the coherence time are just their inverses, respectively. Note that determination of the (Rician) K-factor also falls into the scope of channel characterizations. However, due to its strong relation with the RC measurement uncertainty (cf. Section 1.3), K-factor evaluations are deferred till Chapter 4. Before jumping into the different channel parameters, it is instructive to discuss the appropriate channel model for a RC. Since the RC emulates a reference (Rayleigh or Rician) fading environment and the goal is to find a suitable channel model for the RC, the literature survey here is rather limited. Interested readers are suggested to refer to [37], [38] (and references therein) for more information on channel models. Furthermore, for heuristic purposes, only the single-input single-output (SISO) channel is considered in this chapter. The extension from SISO to MIMO channel characterizations (in terms of the coherence bandwidth and the Doppler spread) is straightforward. The spatial correlation in a RC has been studied extensively in [25], [39]-[41]. In this thesis, the spatial correlation of the MIMO channel is studied in the form of correlations of practical multi-port antennas (that is deferred till Chapter 3).

The underlying physical phenomenon of wireless communications is wave propagation. Maxwell's equations provide a general and elegant model for the propagating waves in any given space. Nevertheless, to compute the solution of Maxwell's equations for a real-life environment requires enormous amount of information on the boundary conditions, which makes it rather difficult (if not impractical). An intuitive approach to simplify the EM problem is the discrete-tap fading model [42],

$$h(\tau) = \sum_{l=0}^{L-1} \alpha_l \delta(\tau - \tau_l) \quad (2.1)$$

where h is the channel impulse response, L is the number of equivalent channel taps, α_l and τ_l ($l = 1, \dots, L-1$) are the complex channel tap coefficients and tap delays, respectively. Although (2.1) is not mathematically rigorous due to the fact of finite (frequency) bandwidth in reality, it is accurate enough for modeling the channel inside a RC. Using the Saleh-Valenzuela model [43], which is a slight modification of (2.1), it is possible to model more complicated channels such as those emulated using the combination of a RC and an AC [29].

The channel in a RC can be approximated as a wide sense stationary (WSS) uncorrelated scattering (US) random process. Based on Bello's seminal work [44] (the extension of Bello's work to angular spread and coherence distance can be found in [45]), together with the WSSUS assumption, interesting relations between the coherence bandwidth B_c (coherence time T_c) and the delay spread σ_τ (Doppler spread σ_d) can be readily derived:

$$B_c \propto 1/\sigma_\tau, \quad \sigma_d \propto 1/T_c. \quad (2.2)$$

The definitions of these parameters are given in the following sections.

2.1 Coherence Bandwidth and Delay Spread

The coherence bandwidth B_c is defined, in this thesis, as the frequency range over which the magnitude of the normalized autocorrelation function (ACF) of the (complex) signal is larger than 0.5. See Fig. 2.1 for the illustration. In the literature there are other definitions for the coherence bandwidth [6], [46]-[51]. For example, a threshold of 0.7 is used [6] instead of 0.5; the ACF of the envelope of the signal is used [46] instead of using the complex ACF of the complex signal; the full-bandwidth is used [50] instead of using the half-bandwidth. In this thesis, the coherence bandwidth means the half-bandwidth coherence bandwidth based on the magnitude of the complex ACF with a threshold of 0.5, as shown in Fig. 2.1, unless otherwise specified.

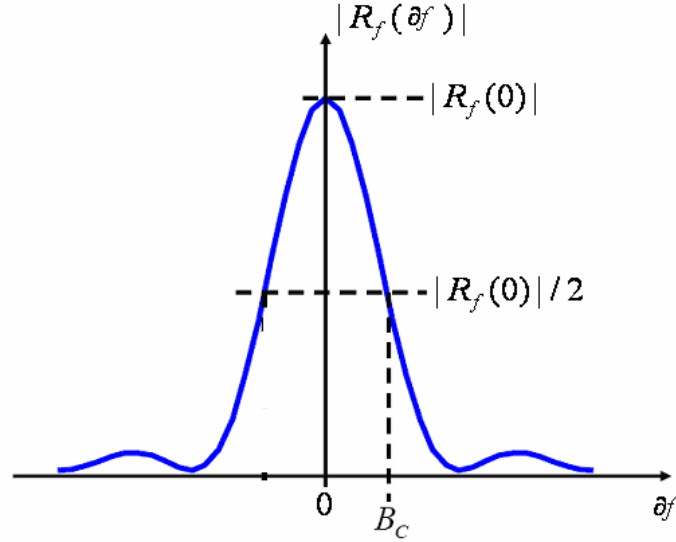


Figure 2.1: Illustration of coherence bandwidth based on signal ACF.

Different coherence bandwidths (in a RC) with different thresholds are related via the following formula:

$$B_c = \frac{1}{2\pi\sigma_r} \sqrt{\frac{1-|\rho|^2}{|\rho|^2}} \quad (2.3)$$

where ρ denotes the autocorrelation coefficient of the signal (see Appendix A for its derivation). Generalized relations of the coherence bandwidth and the delay spread for various real-life multipath environments can be found in [52] (and references therein). Note that it is shown in Appendix A that the envelope autocorrelation coefficient equals to the squared magnitude of the autocorrelation coefficient.

In the following of this section, the coherence bandwidth and the delay spread of the RC channel are presented based on RC measurements.

The RC in use here is the Bluetest HP reverberation chamber (see Fig. 2.2) with dimensions of $1.80 \times 1.75 \times 1.25 \text{ m}^3$. The Bluetest HP RC is used for almost all of the RC measurements in this thesis (except for the Doppler spread measurements in Section 2.3, the throughput measurement in Section 3.4, and part of the uncertainty measurements in Section 4.3). It has two plate mode-stirrers, a turn-table platform and three antennas mounted on three orthogonal walls (referred to as wall antennas hereafter). The wall antennas are wideband half-bow-tie

(or triangular sheet) antennas. In the measurements, the platform (with a radius of 0.3 m), on which the reference discone antenna (see Fig. 2.2) was mounted, was moved step-wisely to 20 positions equally spaced by 18° , and for each platform position the two plates simultaneously and step-wisely moved to 10 positions (equally spanned on the total distances that they can travel). All the mechanical (step-wise) movements were controlled by a computer. The platform and plate positions are referred to as stirrer positions in this thesis. At each stirrer position and for each wall antenna a frequency sweep was automatically performed by a vector network analyzer (VNA) (that was controlled by the computer as well), during which the channel transfer functions at different frequencies were sampled. The frequency step was set to 1 MHz. The sampled channel transfer function (or frequency response) is a function of frequency and stirrer position, denoted as $H(f, n)$. The (normalized) ACF $R_f(\partial f)$ of the transfer function is

$$R_f(\partial f) = \frac{E\left[H(f, n) \cdot H^*(f + \partial f, n)\right]}{E\left[|H(f, n)|^2\right]} \quad (2.4)$$

where the superscript * represents complex conjugation, and E denotes the (mathematical) expectation over the channel random variable. In the calculations, E was approximated by the sample mean of the ACF of the measured channel samples.

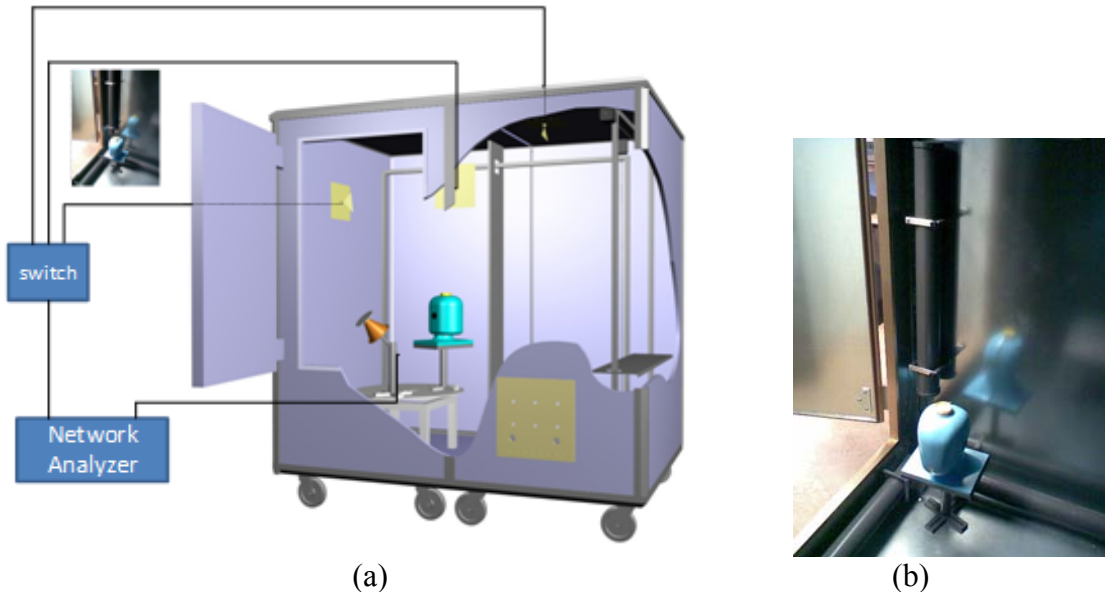


Figure 2.2: (a) Drawing of Bluetest HP RC with two mechanical plate stirrers, one platform and three wall antennas; (b) head phantom and the location of the three absorber-filled PVC cylinders for the loading (to be defined in Section 2.2).

Note that in the step-wise stirring sequence (as described above) the channel sampled by the VNA is essentially the block-fading channel [38], which is commonly assumed in the communication- and information-theoretic literature. Also note that (2.4) is a general formula for the ACF evaluations, which requires a lot of channel samples for an accurate ACF estimation. However, to gather many channel realizations is usually time-consuming (and expensive) when performing measurements in a real-life multipath environment. Therefore, in the literature, there is a more popular formula:

$$R_f(\partial f) = \frac{\int H(f)H^*(f + \partial f)df}{\int |H(f)|^2 df}. \quad (2.5)$$

The theory behind (2.5) is the WSSUS and Gaussianity assumptions. Specifically, the US assumption in the delay domain (i.e. scattering waves from different scatters are uncorrelated [6], [49]) necessitates the WSS properties in the frequency domain. Provided that $H(f)$ is a Gaussian random process with an ACF that is asymptotically decaying, then, based on the autocorrelation ergodic theorem [53], $H(f)$ is autocorrelation ergodic. In other words, (2.5) holds if and only if $H(f)$ is a Gaussian random process with an ACF that is asymptotically decaying. Although the asymptotical decay property of an ACF seems to be ubiquitous for channels in multipath environments, the Gaussianity assumption does not necessarily hold in general [49]. So (2.5) has to be used with great care. It is well known that the necessary and sufficient conditions for autocorrelation ergodicity hold for RCs [12], [25], therefore, (2.5) could have been used for the ACF evaluations in this thesis, in which case the resulting coherence bandwidth would have been a smooth function of frequency. Nevertheless, in order to observe possible frequency variations in B_c , (2.4) is used instead in this thesis.

The time dispersive property of a multipath channel is usually characterized by its RMS delay spread [49]

$$\sigma_\tau = \sqrt{\frac{\sum_k P(\tau_k)\tau_k^2 / \sum_k P(\tau_k) - [\sum_k P(\tau_k)\tau_k / \sum_k P(\tau_k)]^2}{P(\tau) = |h(\tau)|^2}} \quad (2.6)$$

where the received power $P(\tau_k)$ at delay τ_k is the so-called power delay profile (PDP), and $h(\tau)$ is the impulse response obtained from the inverse Fourier transform (IFFT) of the channel frequency response $h(\tau, n) = \text{IFFT}\{H(f, n)\}$ at each stirrer position n . The RMS delay spread is calculated by (2.6) using PDP averaged over all the stirrer positions. Note that (2.6) is based on the US assumption, which of course holds in RCs. In cases where the US assumption does not hold, the delay spread evaluations would be more mathematically involved [50]. Note that the VNA can generate only discrete frequencies, which results in periodicity in the delay domain. Therefore, the 1-MHz frequency step set in the measurement allows non-aliasing PDP detections of up to 1000 ns. Fortunately, PDPs with larger delays have rather limited fraction of the total power (see the PDP profile in Fig. 2 of [55]) thanks to the exponential distribution of the PDP in Rayleigh fading environments (e.g. RCs). Hence, the chosen frequency step should not cause any noticeable error.

As mentioned earlier in this chapter, the delay spread σ_τ and the coherence bandwidth B_c are inversely proportional to each other [44]. Depending on the actual definition of B_c , their relation varies. Given the coherence bandwidth definition (see Fig. 2.1 for illustration) and the assumption of isotropic scattering environments (e.g. RCs), their relation is

$$B_c = \sqrt{3} / (2\pi\sigma_\tau). \quad (2.7)$$

See Appendix A for the derivation of (2.7). The plots of σ_τ and B_c are shown in the next section together with two parameters that are physically associated with the RC.

2.2 Average Mode Bandwidth and Decay Time

The mode bandwidth is defined as the frequency range over which the power in one excited (or induced) mode is larger than half the power in the resonating mode. It is related to the quality-factor Q as

$$\Delta f = f / Q \quad (2.8)$$

where Q is given as

$$Q = 2\pi f U_s / P_d \quad (2.9)$$

with U_s as the steady state energy in the RC and P_d as the dissipated power. The introduction of the average mode bandwidth Δf makes it possible to characterize all the different losses appearing in the RC as additive contributions, i.e.

$$\begin{aligned} \Delta f &= \Delta f_{con} + \Delta f_{obj} + \Delta f_{ap} + \Delta f_{ant}, \\ \Delta f_{ant} &= \sum_{antennas} c^3 e_{rad} / (16\pi^2 f^2 V), \\ \Delta f_{obj} &= \sum_{objects} c\sigma_a / (2\pi V) \end{aligned} \quad (2.10)$$

where V is the volume of the chamber, e_{rad} is the radiation efficiencies of the antennas, and σ_a is the average absorption cross sections of the lossy objects, Δf_{con} , Δf_{obj} , Δf_{ant} and Δf_{ap} are average mode bandwidths due to the finite metallic conductivity, absorbing objects, antennas inside the chamber, and the aperture leakage, respectively. Equations (2.10) are the same as (6) in [54], except that they are expressed in terms of Δf instead of Q . The expressions of Δf_{ant} and Δf_{obj} are useful in order to understand how Δf can be controlled. The average mode bandwidth is given as [54]

$$\Delta f = c_0^3 e_{rad1} e_{rad2} / (16\pi^2 f^2 V G_{ch}) \quad (2.11)$$

where e_{rad1} and e_{rad2} are the total radiation efficiencies of transmit and receive antennas in the RC, respectively, and G_{ch} is the average power transfer function (i.e. average squared magnitude of the channel transfer function).

From the definition of the decay time,

$$\tau_{RC} = Q / (2\pi f) = 2\pi \Delta f. \quad (2.12)$$

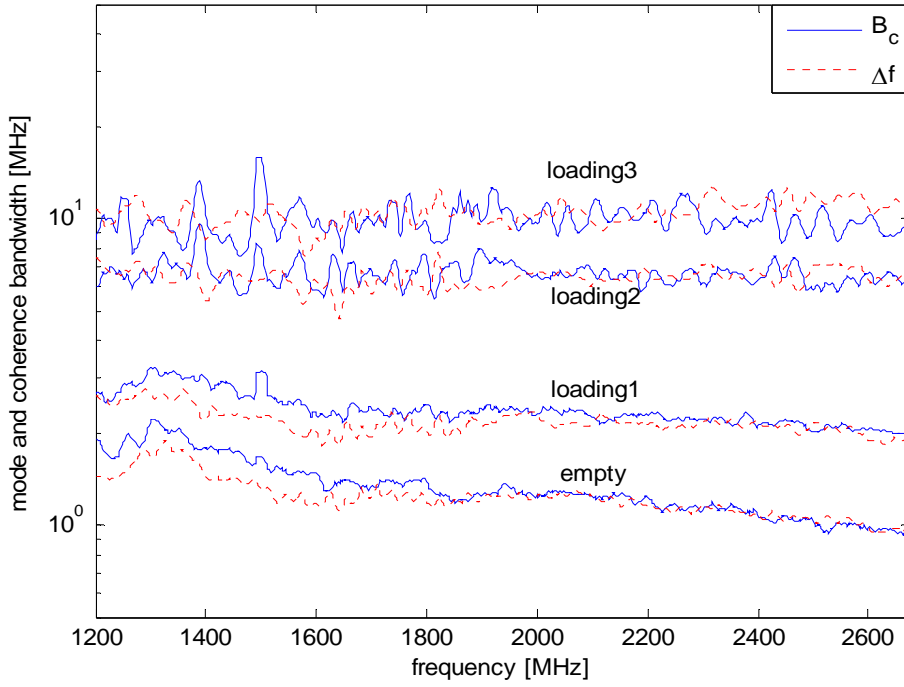


Figure 2.3: Comparison of average mode bandwidths and coherence bandwidths for different RC loadings.

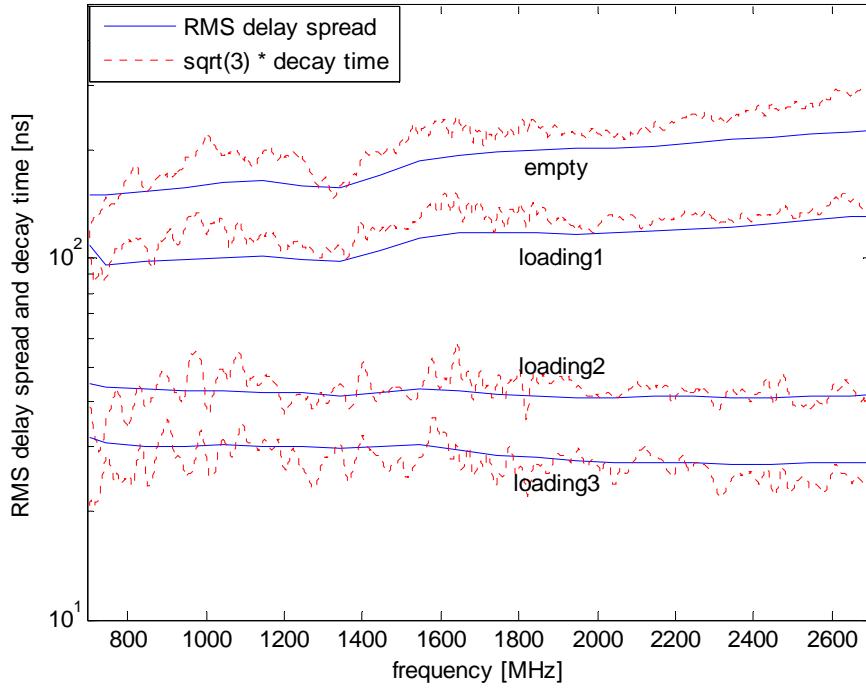


Figure 2.4: Comparison of σ_τ and $\sqrt{3}\tau_{RC}$ for RC different loadings.

Substituting (2.11) into (2.12), the decay time of the RC can be expressed as

$$\tau_{RC} = 8\pi f^2 V G_{ch} / (c_0^3 e_{rad1} e_{rad2}). \quad (2.13)$$

Intuitively the average mode bandwidth should be equal to the coherence bandwidth from their definitions. Based on this conjecture, it can be easily shown that

$$\sigma_{\tau} = \sqrt{3}\tau_{RC}. \quad (2.14)$$

Based on the RC measurement (cf. Section 2.1), the average mode bandwidth and the coherence bandwidth are calculated and plotted in Fig. 2.3, where “empty” corresponds to unloaded chamber, “loading1” is a head phantom that is equivalent to a human head in terms of EM absorption, “loading2” is the head phantom plus three Polyvinyl Chloride (PVC) cylinders filled with EM absorbers cut in small pieces, and “loading3” is the head phantom plus six such cylinders. Every three lossy cylinders were located along orthogonal corners of the chamber (see Fig. 2.2 (b)) in such a way that they approximately attenuate cavity modes of different polarizations equally much. From Fig. 2.3 it is seen that the coherence bandwidth and the average mode bandwidth are approximately the same, as expected. Similarly, σ_{τ} and $\sqrt{3}\tau_{RC}$ are calculated and plotted in Fig. 2.4. It is shown that they agree with each other well for almost all the loadings, especially for loaded RCs, over most frequency range.

Compared with the RMS delay spread and coherence bandwidth, the decay time and average mode bandwidth involve much less computational effort. Therefore, they offer a computationally cheaper alternative for RC channel characterizations. In addition, from Figs. 2.3 and 2.4 it can be seen that the channels in the RC can be controlled by simply loading the RC.

The coherence bandwidth parameterizes the frequency-selectiveness of the channel. The channel time-selectiveness can be characterized by the Doppler spread, which is discussed in the next section.

2.3 Doppler Spread

Different methods for determining the Doppler spread have been studied in [56]-[59]. Reference [56] and [57] directly evaluated the Doppler spread from its definition. Doppler spread estimation in the presence of the carrier frequency offset (CFO) was considered in [58]. By doing channel sounding in the RC with a VNA, the CFO problem is avoided. Therefore there is no need to resort to sophisticated signal processing algorithms as that shown in [58]. The Doppler spread in a RC has been observed by simply sweeping the intermediate-frequency (IF) bandwidth of the VNA in the continuous-wave mode and observing the power variation [59]. However, this method gives only a rough estimation of the Doppler frequency (not to mention the fact that the noise floor changes with the IF bandwidth of the VNA), and it can only predict the Doppler spread at a single frequency based on one measurement. This section shows how the Doppler spread can be easily obtained at all the measured frequencies for any assumed stirrer speed even though the measurements are done when the stirrers are step-wisely stationary (i.e. each VNA measurement is done under stationary conditions with no actual Doppler frequency shift).

The channel transfer function is expressed as a function of frequency and time $H(f, t)$. Its (unnormalized) ACF with respect to (w.r.t.) time (hereafter referred to as time ACF to distinguish with the ACF w.r.t. frequency in Section 2.1) is

$$R_t(f, \partial t) = E[H(f, t)H^*(f, t + \partial t)]. \quad (2.15)$$

The expectation E in (2.15) should be taken over the channel random variable. Based on the WSS assumption in time domain (or US assumption in Doppler frequency domain), the time ACF can be calculated by integrating over time, analogous to (2.5), which simplifies the measurement requirement (in terms of the sample number) a lot. Denoting the Doppler (shift) frequency as f_d , the Doppler spectrum becomes [56]

$$S_d(f, f_d) = \int_{-\infty}^{\infty} R_H(f, \partial t) \exp(-j2\pi f_d \partial t) d(\partial t). \quad (2.16)$$

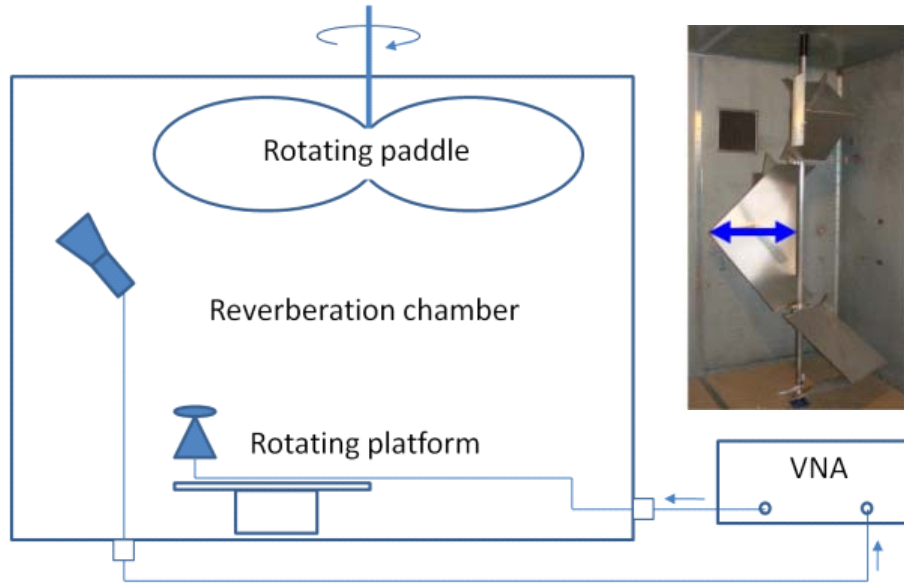


Figure 2.5: Illustration of measurement setup with rotating paddle and turn-table platform. The actual mechanical stirrers used in the measurements are shown in photo with its maximum radius specified by the arrow.

The Doppler spread is defined as the range of Doppler frequency f_d over which $S_d(f, f_d)$ is above a certain threshold (say, the noise floor). Note that since $R_H(f, \partial t)$ is complex conjugate symmetric, its Fourier transform $S_d(f, f_d)$ is real. The time ACF (2.15) is equivalent to

$$R_t(f, \partial t) = H(f, \partial t) \otimes H^*(f, -\partial t) \quad (2.17)$$

where \otimes represents the convolution. Applying the Fourier transform to both sides of (2.17),

$$S_d(f, f_d) = H(f, f_d)H^*(f, f_d) = |H(f, f_d)|^2 \quad (2.18)$$

where $H(f, f_d)$ is the Fourier transform of $H(f, t)$ w.r.t. time t .

The RC used in this section is a large chamber ($3.00 \times 2.45 \times 2.45 \text{ m}^3$) located at SP Technical Research institute of Sweden (SP for short), Borås, Sweden. The SP RC makes use of a rotating paddle and a turn-table platform (see Fig. 2.5). The receive antenna is a discone antenna mounted on the platform, and the transmit antenna is a horn antenna pointed into a corner of the RC.

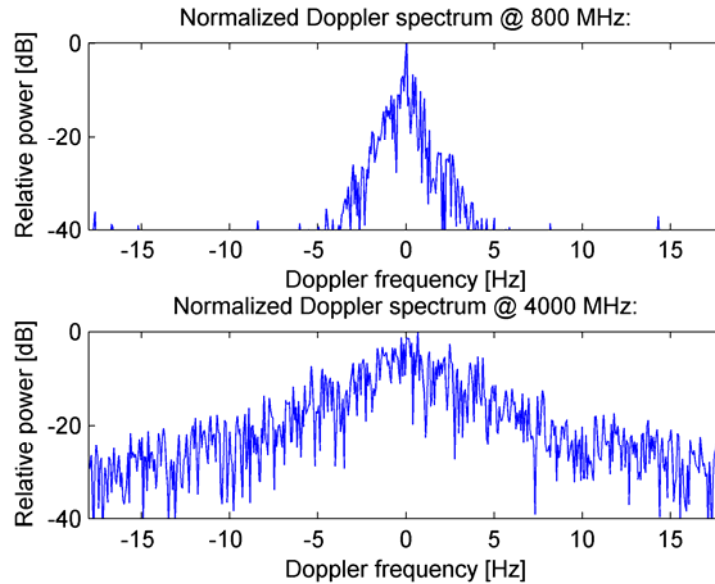


Figure 2.6: Doppler power spectrum at two different frequencies. The RMS Doppler bandwidth for this set of data equal to 1.0 Hz at 800 MHz and 3.6 Hz at 4GHz.

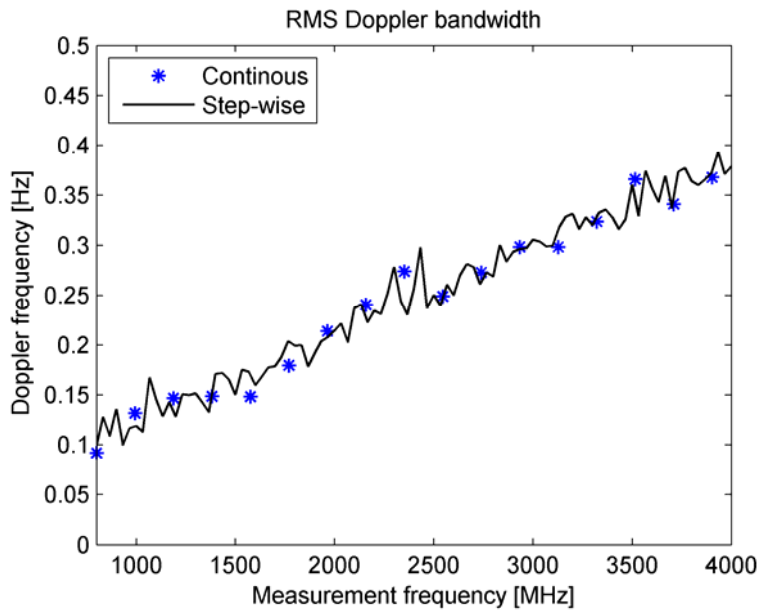


Figure 2.7: Validation of RMS Doppler bandwidth obtained by using present step-wise stationary approach by comparison with results obtained from actual time-varying measurements using continuous movement of the stirrers with given speeds at discrete frequencies.

The RMS Doppler spread at a certain frequency f_0 is given by

$$\sigma_d = \left[\frac{\int f_d^2 S_d(f_0, f_d) df_d}{\int S_d(f_0, f_d) df_d} \right]^{1/2}. \quad (2.19)$$

The integrations in (2.19) should exclude the noise floor (i.e. the level where the Doppler spectrum becomes flat). The step-wise stationary stirring method presented in [30] is used in this section to evaluate the Doppler spread. With this method, the Doppler spread can be determined by assuming that the fixed stirrer positions are the time moments of a continuously moving stirrer with a virtual stirrer speed. The advantage of this method is that one can obtain Doppler spreads with any stirrer speed for the whole frequency sweeping range. During the step-wise measurement, a complete paddle rotation was divided into 720 positions, giving an angular step of 0.5 degrees. At each paddle position, a frequency sweep is performed by the VNA. By assuming that a complete paddle rotation takes 20 s, and using the step-wise stationary stirring method, the Doppler spectrum can be calculated. Fig. 2.6 shows the Doppler spectrums obtained in the SP RC, where the dB vertical scale is chosen by convention. Linear-scaled Doppler spectrums in a RC can be found in [31], which allow a closer examination of the shape of the RC Doppler spectrum. Note that in an ideal isotropic-scattering RC, the Doppler spectrum seen by an isotropic antenna that is moving with a constant velocity is actually rectangular (see Appendix B for the proof). Here the irregular Doppler spectrum shape observed in the RC is due to the non-isotropic antennas and its rotational movement.

To validate the step-wise stationary stirring method, additional measurements with continuously moving stirrers were performed by setting the VNA in the continuous-wave mode. This is the traditional way of detecting the Doppler spread. Using this traditional method, one can only perform the measurement once at a single frequency, and thus needs to repeat the measurement many times to cover the frequency range of interest. The VNA was used to measure $H(f, t)$ 750 times for one complete rotation of the platform and paddle. The rotation time T was increased to 182 sec in order to be able to capture the data with the data acquisition software. Thus the observed Doppler shift was very small. Fig. 2.7 shows the comparison of the Doppler spread obtained during continuous stirring (using the traditional method) and that obtained with the step-wise stationary stirring method by assuming the same speed. Good agreements are observed as expected.

The coherence bandwidth and Doppler spread studies conclude the characterizations of SISO channel in RCs. The spatial characterization is naturally deferred to the next chapter, where MIMO channel is introduced.

3. Measurements of MIMO Terminals

The RC can be used to measure the radiation efficiency and the free-space reflection coefficient of a single-port antenna [60], [61], and the diversity gain and the capacity for a multi-antenna system [13]-[20]. This chapter mainly deals with multi-port antenna measurements for diversity and capacity evaluations. Nevertheless, since the antenna radiation efficiency and mismatch factor are important parameters for multi-port antennas as well, the chapter starts with them using the example of a single-port horn antenna for heuristic purposes. Diversity and capacity evaluations based on RC measurements are presented sequentially. In addition, their counterparts evaluations based on AC measurements are shown correspondingly for comparisons. In the end of this chapter, an active throughput measurement of a USB dongle is presented, together with a simple throughput model that agrees well with the measurement results.

3.1 Measurement of Single-Port Antenna

The total radiation efficiency of an antenna under test (AUT) can be measured in a RC by the following procedure: first, the average power transfer function of a reference antenna with known total radiation efficiency, e_{ref} , is measured as G_{ref} , then, the AUT is measured with another average power transfer function G_{AUT} . The total radiation efficiency of the AUT is then

$$e_{rad} = \frac{G_{AUT}}{G_{ref} / e_{ref}}. \quad (3.1)$$

The total radiation efficiency is the product of the radiation efficiency and the mismatch factor [62]. Knowing the total radiation efficiency, one has to determine the free-space mismatch factor (or reflection coefficient) in order to know the radiation efficiency. Theoretical models of antenna impedances in a metal cavity were studied in [63], [64]. A common disadvantage of these models is that they are constrained to linear small antennas with simple geometries. For arbitrary large antennas with complex geometries, the corresponding theoretical models (if possible) are difficult to build. Therefore, the simple statistical model of the reflection coefficient proposed in [65] is used in this section. Assume that the reflection coefficient can be split into a free-space (deterministic) part and a (stochastic) part due to the RC,

$$\mathbf{S}_{11}^{tot} = \mathbf{S}_{11}^{fs} + \mathbf{S}_{11}^{RC} \quad (3.2)$$

where \mathbf{S}_{11}^{tot} is the total reflection coefficient of the antenna in the RC, \mathbf{S}_{11}^{fs} is the free-space reflection coefficient that is independent of the RC, and \mathbf{S}_{11}^{RC} is the reflection coefficient contribution due to the random scattering in the RC. For a well stirred RC, \mathbf{S}_{11}^{RC} has a zero-mean complex Gaussian distribution [66], provided the antenna is not too directive (otherwise, it may experience less randomness and therefore the distribution of \mathbf{S}_{11}^{RC} may deviate from zero-mean Gaussianity). Thus, the mean value of the reflection coefficient measured in the RC is

$$E[S_{11}^{tot}] = S_{11}^{fs}. \quad (3.3)$$

As before, the expectation is approximated by the sample mean. This estimator therefore depends on the number of independent samples. Interestingly, simple as it is, (3.3) is the best estimator, i.e. minimum variance unbiased (MVU) estimator, of the free-space S_{11} . While its unbiased property is obvious from (3.3), one can readily show that its variance meets the Cramer-Rao bound (CRB), which is the lower bound on the variances of all estimators [67]. In fact, in this case it is also a least-squares (LS) estimator and a maximum likelihood (ML) estimator (see [67] for the proofs).



Figure 3.1: Photo of a standard gain horn antenna mounted on the platform in the RC.

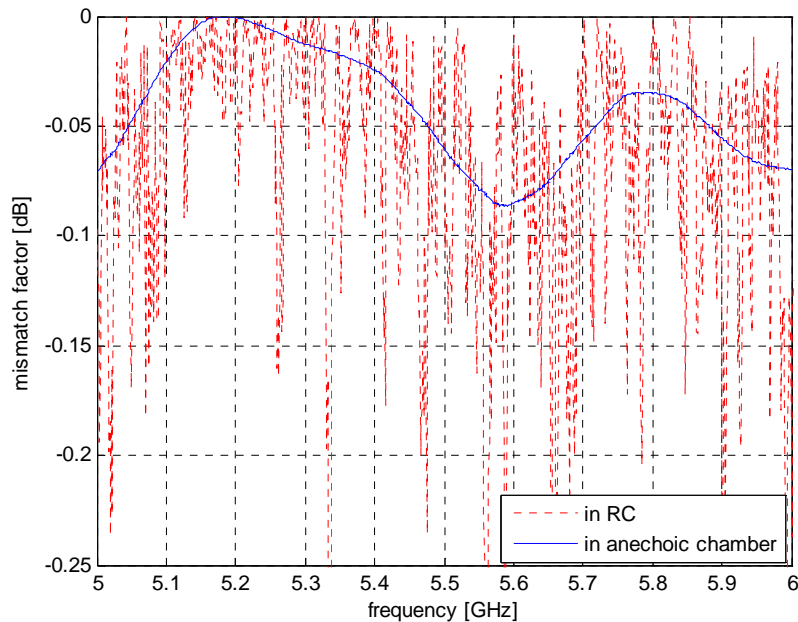
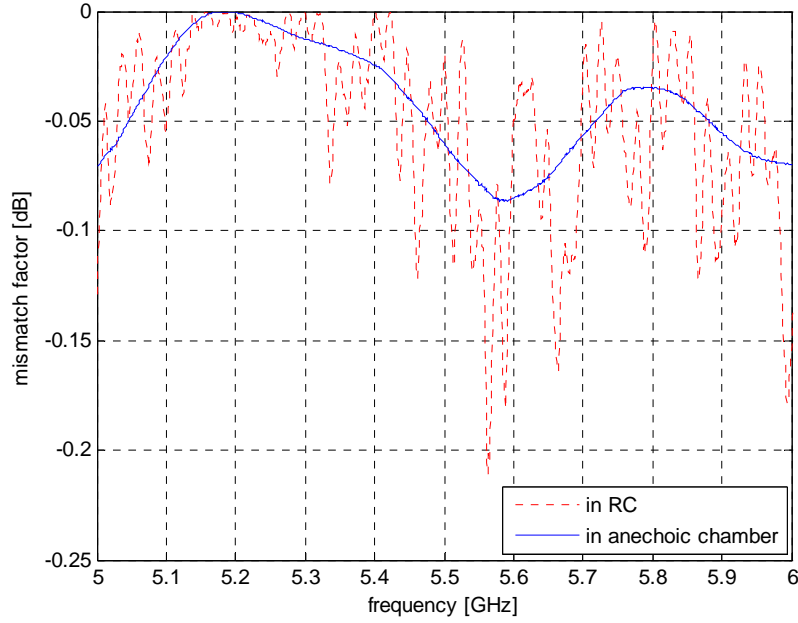
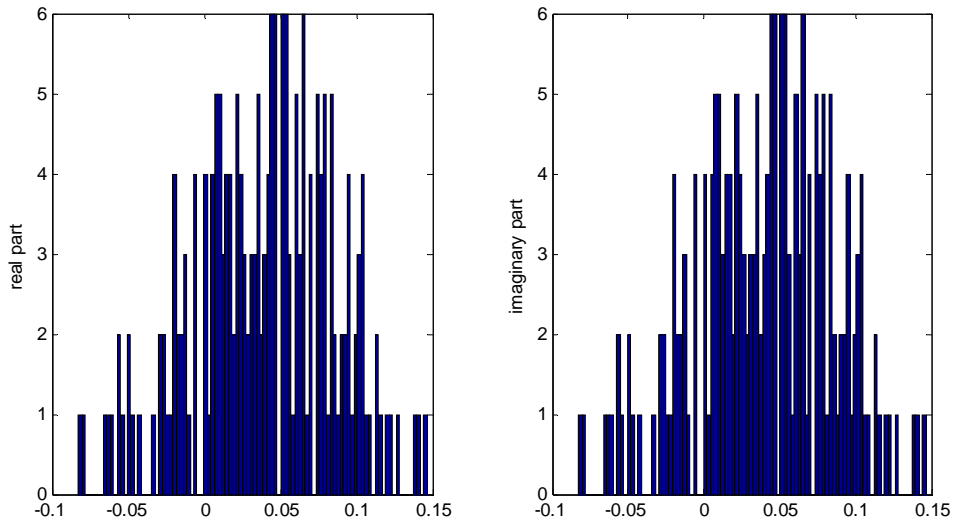


Figure 3.2: Mismatch factor at one stirrer position in the RC and in the anechoic chamber.



(a)

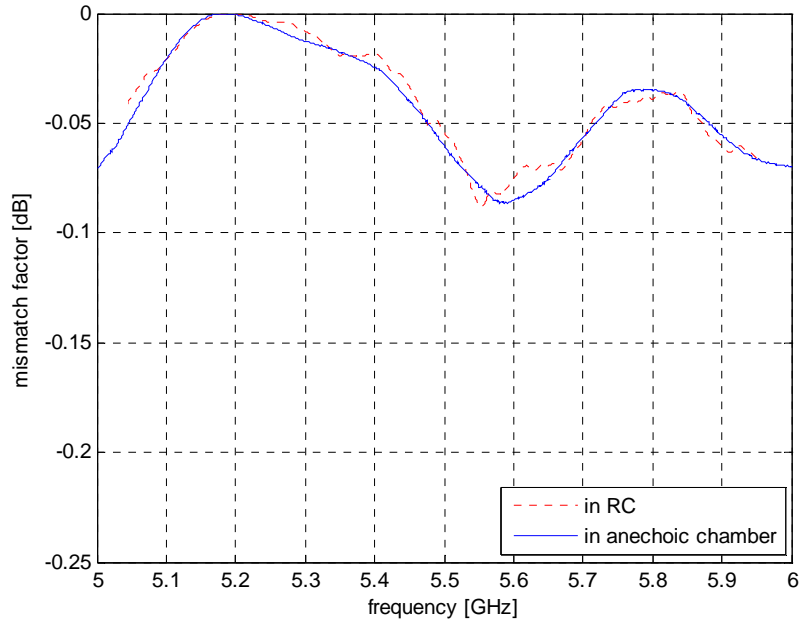


(b)

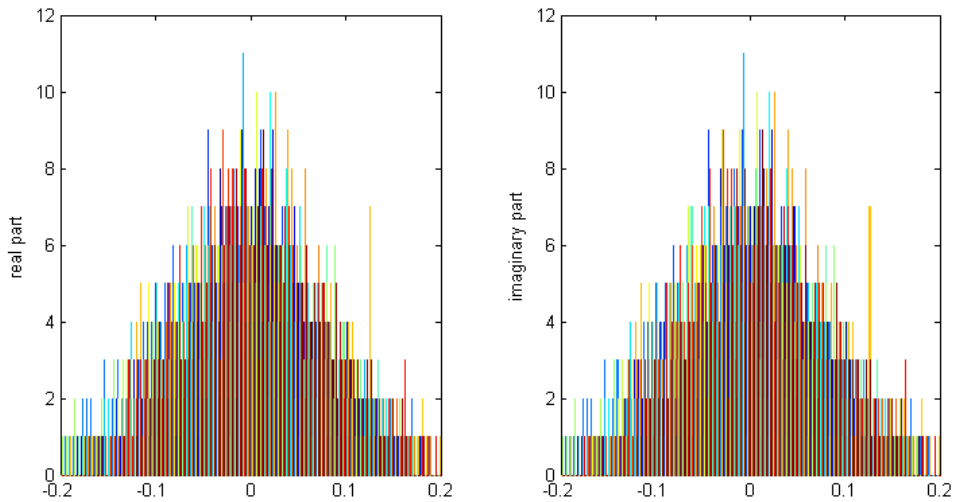
Figure 3.3: (a) Mismatch factor of the AUT in the RC with stirrer position average and that measured in the anechoic chamber; (b) histogram of real and imaginary parts of S_{11}^{RC} at 5.5 GHz.

The AUT is chosen to be a standard gain horn antenna working from 3.94 to 5.99 GHz (see Fig. 3.1). Measurements were done from 5 to 6 GHz with a frequency step of 1 MHz in the Bluetest HP RC. The measurement setup is the same as that of the channel characterization measurement described in Section 2.1. Namely, there are 600 samples (20 platform positions, 10 stirrer plate positions, and three wall antennas) at each frequency. Fig. 3.2 shows the mismatch factor (in dB) at one arbitrary stirrer position in RC, compared with that in an AC. Fig. 3.3 (a) shows the mismatch factor of the AUT in the RC when the free-space S_{11} is estimated by complex stirring over the 600 samples only, compared with that from the AC. Fig. 3.4 (a) shows similar results but with additional 100-MHz complex frequency stirring (or

electronic mode stirring) [68] for the RC measurement. The frequency stirring technique, in principle, is to treat the samples at different frequencies (within the frequency stirring bandwidth) as if they were from the same random process. The improved estimation accuracy can be explained by the histograms without and with the 100-MHz complex frequency stirring, shown in Fig. 3.3 (b) and Fig. 3.4 (b). That is with additional complex frequency stirring, the mean value of S_{11}^{RC} approaches zero with larger probability.



(a)



(b)

Figure 3.4: (a) Mismatch factor of the AUT measured in the RC with 100-MHz frequency stirring, and that measured in the anechoic chamber; (b) histogram of real and imaginary parts of S_{11}^{RC} around 5.5 GHz with a bandwidth of 100 MHz.

Fig. 3.5 shows the standard deviation (STD) of the difference of the RC and AC measurement results as a function of frequency stirring bandwidth. It is shown that the optimal (in the LS sense) frequency stirring bandwidth for this particular horn antenna is 110 MHz. Note that in general, the optimal frequency stirring bandwidth for an arbitrary antenna is unknown. Also note that the frequency stirring reduces the frequency resolution. Thus one has to choose the

frequency stirring bandwidth with great care. Based on empirical experiences, 10-MHz (or slightly less) frequency stirring is close to optimal for non-directive small antennas (e.g. dipoles). A larger bandwidth can be chosen if the AUT is wideband and well-matched.

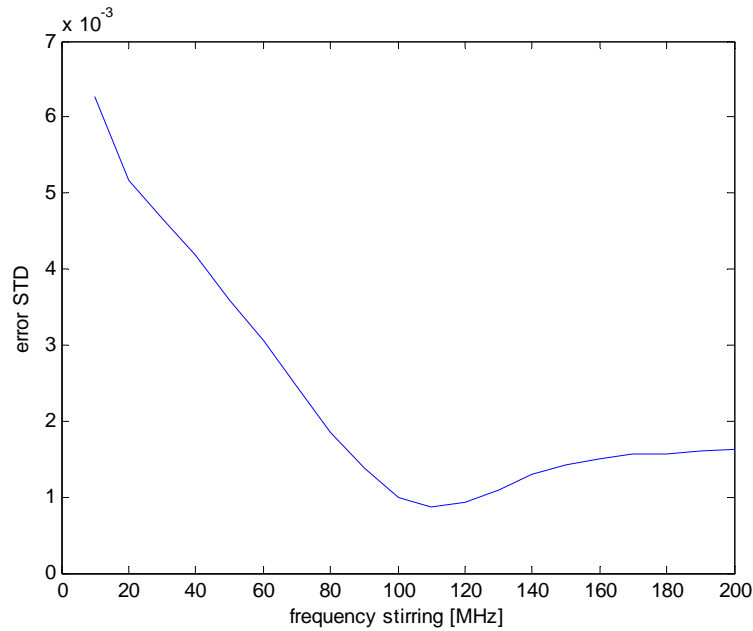


Figure 3.5: STD of the difference of the RC and AC measurement results as a function of frequency stirring bandwidth.

3.2 Diversity Gain Evaluation

Diversity techniques offer an effective leverage to mitigate detrimental fading in wireless multipath environments. Thus it has been popular since the 60s [2], [69]. There are mainly three types of diversity techniques: frequency diversity, time diversity, and antenna (or spatial) diversity. For the antenna diversity, there are three main diversity combining techniques: selection combining (SC), equal gain combining (EGC), and maximum ratio combining (MRC) [69]. Among them, the MRC offers the best performance at the expense of the most complexity. With the evolution of channel estimation techniques, MRC has become the most popular diversity technique [1], [7], [69]-[73]. Thus, this chapter focuses on the MRC diversity gain.

Before jumping into diversity measurements, a method for the MRC evaluation (i.e. the covariance-eigenvalue approach) is presented first. The robustness of the presented method is discussed. After that, comparisons between MRC diversity gains measured in a RC and an AC are compared using the example of a wideband log-periodic dual-dipole array.

3.2.1 Covariance-Eigenvalue Approach

Assuming an N -port diversity antenna in a Rayleigh-fading environment (e.g. a RC), its covariance matrix is

$$\mathbf{R} = E[\mathbf{h}\mathbf{h}^H] \quad (3.4)$$

where \mathbf{h} is a column-vector consisting of complex baseband sub-channels that include the overall antenna effect, and the superscript H denotes the Hermitian operator. The MRC output power is

$$P_{MRC} = \frac{1}{2} \mathbf{h}^H \mathbf{h}. \quad (3.5)$$

Assuming independent, identically distributed (i.i.d.) Gaussian noises with unity variance, P_{MRC} then equals, in value, to the instantaneous signal-to-noise ratio (SNR), denoted as γ , which is a random variable.

Note that in the information theory (and the probabilities) a random variable is usually written in upper case (e.g. [76]) or in bold face (e.g. [77]) to distinguish it from deterministic ones. Following the convention in the signal processing (and the communications) literature, this chapter reserves lower (upper) case bold face letters for vectors (matrices), in order to distinguish them from scalar values. And no extra effort is exerted in separating random variables from deterministic ones. Hopefully, their distinctions are clear from the context.

The characteristic function [74] of the instantaneous SNR γ is

$$\phi(z) = E[\exp(jz\gamma)] \quad (3.6)$$

Equation (3.6) can be expressed as [75]

$$\phi(z) = \frac{1}{\det(\mathbf{I} + z\mathbf{R})} = \prod_{i=1}^N \frac{1}{1 + z\lambda_i} \quad (3.7)$$

where λ_i denotes the i th eigenvalues of \mathbf{R} . The probability density function (PDF) of γ is the inverse Fourier transform of $\phi(z)$,

$$p(\gamma) = \frac{1}{\prod_i \lambda_i} \sum_i \frac{\exp(-\gamma / \lambda_i)}{\prod_{k \neq i} (1 / \lambda_k - 1 / \lambda_i)}. \quad (3.8)$$

The cumulative distribution function (CDF) of γ can be readily derived as,

$$F(\gamma) = 1 - \sum_{i=1}^N \frac{\lambda_i^{N-1} \exp(-\gamma / \lambda_i)}{\prod_{k \neq i} (\lambda_i - \lambda_k)}. \quad (3.9)$$

In this thesis, (3.9) is referred to as Lee's (CDF) formula, since it is derived by Lee [71]. The effective diversity gain (EDG) is defined as the improvement of the output SNR of a diversity antenna compared with that of a single ideal antenna (with 100% radiation efficiency) at a certain outage probability level, e.g. 1% [69]. The MRC EDG is,

$$EDG = \left. \frac{F^{-1}(\gamma)}{F_{ideal}^{-1}(\gamma)} \right|_{1\%} \quad (3.10)$$

where $(\cdot)^{-1}$ denotes the functional inversion, and F_{ideal} is the CDF of output SNR of a single ideal antenna. Note that the diversity gain defined here (from the antenna point-of-view) is different from the ones defined in communications, where the diversity gain denotes the asymptotic slope of the bit-error-rate (BER) curve as a function of SNR [50]. Without further specifications, the diversity gain in this thesis is given by (3.10).

For Rayleigh fading,

$$F_{ideal}(\gamma) = 1 - \exp(-\gamma). \quad (3.11)$$

The CDF of the MRC output SNR in the Rayleigh fading is known for two cases:

- When all eigenvalues are different from each other, it is given by (3.9);
- When all eigenvalues are equal, i.e. $\lambda_i = \lambda$ ($i = 1 \dots M$), it is given by [69]

$$F(\gamma) = 1 - \exp\left(-\frac{\gamma}{\lambda}\right) \sum_{i=1}^N \frac{(\gamma/\lambda)^{i-1}}{(i-1)!}. \quad (3.12)$$

The CDF expressions with an arbitrary number of equal eigenvalues are unknown in general and have to be approximated by empirical CDFs from measured channel samples. As will be shown later in this thesis, Lee's formula (3.9) is robust for stochastic measurements and therefore can be used for the diversity evaluation of arbitrary antennas based on RC measurements. Since the EDG is determined from the CDF as a function the eigenvalues of the covariance matrix, this diversity-evaluation method is referred to as covariance-eigenvalue approach in this thesis. Compared to the traditional way of diversity evaluations (that involves empirical CDF), the covariance-eigenvalue approach offers faster convergence and better accuracy (with large probability) for the same (finite) number of channel samples [16].

It can be seen from (3.9) that Lee's formula has an apparent singularity when any two eigenvalues of the diversity antenna's covariance matrix are equal. Therefore, it is usually believed that Lee's formula would result in large numerical error when two eigenvalues are close to each other. This thesis, however, shows that the EDG obtained using the covariance-eigenvalue approach converges in distribution to the true value, i.e. Lee's formula converges to the true CDF when the eigenvalues approaches each other.

Based on the RC measurement (or any stochastic measurements), the covariance matrix can be estimated by the sample mean (cf. Appendix B), i.e.

$$\hat{\mathbf{R}} = \frac{1}{M} \sum_{m=1}^M \mathbf{h}_m \mathbf{h}_m^H \quad (3.13)$$

where \mathbf{h}_m is the m th realization of the random channel vector \mathbf{h} , and M is the number of realizations (or samples). Interestingly, (3.13) is the unbiased ML estimator of \mathbf{R} , the proof of which can be found in Section 7.1.1 of [78]. This thesis refers to (3.13) as sample covariance matrix and its eigenvalues, $\hat{\lambda}_i$ ($i = 1 \dots N$), as sample eigenvalues.

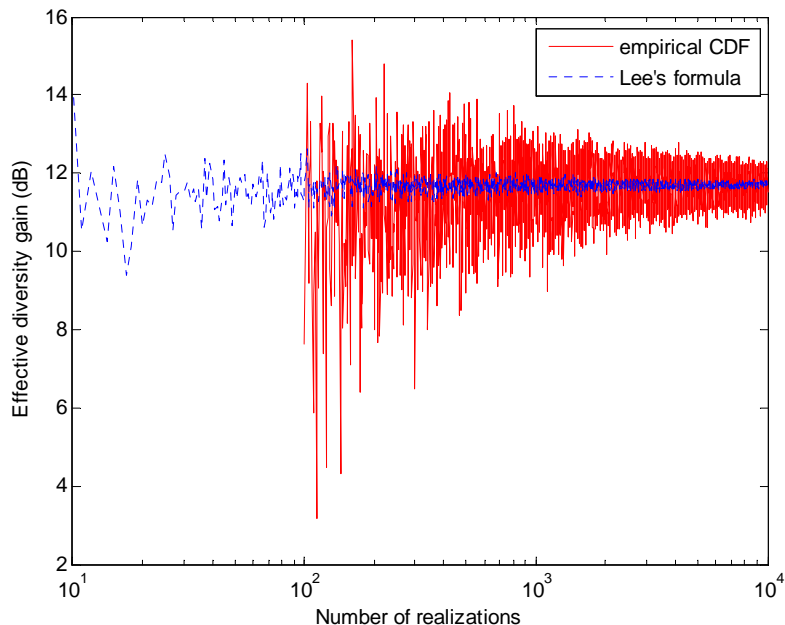


Figure 3.6: Numerically simulated EDG as a function of number of realizations for ideal two-port antenna.

Consider first an ideal two-port diversity antenna with 100% embedded radiation efficiencies and no correlation. The covariance matrix with perfect estimation is an identity matrix with equal eigenvalues of unity. In this case, there would have been singularity due to Lee's formula. Nevertheless, in practice, the diversity antennas' covariance matrices and eigenvalues in multipath fading environments are unknown, and have to be estimated from measured channel samples. Thus $\hat{\lambda}_i$ deviate from λ_i with probability one (w.p.1.). The question is if there will be large numerical error using Lee's formula? To answer that, an i.i.d. complex Gaussian channel, represented by \mathbf{h}_w , is generated with its Euclidean norm satisfying $E[\|\mathbf{h}_w\|_2^2] = N$, where $N = 2$ in this case. The channel seen by the diversity antenna can then be expressed as $\mathbf{h} = \mathbf{R}^{1/2} \mathbf{h}_w$, where $\mathbf{R}^{1/2}$ is the Hermitian square root of \mathbf{R} , which is the identity matrix \mathbf{I} in this case. The sample covariance matrix $\hat{\mathbf{R}}$ deviates from \mathbf{I} (due to finite sample number M) w.p.1.

Fig. 3.6 shows the EDG (as a function of the number of channel realizations) obtained using

Lee's formula with sample eigenvalues $\hat{\lambda}_i$ against that obtained using the empirical CDF from generated channel realizations. Surprisingly, the EDG converges to the true value, i.e., 11.7 dB, much faster than that of the empirical CDF. Moreover, it is surprising to see that there is no noticeable error when the number of samples increases, knowing that the sample eigenvalues are estimated more accurately and therefore become very close to each other with large numbers of independent channel realizations.

Consider then a three-port antenna with a covariance matrix

$$\mathbf{R} = \begin{bmatrix} 1 & 0.5 & 0.5 \\ 0.5 & 1 & 0.5 \\ 0.5 & 0.5 & 1 \end{bmatrix}, \quad (3.14)$$

such that two of the eigenvalues are equal ($\lambda_1 = 2, \lambda_2 = \lambda_3 = 0.5$). Repeating the same simulation procedure as described above, the EDGs are calculated and shown in Fig. 3.7 as a function of the number of channel realizations. Fig. 3.7 shows the EDG obtained using Lee's formula with sample eigenvalues $\hat{\lambda}_i$ against that obtained using the empirical CDF from generated channel realizations. Similar simulation results are observed, i.e. EDG obtained using Lee's formula with sample eigenvalues not only converges to the true value but also converge much faster than that obtained from the empirical CDF. By Murphy's Law, if there is a finite probability that sample eigenvalues equal to each other, one would have observed singularity problems in the simulations, but there are no singularity problems in either Fig. 3.6 or Fig. 3.7. Therefore, in practice, the covariance-eigenvalue approach is computationally robust for stochastic diversity measurements.

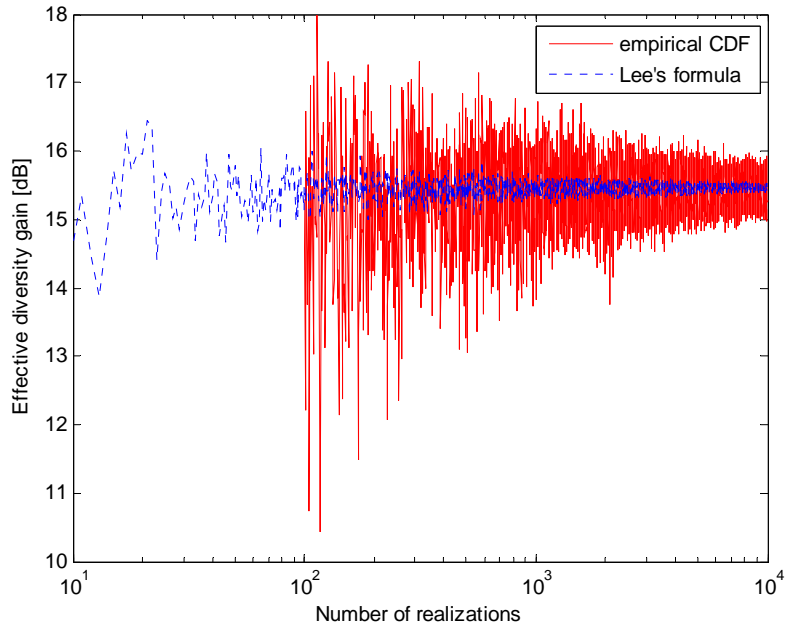


Figure 3.7: Numerically simulated EDG as a function of number of realizations for three-port antenna with a uniform correlation of 0.5.

From both Figs. 3.6 and 3.7, it seems that the limit of Lee's formula converges to the true CDF as the eigenvalues converge to each other. In other words, the EDG obtained using the

covariance-eigenvalue approach converges in distribution to the true value (see Appendix C for the proof). The faster convergence of Lee’s formula in sample number is because that the sample eigenvalues converge faster than the empirical CDF at the 1% level.

In the following subsections, the covariance-eigenvalue approach is used for diversity evaluations of a diversity antenna. Before going into the measurements, the AUT is described in the next subsection.

3.2.2 Eleven Antenna under Test

The so-called Eleven antenna (see Fig. 3.8) is chosen as the AUT. It is a log-periodic dual-dipole array working from 2 to 13 GHz [79]. In this paper, the four ports for one polarization of Eleven antenna, shown in Fig. 3.8, are combined with wideband 180° hybrids to form two-port and three-port antennas as shown in Figs. 3.9 and 3.10, respectively. The associate 180° hybrids have losses between 1.4 dB at 2 GHz and 3 dB at 8 GHz, where ohmic losses contribute the most. The ports of the two-port Eleven antenna are marked as ports P1 and P2 (see Fig. 3.9). The ports of the three-port Eleven antenna are marked as ports P1, P2 and P3 (see Fig. 3.10). In this thesis, the two Eleven antenna configurations are measured from 2 to 8 GHz in both a RC and an AC. The Eleven antenna is chosen because of its wideband property. By assuming narrowband multi-antenna systems, the wideband measurements can be virtually regarded as measurements of many narrowband antennas (working at different frequencies), which facilitates comparisons between RC and AC measurements.

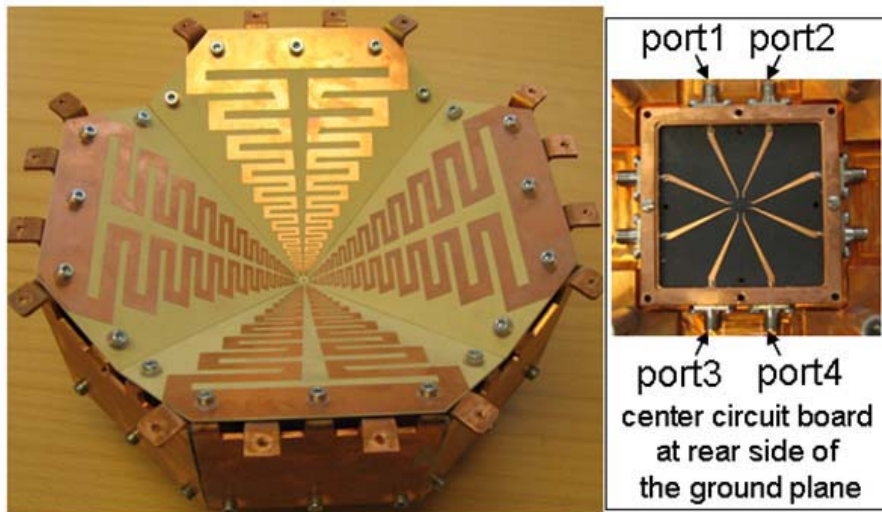


Figure 3.8: Photos of front and back sides of Eleven antenna.

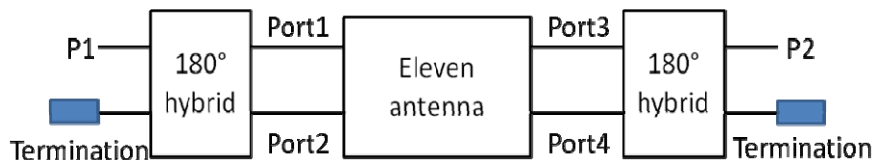


Figure 3.9: Diagram of Eleven antenna with the four ports for one polarization combined to form a two-port antenna.

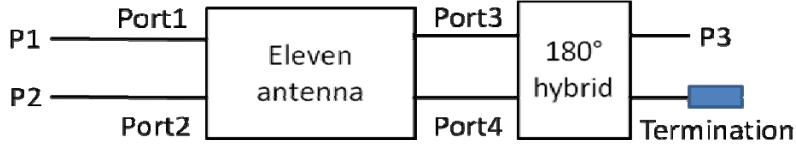


Figure 3.10: Diagram of Eleven antenna with the four ports for one polarization combined to form a three-port antenna.

3.2.3 RC and AC Measurements

The Eleven antenna was measured in the Bluetest HP RC with the same measurement setup as that of the channel characterization measurement described in Section 2.1. Namely, there are 600 samples (20 platform positions, 10 stirrer plate positions, and three wall antennas) at each frequency. In order to improve the measurement accuracy, the frequency stirring technique is applied to the measurement data. Though developed for RC applications [68], the same technique has independently been used in processing the measured data from real-life multipath environments [8], [11]. Using this technique, the frequency stirring bandwidth has to be carefully chosen so that more independent samples can be included without changing the channel statistics. Since the coherence bandwidth of the channel in the (unloaded) RC is around 1-2 MHz [27], the frequency step was set to 1 MHz, and a 20-MHz frequency stirring was used. Therefore, there are 12000 channel samples for diversity evaluations. Note that the Eleven antenna has a reflection coefficient below -10 dB over the measuring frequency range [79], thus a larger frequency stirring bandwidth could have been chosen; the 20-MHz frequency stirring was chosen to preserve a better frequency resolution (cf. Section 3.1). Also note that the VNA that was used for the RC measurement could gather a maximum of 1601 samples per frequency sweep. Therefore, the whole measurement frequency range had to be divided into four sub-bands, each with a bandwidth of 1.5 GHz, i.e. 2 – 3.5 GHz, 3.5 – 5 GHz, 5 – 6.5 GHz, and 6.5 – 8 GHz. The same measurement procedure was repeated over these four sub-bands.

The average power transfer function is measured using a reference antenna with known radiation efficiencies (over the measured frequency range). The reference level, P_{ref} , is obtained by dividing the average power level with the total radiation efficiency of the reference antenna (i.e. G_{ref}/e_{ref}). The measured diversity channel \mathbf{h}_{meas} is a function of frequency and stirrer position. To focus on the small-scale fading, the measured channel should be normalized,

$$\mathbf{h} = \mathbf{h}_{meas} / \sqrt{P_{ref}}. \quad (3.15)$$

Note that the RC attenuation and the total radiation efficiencies of the wall antennas are calibrated out by (3.15). Since the three wall antennas in the RC are located far away from each other on three orthogonal walls (with orthogonal polarizations), the correlations between them are negligible. The covariance matrix at the receive side can be estimated using (3.13). Once the covariance matrix is estimated, the MRC EDG can be readily obtained using the covariance-eigenvalue approach.

Diversity measurements in an AC are not as straightforward as that in the RC, because there is no random channel to measure in the AC. For diversity evaluations, one needs to measure the

embedded far-field functions and embedded radiation efficiencies at every antenna port. In this thesis, the embedded far-field functions and efficiencies of the multi-port Eleven antennas were measured (with an angular step of 1°) in the AC at Technical University of Denmark (DTU), Lyngby, Denmark. During the measurement, the AUTs were rotated by an azimuth positioner and the full-sphere near-field signal was measured on a regular grid by a dual-polarized probe located about 6 m away. The measured signal was then transformed to the far-field using the spherical wave expansion and properly correcting for the probe characteristics. Due to the symmetric property of the Eleven antenna, only the embedded far-field function and efficiency at the port P1 of the two-port Eleven antenna (see Fig. 3.9) and those at the port P1 of the three-port Eleven antenna (see Fig. 3.10) were measured, from 2 to 8 GHz with frequency step of 100 MHz. This simplification is necessary considering the time-consuming radiation pattern measurements in the AC. As a result, for the two-port Eleven antenna, the embedded far-field function at the port P2 is obtained by rotating that of P1 by 180° . For three-port Eleven antenna, the embedded far-field function at P2 is obtained from that of P1 by imaging; and the embedded far-field function at P3 is the same as that at P2 of the two-port Eleven antenna. Furthermore, for the two-port Eleven antenna the embedded radiation efficiency at P1 is the same as that at P2; for the three-port Eleven antenna the embedded radiation efficiency at P1 equals to that at P2 (with the embedded radiation efficiency of P3 equal to that at P2 of the two-port Eleven antenna).

For MRC diversity evaluations, the covariance matrix \mathbf{R} has to be constructed first:

$$\begin{aligned}\mathbf{R} &= \mathbf{\Xi} \circ \mathbf{\Phi} \\ \mathbf{\Xi} &= \sqrt{\mathbf{e}} \sqrt{\mathbf{e}}^T \\ [\mathbf{\Phi}]_{mn} &= \frac{\iint_{4\pi} \mathbf{g}_m^H(\Omega) \mathbf{P}_{inc}(\Omega) \mathbf{g}_n(\Omega) d\Omega}{\sqrt{\iint_{4\pi} \mathbf{g}_m^H(\Omega) \mathbf{P}_{inc}(\Omega) \mathbf{g}_m(\Omega) d\Omega \cdot \iint_{4\pi} \mathbf{g}_n^H(\Omega) \mathbf{P}_{inc}(\Omega) \mathbf{g}_n(\Omega) d\Omega}}\end{aligned}\quad (3.16)$$

where \mathbf{g}_i ($i = 1, \dots, N$) is the embedded far-field function vector (with elements representing components for different polarizations) at the i th antenna port, and \mathbf{P}_{inc} is dyadic power angular spectrum of the incident waves, $\mathbf{e} = [e_{emb1} \quad e_{emb2} \quad \dots \quad e_{embN}]^T$, \circ denotes entry-wise product, the superscript T denotes the transpose operator, and $\sqrt{\cdot}$ is entry-wise square root. Note that in polarization-balanced isotropic scattering environments, e.g. RCs, $\mathbf{P}_{inc}(\Omega) = \mathbf{I}$. Once the covariance matrix is constructed, one can apply the covariance-eigenvalue approach directly. In that case, it is necessary to put tiny marginal guards (say, “eps” in Matlab) between any (possibly) equal eigenvalues to avoid singularity in Lee’s formula, because the AC measurement is deterministic and therefore there is nonzero probability that some eigenvalues are equal.

3.2.4 Measurement Results

Although correlations and embedded radiation efficiencies are only needed for diversity evaluations based on AC measurements (evaluations of RC measurements are based on measured channel samples directly), it is still worthwhile to compare the measured embedded radiation efficiencies and correlations in both chambers, because they are also informative parameters for characterizations of multi-port antennas. The embedded radiation efficiencies are readily obtained from the AC measurements; the correlation coefficients in the AC can be

calculated using the last equation in (3.16). The measured embedded radiation efficiencies in the RC can be obtained by applying (3.1) at each port. The measured correlation coefficients in the RC can be obtained by

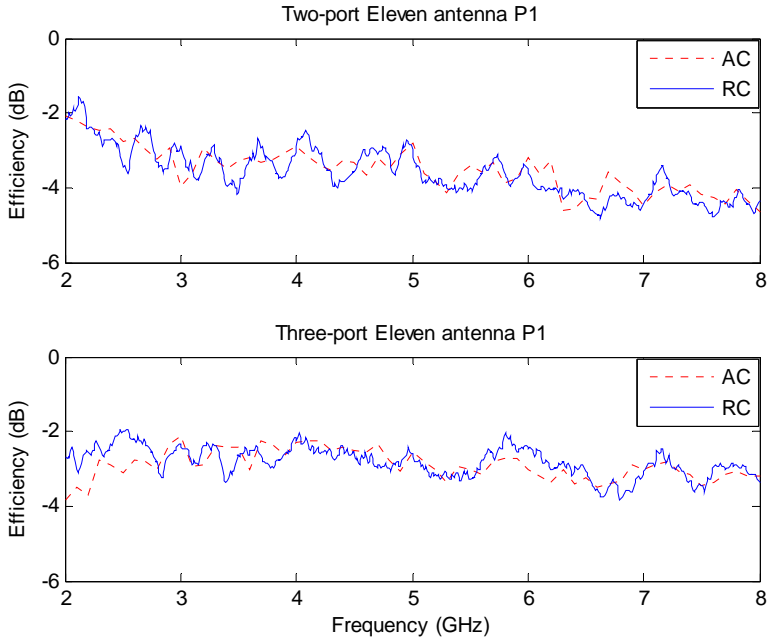


Figure 3.11: Comparison of measured total embedded radiation efficiencies from AC and RC.

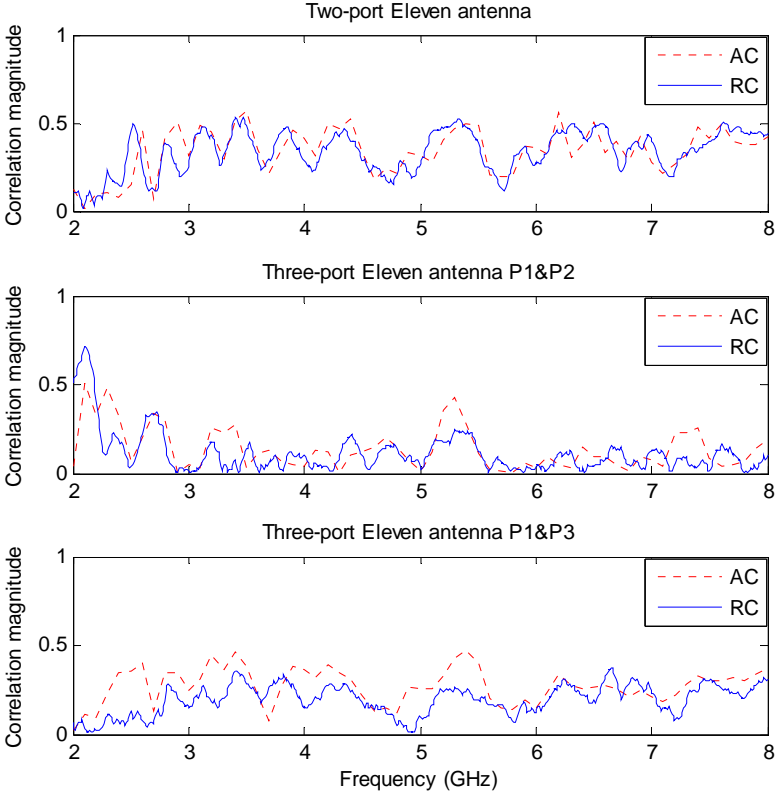


Figure 3.12: Comparison of measured correlation magnitudes from AC and RC.

$$\hat{\rho}_{mn} = \frac{[\hat{\mathbf{R}}]_{mn}}{\sqrt{[\hat{\mathbf{R}}]_{mm}[\hat{\mathbf{R}}]_{nn}}} \quad (3.17)$$

where $\hat{\mathbf{R}}$ can be calculated using (3.13).

Due to the symmetry property of the Eleven antenna (cf. Section 3.2.2), only the embedded radiation efficiencies at P1 of the two-port Eleven antenna and P1 the three-port Eleven antenna are compared. Fig. 3.11 shows the measured embedded radiation efficiencies of the Eleven antennas at both chambers. There are good agreements over most of the frequency range. Note that the used 180° hybrids are the dominant contributor to the total embedded radiation efficiency at P1 of the two-port Eleven antenna, and that the mismatch and mutual coupling are the main contributions to the total embedded radiation efficiency at P1 of the three-port Eleven antenna. Fig. 3.12 shows the measured correlation magnitudes from both chambers. There is excellent agreement for the correlation of the two-port Eleven antenna. Although the correlation agreements between different ports of the three-port Eleven antenna is not as good as that of the two-port Eleven antenna, their agreement is acceptable, since it is difficult to measure small correlations accurately.

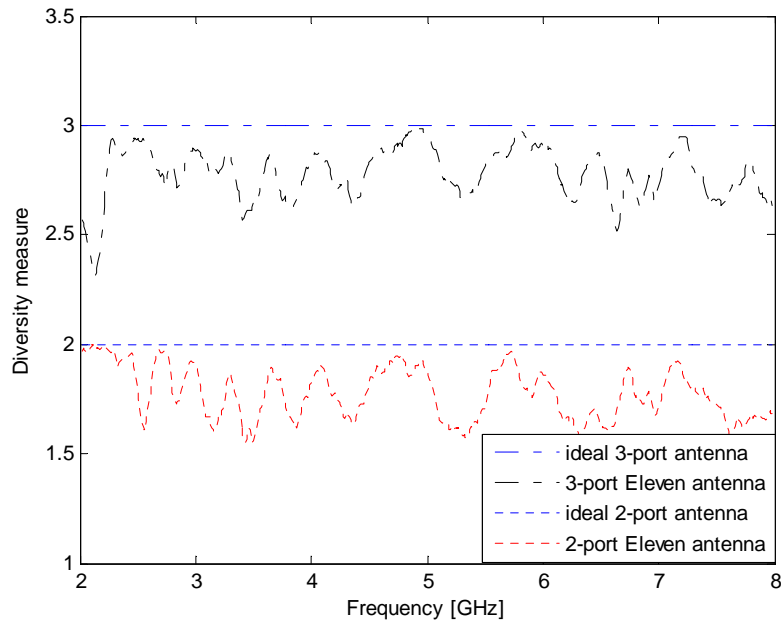


Figure 3.13: Comparison of diversity measures of the two-port and three-port Eleven antennas from RC measurements.

Note that the examination of the correlation of a two-port antenna is easy, since it only requires one correlation coefficient. However, for arbitrary multi-port antennas, the number of corresponding correlation coefficients can be large, i.e.

$$\binom{N}{2},$$

where N in the binomial coefficient denotes the number of antenna ports. For example, in general it requires three and six correlation coefficients to specify the correlation performance of three- and four-port antennas, respectively. One way to circumvent this problem is to use the diversity measure [80],

$$\Psi(\mathbf{R}) = \left(\frac{\text{tr}(\mathbf{R})}{\|\mathbf{R}\|_F} \right)^2 \quad (3.18)$$

where tr denotes the trace, and the subscript F of the norm denotes the Frobenius norm [81]. The advantage of the diversity measure (compared with correlation coefficients) is that it requires only one scalar parameter to characterize the overall correlation performance of the multi-port antenna, i.e. it maps a positive semidefinite matrix to a scalar value. The range of the mapping is $[1, N]$, where 1 denotes 100% correlation and N means no correlation. Note that although it is a special application of the majorization theory [82], which only gives partial ordering (meaning there exist covariance matrices that cannot be ordered), the diversity measure offers total ordering (meaning any two covariance matrices can be ordered). Fig. 3.13 shows the diversity measure of the two- and three-port Eleven antennas, together with that of the corresponding ideal diversity measure. It can be seen that except for the large correlation between P1 and P2 of the three-port Eleven antenna at low frequencies (at which frequencies the two ports forms a loop, see Fig. 3.8), the diversity measures of the Eleven antennas approach their maximal values periodically.

The MRC EDG of the two-port and three-port Eleven antennas based on the RC and AC measurements are shown in Fig. 3.14, as a function of frequency. As expected, the EDGs measured from both chambers agree with each other well over most of the frequency range. Since the corresponding EDG values of ideal antennas (with i.i.d. channels) are independent of frequency, a single value for each case is given in the captions of Fig. 3.14.

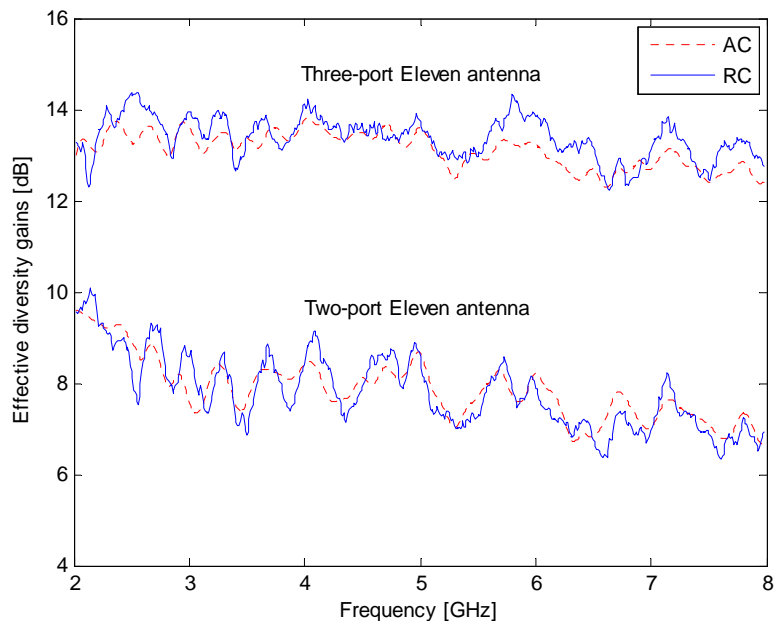


Figure 3.14: Comparison of MRC EDGs of two-port and three-port Eleven antennas from AC and RC measurements. The corresponding ideal two-port and three-port antennas (with i.i.d. channels) have EDGs of 11.7 and 16.4 dB, respectively.

3.3 MIMO Capacity Evaluation

It has been shown that ergodic capacities of MIMO systems can be measured readily in RCs [13], [17]. However, the capacity evaluation in an AC is not that straightforward in that there

is no random channel to sample in the AC. Therefore, before going into capacity measurements, a method (i.e. embedded far-field function method) for capacity evaluation based on AC measurement is presented. The presented method is compared with the so-called Z-parameter method [83] by simulations. Good agreements are observed. Then, an analogous S-parameter method is presented and verified based on the RC measurement using a narrowband portable antenna. After that, the embedded far-field function method, which is more suitable for measurements, is applied to compare the AC measurement with that of the RC. The two- and three-port Eleven antennas are used again for the AC and RC measurement comparisons. Note that the term capacity in this chapter is slightly abused from the information-theoretic point-of-view, but this should not cause any problem for MIMO antenna characterizations provided that the context is clear.

3.3.1 Embedded Far-Field Function Method

Assume that the receiver has a perfect channel state information (CSI), and that the transmit power is equally allocated among transmit antennas. The ergodic capacity of the multi-antenna system is [4], [5]

$$C_{N_r \times N_t} = E\{\log_2[\det(\mathbf{I}_{N_t} + \frac{\gamma}{N_t} \mathbf{H}_{N_r \times N_t} \mathbf{H}_{N_r \times N_t}^H)]\} \quad (3.19)$$

where $\mathbf{H}_{N_r \times N_t}$ is the MIMO channel matrix, N_t and N_r are number of transmit and receive antennas, respectively. The subscripts in (3.19) are dropped hereafter for notation convenience.

In order to focus on the characterization of a multi-port antenna, we assume the multi-port antenna under test is at the receive side and that the transmit antennas are ideal in the sense that they all have 100% efficiency and no correlation. The ergodic capacity including overall antenna effect can be expressed as

$$C = E\{\log_2[\det(\mathbf{I} + \frac{\gamma}{N_t} (\mathbf{R}^{1/2} \mathbf{H}_w)(\mathbf{R}^{1/2} \mathbf{H}_w)^H)]\} = E\{\log_2[\det(\mathbf{I} + \frac{\gamma}{N_t} \mathbf{R} \mathbf{H}_w \mathbf{H}_w^H)]\} \quad (3.20)$$

where \mathbf{H}_w denotes spatially white MIMO channel with i.i.d. complex Gaussian entries. \mathbf{H}_w is normalized so that its Frobenius norm satisfies $E[\|\mathbf{H}_w\|_F^2] = N_t N_r$. The physical meaning of this normalization is that every sub-channel (entry of the channel matrix) should have unity average channel gain so that only small-scale fading comes into play.

From (3.20) it is easy to show that \mathbf{R} is a sufficient statistic of the capacity. As shown in the previous section, \mathbf{R} (3.16) can be constructed from embedded far-field functions and efficiencies of the multi-port antenna. Since embedded radiation efficiencies obtained from the AC measurement is based on measured embedded far-field functions as well, the corresponding method is referred to as the embedded far-field function method. For a power-balanced multi-port antenna with a scalar embedded radiation efficiency of e_{emb} , \mathbf{R} becomes $e_{emb} \mathbf{\Phi}$, and (3.20) reduces to [17]

$$C = E\{\log_2[\det(\mathbf{I} + \frac{\gamma e_{emb}}{N_t} \Phi \mathbf{H}_w \mathbf{H}_w^H)]\} \quad (3.21)$$

where Φ is given in (3.16). Up to this point, the embedded far-field function method in [17] has been extended to arbitrary multi-port antennas. Based on the generalized method, MIMO capacity of any multi-port antenna can be calculated based on measurements in an AC.

Mutual coupling effects exist ubiquitously in multi-port antennas. It has effects on both the embedded radiation efficiency and the correlation (and therefore on diversity gain and capacity). The presented diversity and capacity formulations so far have dealt with mutual coupling implicitly via embedded radiation efficiencies and embedded far-field functions, which are measured at the corresponding ports with the other ports being terminated with 50-ohm loads. In the following subsection, another method that explicitly deals with the mutual coupling is presented and compared with the embedded far-field function method.

3.3.2 Comparison with Z-Parameter Method

For analysis convenience, open-circuit (o.c.) far-field functions (and o.c. correlations) of multi-port antennas are often employed in the literature, e.g. [83]-[88]. In this case, the mutual coupling has to be addressed explicitly. Often the mutual coupling effects are included via antenna and load impedance matrices. Due to this reason, this method is referred to as Z-parameter method [83]. Using the Z-parameter method, the MIMO channel that includes the overall antenna effect can be expressed as

$$\mathbf{H} = 2\sqrt{r_R r_T} \mathbf{R}_L^{1/2} (\mathbf{Z}_L + \mathbf{Z}_R)^{-1} \mathbf{H}^{oc} \mathbf{R}_T^{-1/2} \quad (3.22)$$

where \mathbf{R}_L and \mathbf{R}_T (r_T and r_R) are respectively the resistances of the transmit and receive multi-port (single-port) antennas, $\mathbf{H}^{oc} = \Phi_R^{oc,1/2} \mathbf{H}_w \Phi_T^{oc,1/2}$ with Φ_R^{oc} and Φ_T^{oc} denoting the o.c. correlation matrices, which can be calculated using the last equation in (3.16) by replacing the embedded far-field functions with corresponding o.c. far-field functions. The derivation of (3.22) is shown in Appendix C.

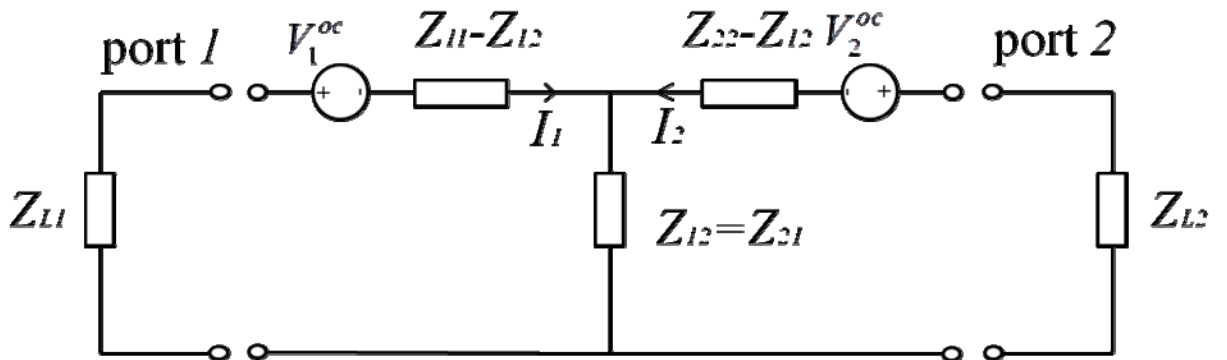


Figure 3.15: Equivalent circuit of parallel dipoles [93].

Despite the popularity of the Z-parameter method in MIMO antenna literatures, it is found that the channel normalizations in different literatures differ with each other, which may cause confusions. The derivation of (3.22), in Appendix C, follows the same physical normalization as (3.15), and therefore enables fair comparison with the embedded far-field function method.

Also note that this thesis assumes Kronecker (channel) model, i.e. separable transmit and receive correlations. The Kronecker model was first conjectured in [90], [91], then verified by simulations [92] and measurements [8]-[10]. It is pointed out in [11], however, that the Kronecker model does not hold for MIMO systems with more than four antennas at either side. Nevertheless, this thesis only considers portable MIMO terminals whose antennas are usually limited to a number that is smaller than four. Therefore, it is assumed that Kronecker model holds throughout this thesis.

In order to compare the embedded far-field function method with the Z-parameter method, two parallel half-wavelength dipoles (see Fig. 3.15 for its equivalent circuit) are used as an example. The dipole antennas are used as receive antennas, and two ideal antennas are used at the transmit side. The isolated (o.c.) and embedded far-field functions of the dipoles are, respectively [62], [94]

$$\begin{aligned}\vec{G}_i(\theta, \phi) &= -\hat{\theta} \frac{2C_k \eta \cos(\pi/2 \cos \theta)}{k \sin \theta} \exp(jk \frac{d_i}{2} \sin \theta \sin \phi), \\ \vec{G}_{emb,1}(\theta, \phi) &= \vec{G}_1(\theta, \phi)I_1 + \vec{G}_2(\theta, \phi)I_2, \\ \vec{G}_{emb,2}(\theta, \phi) &= \vec{G}_1(\theta, \phi)I_2 + \vec{G}_2(\theta, \phi)I_1.\end{aligned}\tag{3.23}$$

where $i = 1, 2$, $d_1 = -d$, $d_2 = d$, $C_k = -jk/4\pi$, and η is the free-space wave impedance.

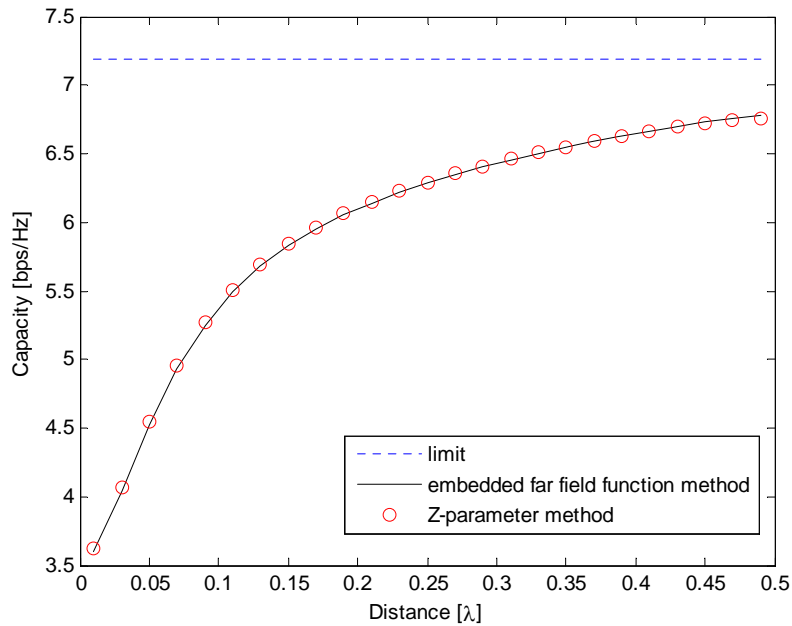


Figure 3.16: Ergodic capacities at 13-dB SNR in an isotropic scattering environment with Z-parameter method and embedded far-field function method.

Note that in general the isolated far-field functions and the corresponding o.c. ones are not the same for arbitrary antennas. They are the same when the antenna in question can be regarded as minimum-scattering antenna [96], which approximately holds with good accuracy for a half-wavelength dipole. Also note that for notation convenience, the EM vector expressions are used here for the antenna patterns, instead of the otherwise sparse vectors as shown in (3.16). From simple circuit theory, when the excitation current at the port 1 is unity, i.e. $I_1 = 1$, $I_2 = -Z_{12}/(Z_{11}+Z_s)$. The embedded radiation efficiencies can therefore be calculated as

$$e_{emb,j} = \left(1 - \left| \frac{z_{in,j} - z_{L,jj}^*}{z_{in,j} + z_{L,jj}} \right|^2\right) \left(1 - \frac{r_{L,jj} \sum_{i=1, i \neq j} |I_i|^2}{\text{Re}\{z_{in,j}\} |I_j|^2}\right), \quad (3.24)$$

$$z_{in,j} = z_j + \frac{1}{I_j} \sum_{i=1, i \neq j} z_{ji} I_i.$$

The analytical expressions for the self- and mutual-impedances of the parallel dipoles can be found in [95]. Fig. 3.16 shows the ergodic capacities (as functions of dipole separation) in an isotropic scattering environment (e.g. RCs) at 13-dB SNR with 50-ohm loads using both the Z-parameter and embedded far-field function methods. As expected, both methods result in the same capacity values.

It is shown in [97], using the example of parallel dipoles, that both methods give identical correlation coefficients under different matching conditions. The Z-parameter method is often used because it facilitates the analysis of impedance matching on the MIMO capacity. In certain simplified cases, it is possible to derive optimal impedances (w.r.t. the ergodic capacity) based on the gradient-based optimization [98]. Nevertheless, it is difficult to measure o.c. far-field functions in practice and that the Z-parameter method is only valid for antennas with little ohmic losses. Therefore, the embedded far-field function method is more suitable for measurement-based evaluations.

3.3.3 S-Parameter Method

Analogous to the Z-parameter method, a slight modification of the far-field function method which involves free-space scattering-parameters (S-parameters) of the antennas, i.e. S-parameter method, is presented in this subsection. Like the Z-parameter method, this method only holds for antennas with little ohmic losses. Nevertheless, since the free-space S-parameters can be easily measured with a good accuracy in an AC, the S-parameter method is much easier to use compared with the far-field function method, provided the AUT has negligible ohmic losses.

The S-parameter method differs from the embedded far-field function method only in calculations of the embedded radiation efficiencies and the correlation coefficients of an N -port antenna. The former and latter can be expressed respectively as [99]-[101]

$$e_{emb,i} = 1 - \sum_{i=1}^N |S_{i1}|^2,$$

$$[\Phi]_{mn} = \frac{-\sum_{i=1}^N S_{mi}^* S_{in}}{\sqrt{\prod_k \left(1 - \sum_{i=1}^N S_{ki}^* S_{ik}\right)}}. \quad (3.25)$$



Figure 3.17: Photo of the two-port portable antenna used for verifying S-parameter method.

As a result, the capacity can be calculated using the S-parameter method with only measured S-parameters and numerically generated random channel realizations (cf. Section 3.3.1 and [89]).

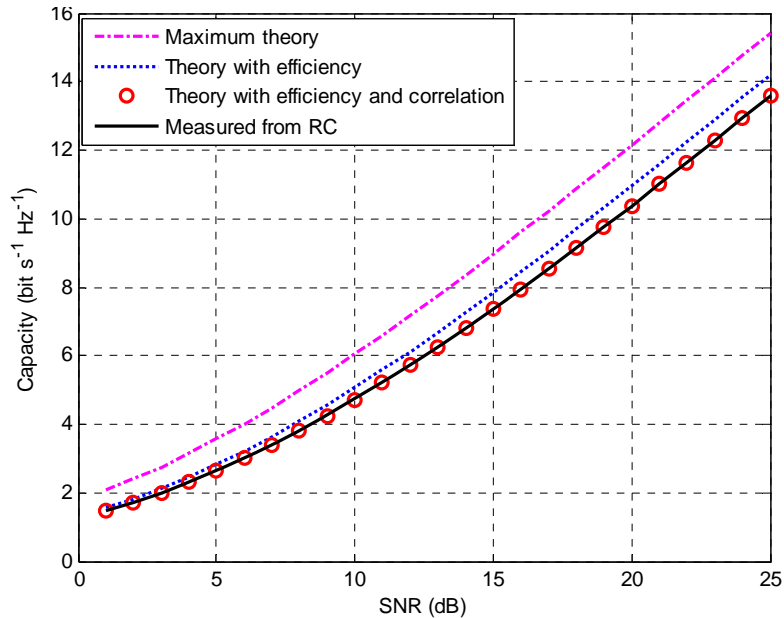


Figure 3.18: Ergodic MIMO capacity. The curves show the degradation from the theoretical maximum due to embedded element efficiency and correlation, evaluated using S-parameter method, and agreement with capacity based on RC measurement.

Since the Eleven antenna has a nonzero ohmic loss, it cannot be used to verify the S-parameter method. Instead, a narrowband portable two-port antenna (see Fig. 3.17) which has negligible ohmic losses is used. It has a resonating frequency of 1.6 GHz. Other detailed information about the antenna can be found in [102]. Measurement of this antenna was done in the Bluetest HP RC with the same measurement setup (i.e. 20 platform positions, 10 stirrer plate positions, and three wall antennas) as before (cf. Section 3.2.3). For the MIMO capacity evaluation, the three wall antennas in the RC are regarded as three transmit antennas, the AUT (in this case the Eleven antenna) is regarded as receive antenna. Therefore, instead of 600 channel samples per frequency point as for diversity measurement in the RC, there are 200 MIMO channel samples per frequency point. Due to the fact that the AUT has a bandwidth slightly larger than 10 MHz w.r.t -10 dB $|S_{11}|$, the frequency stirring bandwidth is set to 10

MHz (for the reason given in Section 3.1). Thus, there are 2000 MIMO channel samples for the capacity evaluation.

The (normalized) measured MIMO channel is

$$\mathbf{H} = \mathbf{H}_{meas} / \sqrt{P_{ref}}. \quad (3.26)$$

The S-parameters of the AUT was conveniently measured in the AC at Chalmers. In order to see the effects of the total embedded radiation efficiency and the correlation coefficient on the capacity, the ergodic MIMO capacities for the following four cases are plotted in Fig. 3.18: assuming 100% efficiency and zero correlation (i.e. ideal AUT with i.i.d. channels); including the measured efficiency; and including both efficiency and correlation; and the ergodic MIMO capacity obtained from the measured channel samples in the RC using (3.19). It is seen that the total embedded radiation efficiency reduces the capacity, and that the correlation reduces it further, and that the S-parameter method results in an excellent agreement with the RC measurement. Besides giving illustrations of the efficiency and correlation effects on the MIMO capacity, Fig. 3.18 also verified the S-parameter method. Note that there are 2000 numerically generated random i.i.d. channel realizations for the S-parameter method in order to make a fair comparison with the RC measurement.

3.3.4 RC and AC Measurement Results

For a general comparison between the measured MIMO capacities in the RC and the AC, the Eleven antenna is used (for the same reason as that given in Section 3.2.2). The far-field function method is used for the AC measurement-based evaluation. Actually, the measurements are the same as the corresponding diversity measurements in the RC and the AC (cf. 3.2.3). In other words, the same measurement data (from diversity measurements) are used here for MIMO capacity evaluations. The comparisons of embedded radiation efficiencies and correlation magnitudes based on the AC and RC measurements are shown in Figs. 3.11 and 3.12. As explained in the previous subsection (assuming the three wall antennas as three transmit antennas), instead of 12000 channel samples as for the diversity evaluation, there are 4000 MIMO channel samples (including a 20-MHz frequency stirring) for the capacity evaluation. For fair comparison between RC and AC measurements, 4000 random MIMO channel realizations are generated numerically for the embedded far-field function method that are used for the evaluation of the AC measurement. Fig. 3.19 shows the ergodic capacities of the two-port and three-port Eleven antennas as functions of frequency at 10-dB SNR based on the AC and RC measurements. Again good agreements are observed. Note that for better illustrations, the corresponding ergodic capacity values of ideal antennas (with i.i.d. channels) are not plotted in the same figure. Since the ideal case values are independent of frequency, a single value for each case is given in the caption of Fig. 3.19.

The (estimated) ergodic capacity is the average of all the instantaneous capacity estimates. Since the instantaneous capacity depends on the channel state, it is itself a random variable. Therefore, a closer look at the capacity would be comparisons of the empirical CDF of the instantaneous capacity. Figs. 3.20 and 3.21 show the empirical CDFs of the capacities of the two-port and three-port Eleven antennas, respectively, at a few frequencies (i.e. 3, 5, and 7.5 GHz) with 10-dB SNR. As expected, there are acceptable agreements, in general, between the empirical CDFs. At the frequencies where mismatches occur (e.g. $f = 3$ GHz for the two-port Eleven antenna), the corresponding ergodic capacities deviate from each other. For

comparisons, the empirical CDFs of the corresponding ideal antennas (with i.i.d. channels) are also calculated and plotted. As mentioned earlier, the capacity degradation is mainly due to the ohmic loss introduced by the 180° hybrids (and the strong mutual coupling between P1 and P2 of the three-port Eleven antenna).

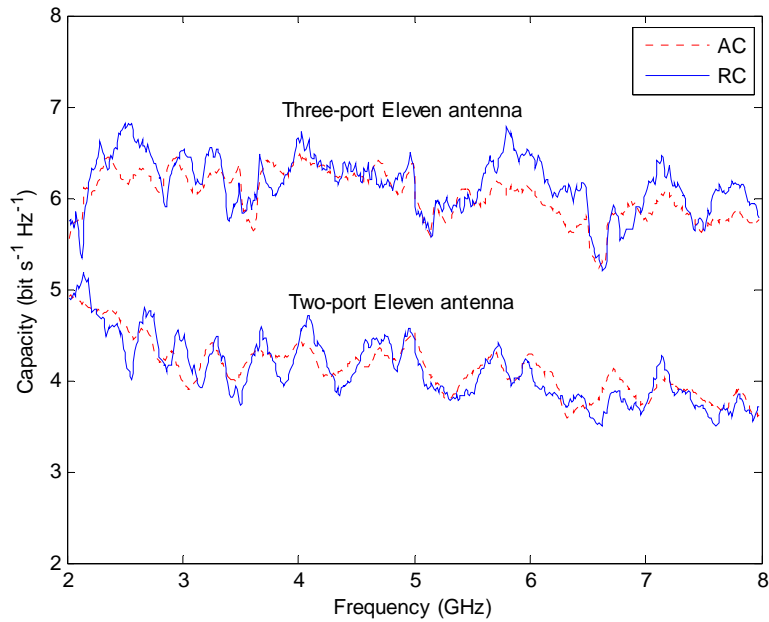


Figure 3.19: Comparison of ergodic capacities of two-port and three-port Eleven antennas from AC and RC, both at 10-dB SNR. The corresponding ideal two-port and three-port antennas (with i.i.d. channels) have ergodic capacities of 6.0 and 8.2 bps/Hz, respectively.

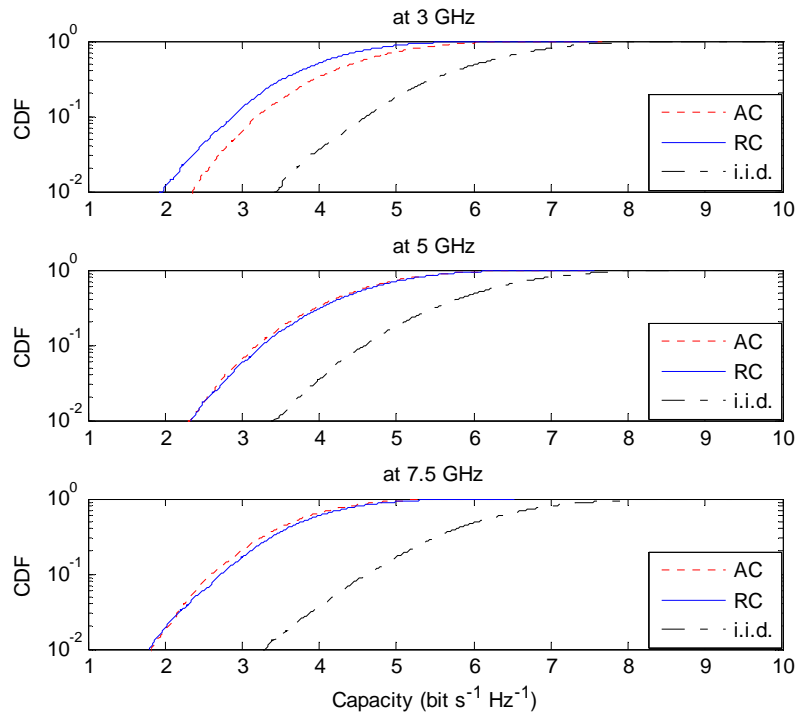


Figure 3.20: Comparison of empirical CDFs of capacities (at different frequencies) of two-port Eleven antennas from anechoic AC and RC, all at SNR of 10 dB.

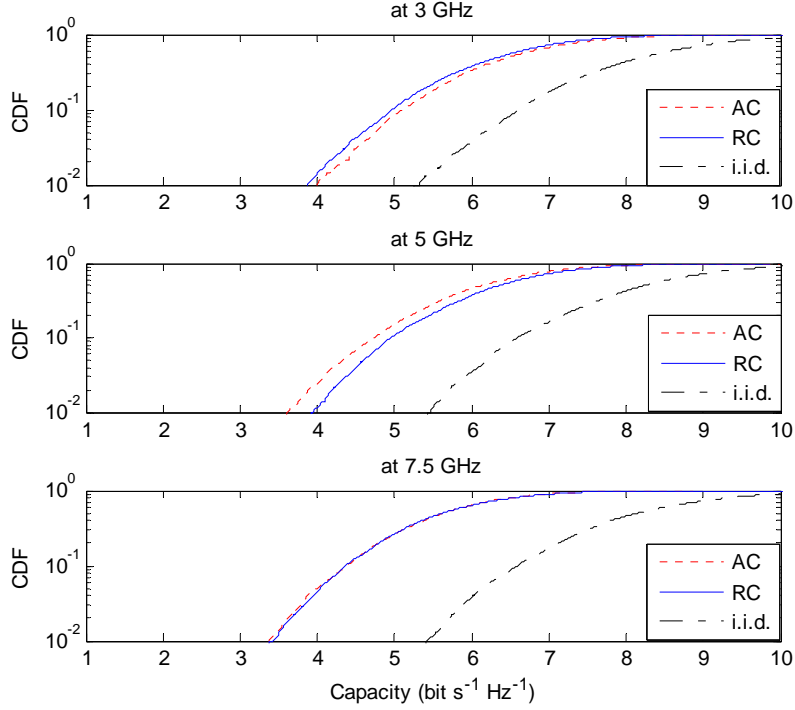


Figure 3.21: Comparison of empirical CDFs of capacities (at different frequencies) of three-port Eleven antenna from AC and RC, all at SNR of 10 dB.

It is non-trivial to determine the capacity (and diversity) measurement uncertainty, for it requires, in principle, many independent repetitions of the same measurement procedure many times. Given the fact that the embedded far-field function measurement for one port of the Eleven antenna took 10 hours in the DTU AC, and that the measurement is costly, thus no effort is exerted in determining the capacity measurement uncertainty by repeated measurements. Instead, Monte Carlo simulations are used based on a priori knowledge of the efficiency measurement uncertainty in each chamber.

For heuristic purpose, the power-balanced two-port Eleven antenna is used as an example for the analysis of the capacity uncertainty. It is shown from (3.21) that the capacity depends on the antenna efficiency and the correlation. Thus, the uncertainty of the capacity measurement depends on the uncertainty of the efficiency and correlation measurements. At the high SNR regime, the capacity is given by [5],

$$C = K \log_2 \gamma_{eff} + o(1) \quad (3.27)$$

where $\gamma_{eff} = \gamma e_{emb}$ is the effective SNR, K denotes the rank of \mathbf{H} , and $o(1)$ vanish at the high SNR. While the correlation implicitly affects the capacity via K , the efficiency uncertainty affects the capacity explicitly by $\Delta\gamma_{eff} = \gamma\Delta e_{emb}$, where Δe_{emb} is the estimated efficiency error. Using the Taylor expansion of (3.27), the estimated capacity error can easily be derived as

$$\Delta C = \frac{K / \ln 2}{\gamma_{eff}} \Delta\gamma_{eff} = \frac{K / \ln 2}{e_{emb}} \Delta e_{emb}. \quad (3.28)$$

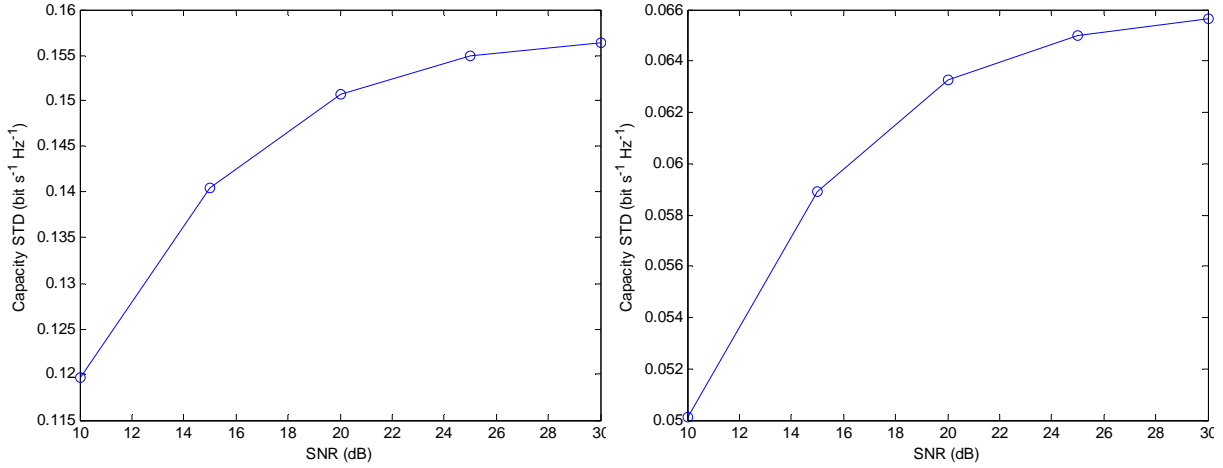


Figure 3.22: STD of simulated capacity due to efficiency uncertainty in RC (left) and AC (right).

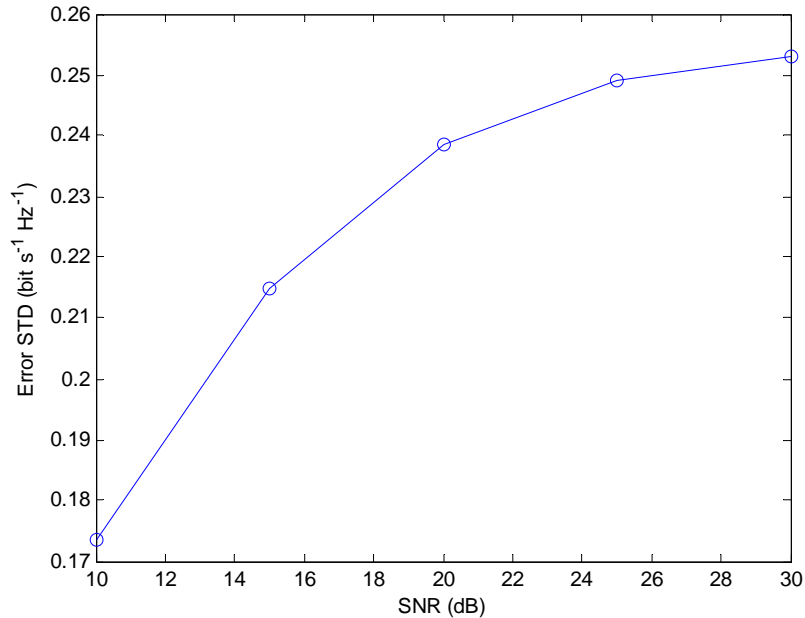


Figure 3.23: STD between measured capacities in RC and AC evaluated over the frequency band of 2-8 GHz.

It can be seen from (3.28) that the uncertainty (STD) of the capacity is proportional to the uncertainty (STD) of the efficiency. Based on this observation and given the fact that the uncertainties of measured antenna efficiencies in both chamber are known empirically, it is possible to determine the uncertainty based on (3.21) using numerically generated random channel realizations. The STD of the efficiencies measured in the Bluetest RC is less than 0.5 dB [103], whereas in the AC at DTU it is stated to be approximately 0.2 dB [104]. Random efficiency errors with the corresponding uncertainties are introduced separately for ergodic capacity calculations at different SNRs for both chambers. By repeating this procedure 50 times, the STDs of the estimated capacity errors are estimated for both chambers. Fig. 3.22 shows the contributions of the efficiency uncertainties to the capacity measurement uncertainties for the RC (left) and the AC (right). Although obtained via numerical simulations, the simulated capacity uncertainty (as a function of SNR) has similar trend of the

measured one (see Fig. 3.23) that is calculated as follow: assume the measurement errors in different chambers are independent and that the channel is wide sense stationary in the frequency domain (i.e. US assumption), the total uncertainties from both chambers can be obtained by calculating the standard derivations (STDs) of their capacity differences averaged in the frequency domain.

From both the measured and simulated capacity uncertainties (Figs. 3.23 and 3.22), it is seen that the capacity measurement uncertainty increases as increasing SNR, which is reasonable, since the efficiency error is multiplied by the SNR in the capacity formula (3.21). Moreover, it is found that the capacity STD slope (as a function of SNR) is approaching zero asymptotically (at the high SNR regime). This can be explained from (3.28), where it is shown that the capacity measurement error is independent of the SNR (yet proportional to the relative error of the antenna efficiency) at the high SNR regime.

It is shown in [105] that capacities depend on correlations only via Frobenius norms of covariance matrices. As a simple corollary, capacities depend on correlation magnitudes rather than (complex) correlations themselves. Hence, for the simulation of the correlation uncertainty contribution, only real-valued random correlation errors are generated. The STD (over frequency) of correlation difference between the RC and AC measurements is 0.08, which means that the correlation STD in either chamber is smaller than 0.08. The capacity STD due to the correlation uncertainty of 0.08 STD is obtained using a similar simulation procedure. It shows that the contribution from the correlation uncertainty is much smaller than the contribution from the efficiency uncertainty [106]. There are other minor contributions to the system error, such as VNA calibration drifting during the measurement, hardware calibration error, the perfect symmetric assumption of the Eleven antenna (cf. Sections 3.2.2 and 3.2.3), etc. However, the efficiency uncertainty in the RC is found to be the major contribution to the capacity uncertainty. And therefore, more effort should be exerted on improving the accuracy of the efficiency measurement for RC designs, which is discussed in the next chapter.

The better accuracy of the AC measurement is at the expense of the prolonged measurement time (that is almost 7 times longer than that of the RC measurement), and that the accuracy of the RC measurement is reasonably small already. Note that the good efficiency accuracy in the AC is based on the fact that the Eleven antenna is directive. For non-directive portable antennas (e.g. mobile phone antennas), the efficiency accuracy in the AC will degrade (becomes more or less the same as, if not worse than, that in the RC), whereas the 0.5-dB efficiency uncertainty in the RC holds for non-directive small antennas as well. This is because that the efficiency measurement in the AC relies on the antenna radiation pattern, where a directive radiation pattern is desirable, while the efficiency measurement in the RC depends on the measured power level, which is less dependent of the antenna pattern (actually non-directive antennas are more favorable for RC measurements). Therefore, for non-directive antennas, the superiority of the AC measurement will vanish.

Note that the 0.5-dB efficiency uncertainty in the RC is for the normal measurement setup (i.e. 20 platform positions, 10 stirrer plate positions, and three wall antennas) that has been used in this thesis so far for the Bluetest HP RC measurement. In the next chapter, it will be shown that the measurement uncertainty depends on the measurement setup, and that by increasing the stirrer positions up to a maximum independent number (that is frequency dependent), a better accuracy can be achieved. Also note that the improved measurement accuracy in that case is at the expense of the prolonged measurement time.

3.4 Throughput Measurement

The RC has been used for active mobile phone measurements [23], [107]. It is shown in [108] that such BER-based measurement become similar to those measured in real-life environments provided that the chamber is appropriately loaded. The throughput of the multi-antenna system has been measured in [21], [22], [24]. This section is a brief documentation of the findings in [21], where interested readers can find more details. Here some alternative interpretations of the throughput model is presented based on the information-theoretic model: The outage theorems in [109] show that, with powerful hybrid-automatic-repeat-request (H-ARQ) coding [110], the frame error rate can be well approximated by the (instantaneous) capacity's outage probability. This motivates and confirms the threshold receiver [113] proposed in [21]. Based on this assumption, the throughput is basically the multiplication of the maximum transmission rate and the complementary CDF of the capacity.

The throughput measurement setup is shown in Fig. 3.24. The RC in use is an upgraded version of the Bluetest HP RC, i.e. Bluetest RTS60 RC [35] (comparisons of these two RCs are given in the next chapter). A commercial communication test instrument was used as the base station simulator. The DUT is the Huawei E398 LTE USB dongle with external radio frequency (RF) ports for OTA tests. The USB dongle was located in a separate shielded box outside the RC. It is connected with two discone antennas (via RF cables) that are located inside the RC. For the sake of modeling simplification, the two discone antennas are orthogonally placed with sufficient separation, so that the antennas can be regarded as uncorrelated. Note that the dongle's built-in antennas are not connected once the external RF ports are used. To simplify the analysis even more, the OTA testing system was constraint to the 1×2 MISO and the 2×1 SIMO. Instead of the step-wise stirring sequence that is used in all the previous measurements, this measurement setup uses the continuous stirring sequence for faster measurements. That is the plate stirrers and the turn-table platform inside the RC are continuously moving during the measurement. Furthermore, during the measurement, the RC is loaded to achieve a RMS delay spread of 90 ns (corresponding to 3-MHz coherence bandwidth [27]). The 3-MHz coherence bandwidth is motivated by the work of Jung [111], where it was shown by extensive real-life measurements that typical indoor environments usually have a coherence bandwidth of about 3 MHz. Measurements were performed on the LTE band 7, i.e. channel 3100 (2655 MHz), with a bandwidth of 10 MHz. The OTA testing system was set to a fixed modulation of 64 QAM with a maximum rate of 24 Mbps.

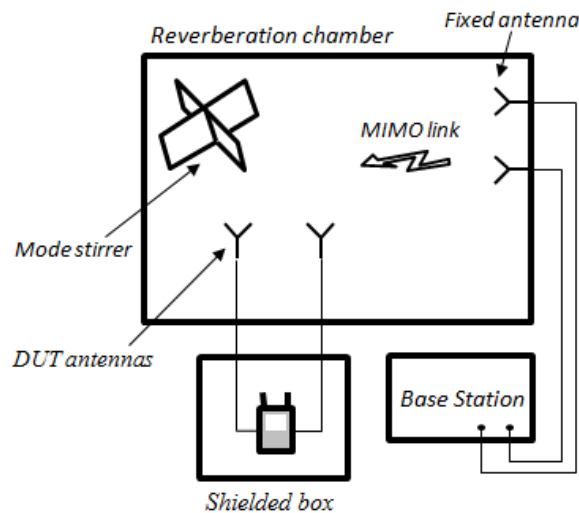


Figure 3.24: Throughput measurement setup in RC.

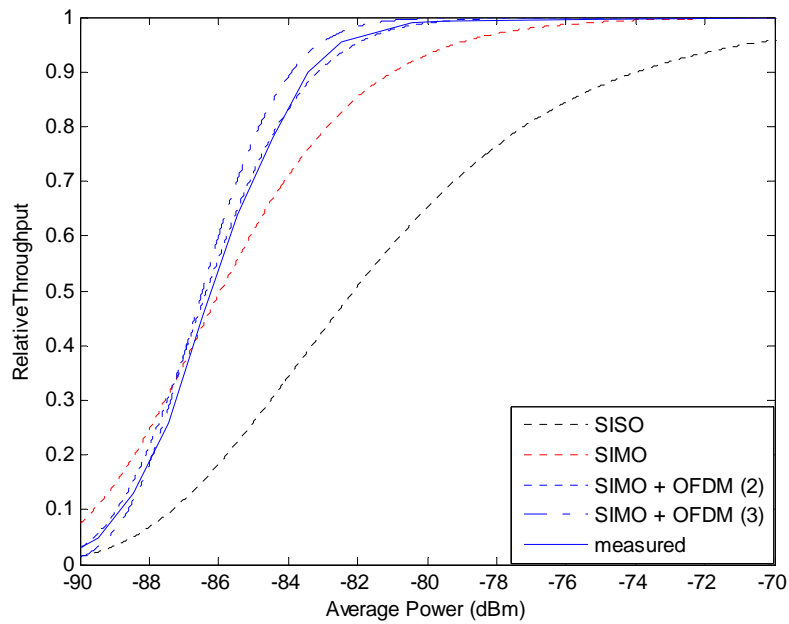


Figure 3.25: Relative throughput models (dotted and dash-dotted curves) from one receive antenna (SISO) to two receive antennas (SIMO) and finally include different frequency diversity orders, i.e. SIMO + OFDM (frequency diversity order), against that of the measured one (solid curve).

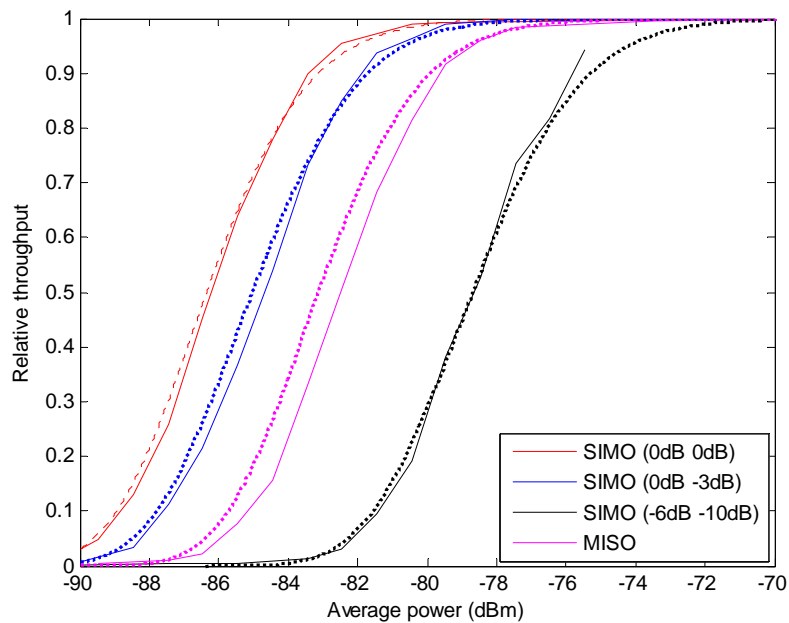


Figure 3.26: Measured (solid curves) and modeled (dotted curves) relative throughput for different cases of power imbalances between the two receive branches of the USB dongle. The dB values in the bracket denotes the effective radiation efficiencies of the receive antenna including different attenuators.

The SIMO and MISO simplifications make the MRC and maximum ratio transmission (MRT) suitable models to predict the measured throughput. However, the orthogonal frequency division multiplexing (OFDM) technique (that is introduced in [112] first) used in the LTE system has to be taken care of. The OFDM effectively partition the wideband channel into

subchannels each with a smaller bandwidth. Hence, intuitively the number of effective (or uncorrelated) subchannels can be approximated by dividing the system bandwidth (10 MHz) by the coherence bandwidth (3 MHz). However, as can be seen from the definition of the coherence bandwidth (cf. Section 2.1), two subchannels with a separation larger (but not much larger) than 3 MHz still have a nonzero correlation. Moreover, the channel partition by OFDM is not strictly performed in the frequency domain (but rather in tone-domain defined by discrete Fourier transformation) [50]. Given these facts, the actual effective subchannel number (or equivalently the frequency diversity order) must be found out empirically.

Fig. 3.25 shows the measured relative throughput against different throughput model with/without the MRC and the OFDM. It shows that by assuming a frequency diversity order of 2 (i.e. two effective subchannels) together with the MRC, the relative throughput can be accurately estimated. Note that a similar MRC and OFDM model has been used in [114] to emulate the throughput of a 2×1 SIMO system in Nakagami- m fading environments. Although the Nakagami- m fading includes Rayleigh fading (e.g. RCs) as a special case, the result in [114] does not apply here in that [114] only studied uncoded BER performance, where the advanced error-correcting coding existing in the LTE system is not considered.

To further verify the presented model, the same measurement procedure is repeated with the receive antennas connected with different attenuators. Fig. 3.26 shows the measured and modeled relative throughputs for different antenna attenuations (i.e. 3 dB, 6 dB, and 10 dB). Good agreements are observed. Interestingly, it can be seen that the SIMO (without attenuator, i.e. 0 dB) and MISO throughputs differ by 3 dB at all throughput levels. This is because the receiver has the CSI while the transmitter does not. In such a CSIT (CSI at the transmitter) uninformed V-BLAST [3] system, the MISO communications can be built reliably via space-time coding (e.g. Alamouti coding [115]), but a 3-dB receive power gain (or using the communications term, array factor [6]) is lost compared with that of a CSIR (CSI at the receiver) informed 2×1 SIMO system. Comparisons in Fig. 3.26 show that the presented throughput model can well predict the measurement results.

As mentioned in the introduction, although the ultimate goal of this thesis is MIMO terminal characterizations and tests as shown in this chapter, the measurement accuracy is of vital importance, for an inaccurate measurement gives little useful information, or even worse, leads to wrong conclusions. Therefore, the next chapter is devoted to characterizations of the RC measurement uncertainty.

4. Measurement Uncertainty Characterizations

In this chapter the RC measurement uncertainty is studied in details. First a procedure for assessing the (measurement) uncertainty is presented. Then, an uncertainty model is devised. Measurements show that this uncertainty model can well predict the actual measurement uncertainty.

4.1 Procedure of Uncertainty Assessment

The measurement uncertainty can be assessed by repeating the reference measurement (i.e. measurement of the power transfer function using the reference discone antenna, cf. Section 2.1) several times with different positions and orientations of the reference antenna inside the RC. Due to limitations of the RC space and the measurement time, three heights and three orientations (vertically, horizontally and at 45 deg relative to the vertical) of the reference antenna are chosen. Therefore, there are in total nine reference measurements for assessing the measurement uncertainty for a certain loading at each frequency point. And the uncertainty, for this loading condition, is characterized by the STD of the nine average power transfer functions normalized by their mean. To evaluate the uncertainties for different loading conditions, one needs to repeat the uncertainty assessment procedure with corresponding loading conditions of the RC.

4.2 Uncertainty Model

Traditionally, it was believed that the RC measurement uncertainty (in terms of the STD σ) depends solely on its independent sample numbers N_{ind} ,

$$\sigma = 1 / \sqrt{N_{ind}}. \quad (4.1)$$

Equation (4.1) comes from the basic statistics, e.g. [74], assuming that the variance of the individual sample has been normalized to one (for notation convenience and without loss of generality, this section assumes that the samples are with a unity variance). Therefore, pervious RC uncertainty studies only focus on the independent sample number, e.g. [116]. It was first pointed out in [117] that the (Rician) K-factor represents a residual error in a RC measurement, meaning that the RC accuracy cannot be improved by simply increasing independent sample number and that the RC accuracy is limited by the K-factor, given enough independent samples. Interestingly, it is found that the authors of [33] have used the K-factor as an objective function (that is to be minimized) to optimize their RC mode-stirrers.

The original model presented in [117] was improved and presented in [35] with extensive measurement validations. It is given as

$$\sigma = \sqrt{(\sigma_{NLOS})^2 + K_{av}^2 (\sigma_{LOS})^2} / \sqrt{1 + K_{av}^2} \quad (4.2)$$

where σ_{NLOS} is the STD contribution from the stirred EM fields, σ_{LOS} is the STD from the random line-of-sight (LOS) EM fields, and K_{av} is the average K-factor defined in [34]. Note

that σ in this thesis is presented in dB as

$$\sigma_{dB} = 5 \log[(1 + \sigma) / (1 - \sigma)]. \quad (4.3)$$

The dB transformation defined in (4.3) ensures a close-to-linear mapping when σ is small, which helps the visualization of the STD plots that are shown in Section 4.3. Note that similar dB transformation was used in [118] to represent the STD of the fading signal. Each of the ingredients of (4.2) is studied in the following subsections separately.

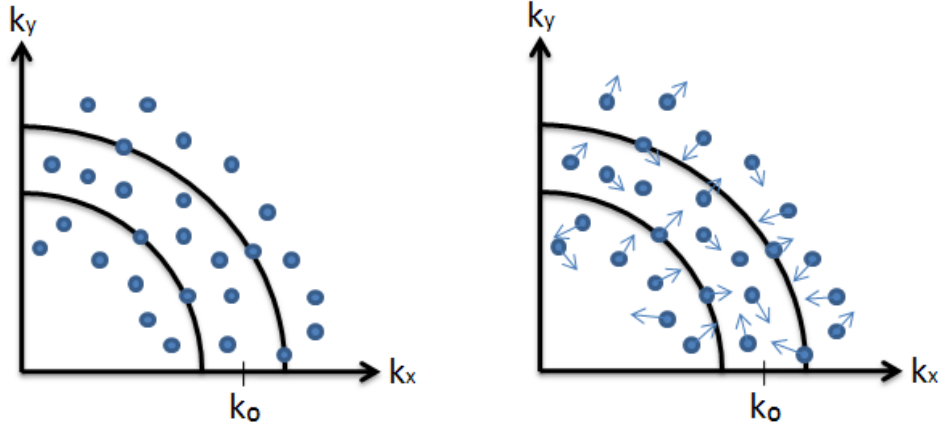


Figure 4.1: Mode distribution near resonating frequency in RC: stationary mode-stirrer (left); moving mode-stirrer (right).

4.2.1 Stirred Fields and Independent Sample Number

Ideally, EM fields in a RC can be expanded into orthogonally perturbed mode functions. These perturbed modes satisfy the boundary condition on mode stirrers as well as on cavity walls. The mode stirrers have the effect of shifting the eigen-frequencies of the EM modes, as illustrated in Fig. 4.1. Fig. 4.1 (left) is a two-dimensional (2-D) view of the mode distribution (represented by dots) when mode-stirrers in the RC are stationary, where $k_0 = 2\pi f_0 / c$ is the wave number corresponding to resonant frequency f_0 , with speed of light denoted as c . In practice, RCs always have finite Q-factors due to different losses [54], corresponding to a non-zero average mode bandwidth Δf [27]. With one excitation at f_0 all the modes falling within the spherical shell Δk will be excited. Δf is related to the thickness of Δk as $\Delta k = 2\pi\Delta f / c$. With moving mode-stirrers in the RC, the eigenmodes shift as shown in Fig. 4.1 (right). The amount of shift of the eigenmodes depends on the size, geometry, and moving sequence of the mode-stirrers. An effective mode-stirrer means the shift of the mode is large enough for it to be shifted in or out of the shell. In this way, the number of independent samples increases. As Wu [36] postulated, the key mechanism behind an effective mode-stirrer lies in the shifting of the eigen-frequencies. Therefore, it is necessary to define a mechanical stirring bandwidth, B_{mech} , to quantify the effectiveness of the mode-stirrers. Due to imperfect EM stirring of the mode stirrers, the EM fields in a RC can be partitioned as stirred and unstirred components. Obviously, the stirred components in the RC, which is Gaussian distributed [12], can be expressed as

$$\sigma_{NLOS} = 1 / \sqrt{N_{ind}}. \quad (4.4)$$

The number of independent samples N_{ind} can be determined primarily by the number of independent modes, which is related to the average mode bandwidth [27] and the mechanical bandwidth in the RC,

$$N_{mode} = \frac{Vf^2 8\pi}{c^3} (B_{mech} + \Delta f) \quad (4.5)$$

where the factor in front of the bracket is the well-known Weyl's formula, which well approximate the mode density [14]. However, it is non-trivial to determine B_{mech} in that it is believed to be sensitive to the chamber loading and the frequency and that it depends on mode stirring methods and sequences, shapes of mode-stirrers, and the shape of the chamber. As a result, a detailed study of B_{mech} is not available in the literature yet (except for [119], where the objective function for the stirrer is chosen to be the lowest frequency with a certain uncorrelated samples, which does not fit into the present uncertainty model). Therefore this thesis resorts to a simplified independent sample model (and the study of B_{mech} is left for future work):

$$N_{ind} = M_{plate} M_{pf,ind} M_{ant} \quad (4.6)$$

where M_{plate} is to the number of plate positions (or plate stirring number), M_{ant} is the number of antennas used for the polarization (or multi-probe) stirring, and $M_{pf,ind}$ is the number of independent platform positions that was found to be bounded according to

$$M_{pf,ind} = \max \left\{ 8, \min \left[M_{pf}, \frac{2R \sin(2\pi / M_{pf}) M_{pf}}{\alpha \lambda_c / 2} \right] \right\}. \quad (4.7)$$

Equation (4.7) is an extension of the formula introduced in [33], where M_{pf} is the number of platform positions, R is the radius of the circle along which the reference antenna moves during the measurement, and α is a parameter that needs to be determined empirically when the far-field function of the AUT is unknown. Note that since λ and λ_i have been reserved to representations of the eigenvalues (cf. Section 3.2) by following the notion convention of the matrix analysis, e.g. [81], the EM wavelength is denoted as λ_c here. The interpretation of (4.7) is that the independent platform position number is first upper bounded by the maximum independent platform number, and then lower bounded by a factor of 8. The maximum independent platform number is obtained by dividing the arc length that the reference antenna traveled by the coherence distance (or correlation length [39]). It is shown that the coherence distance for an isotropic antenna in the RC is $\lambda_c / 2$ [39], but it differs for practical antennas with non-isotropic far-field functions [25], [40], [41]. Hence α is introduced to take the reference antenna into account. Note that since the reference discone antenna is not very directive, the corresponding α was found to be 0.7 by curve fitting against the measured STDs. The factor of 8 in (4.7) comes from the fact that most of the EM wave in the RC can be decomposed into 8 plane waves [14].

4.2.2 Unstirred Fields and Average K-factor

It is shown in [32]-[34] that RCs can be loaded to emulate Rician fading environments, while an unloaded RC with properly designed mode-stirrers has a negligible K-factor when the transmit and receive antennas are not pointed towards each other [32] or non-directive [34]. Interestingly, the Rician distribution due to an unstirred component in a RC was previously studied in [120] but from an EMC point-of-view. For active OTA tests, it is often necessary to load the RC in order to have a desired coherence bandwidth (cf. Section 3.4). Therefore, K-factors (small as they might be) exist ubiquitously in various active OTA tests. The Rician K-factor is defined as the power ratio of the unstirred components to the stirred components [49],

$$K = \frac{|E[H]|^2}{\text{var}[H]} \quad (4.8)$$

where H is the channel transfer function in the RC (cf. Section 2.1), and var denotes the variance. Note that the unstirred components consists both LOS components and unstirred multipath components (UMCs) [32], since the UMC has the same effect as the LOS component in a (passive) RC measurement, both of them are referred to as LOS components in this thesis. Also note that in the literatures various moment-based approaches (that utilize the signal magnitude only), e.g. [122], were used for the K-factor estimation; the CRB [67] on the estimation error of this kind of estimators diverges as the K-factor approaches zero [123] (meaning that reliable a K-factor estimation using the moment-based approach is impossible when the K-factor is small). On the other hand, the CRB for the estimator (4.8) goes to zero as the K-factor vanishes; and it is strictly smaller than that of the moment-based estimator [123], meaning that the performance of (4.8) surpasses that of its moment-based counterpart. This is quite intuitive since the estimator (4.8) uses both the magnitude and phase information of the signal, which cannot be worse than the case where only signal magnitude is available. Since the magnitude and phase information can be obtained readily in a VNA measurement, (4.8) is used for the K-factor estimation in this chapter.

Because of the traditional definition of the K-factor, i.e. (4.8), the LOS components are usually regarded as deterministic. However, due to the (step-wise) rotation of the turn-table platform in the RC, at each platform position there is an associated K-factor that is different from the other ones with large probability. In other words, the LOS component associated with a moving antenna can be regarded as a random variable. Due to this reason, an average K-factor is proposed [34],

$$K_{av} = \frac{\sum_{n=1}^{M_{pf}M_{ant}} |E_n[H]|^2}{\sum_{n=1}^{M_{pf}M_{ant}} \text{var}_n[H]} \quad (4.9)$$

where the subscript n in both E and var denotes an ensemble average over the subset (enumerated by n , i.e. the random channel associated with a fixed platform position and a fixed wall antenna) of the total sample set. Since the distribution of the LOS component is unknown, a good guess of it would be Gaussian. And under the Gaussian assumption, the

STD contribution from the random LOS components can be expressed as

$$\sigma_{LOS} = 1 / \sqrt{M_{LOS,ind}} \quad (4.10)$$

where $M_{LOS,ind}$ is the number of independent samples of the platform and wall antenna samples, which is given as

$$M_{LOS,ind} = M_{pf} M_{ant,ind} \quad (4.11)$$

where $M_{ant,ind}$ is the effectively independent wall antenna number for the LOS case. $M_{ant,ind} = M_{ant}$ when the wall antennas are separated by at least half-wavelength (e.g. in HP Bluetest RC); $M_{ant,ind} = 1$ when they are co-located (e.g. in RTS60 Bluetest RC that is shown in the next section).

By now, the uncertainty model has been presented. In the next section, this model will be verified by measurements in two Bluetest RCs.

4.3 Measurements and Results

In order to verify the uncertainty model presented in the previous section, extensive measurements in two chambers are performed. One chamber is the Bluetest HP RC that has been used mostly in this thesis; the other chamber is the Bluetest RTS60 RC that has been used for throughput measurement in Section 3.4. Basically, the RTS60 RC is an upgraded version of the HP RC (see Fig. 2.2). Need to say that the RTS60 is designed based on the knowledge that the K-factor degrades the measurement accuracy. As a result, the three wall antennas in the RTS60 RC are co-located (but with orthogonal polarizations) at one corner of the RC with a metallic shield blocking most of the LOS components. Moreover, two enlarged plate stirrers are equipped in the new RC (one moving horizontally along ceiling and the other one moving vertically along a wall).

Measurements are performed from 500 to 3000 MHz in both of the RCs separately by following the uncertainty assessment procedure (cf. Section 4.1). For the reference measurements, the measurement setup (or stirring sequence) of the HP RC is chosen such that: The turn-table platform was moved to 20 positions equally spaced by 18° , and for each platform position the two plates simultaneously moved to 50 positions (equally spanned on the total distances that they can move along the walls). At each stirrer position and for each wall antenna a full frequency sweep was performed by the VNA with a frequency step of 1 MHz, during which the channel transfer functions are sampled as a function of frequency and stirrer position. And the same procedure is repeated for three loading conditions. Such measurements take at least one week. In order to reduce the measurement time, the measurement setup in the RTS60 RC is almost the same except that the plate positions are limited to 25, and the frequency step is set to 2 MHz. Thus, measurements in the RTS60 RC have half of the (mechanical) stirring samples and approximately half of the frequency points of that of the HP RC, i.e. for each loading and reference antenna placement, the HP RC measurements result in 3000 samples at each of the 2501 frequency points, while the RTS60 RC measurements result in 1500 samples at each of the 1251 frequency points.

Fig. 4.2 shows the average K-factors (4.9) measured at both RCs, where load0, load1, and load2 correspond to empty, loading1, and loading2, respectively, as described in Section 2.1. The K-factor in the RTS60 RC is reduced significantly at low frequencies. Note that for better illustrations, a 20-MHz frequency smoothing is performed to the average K-factors before plotting.

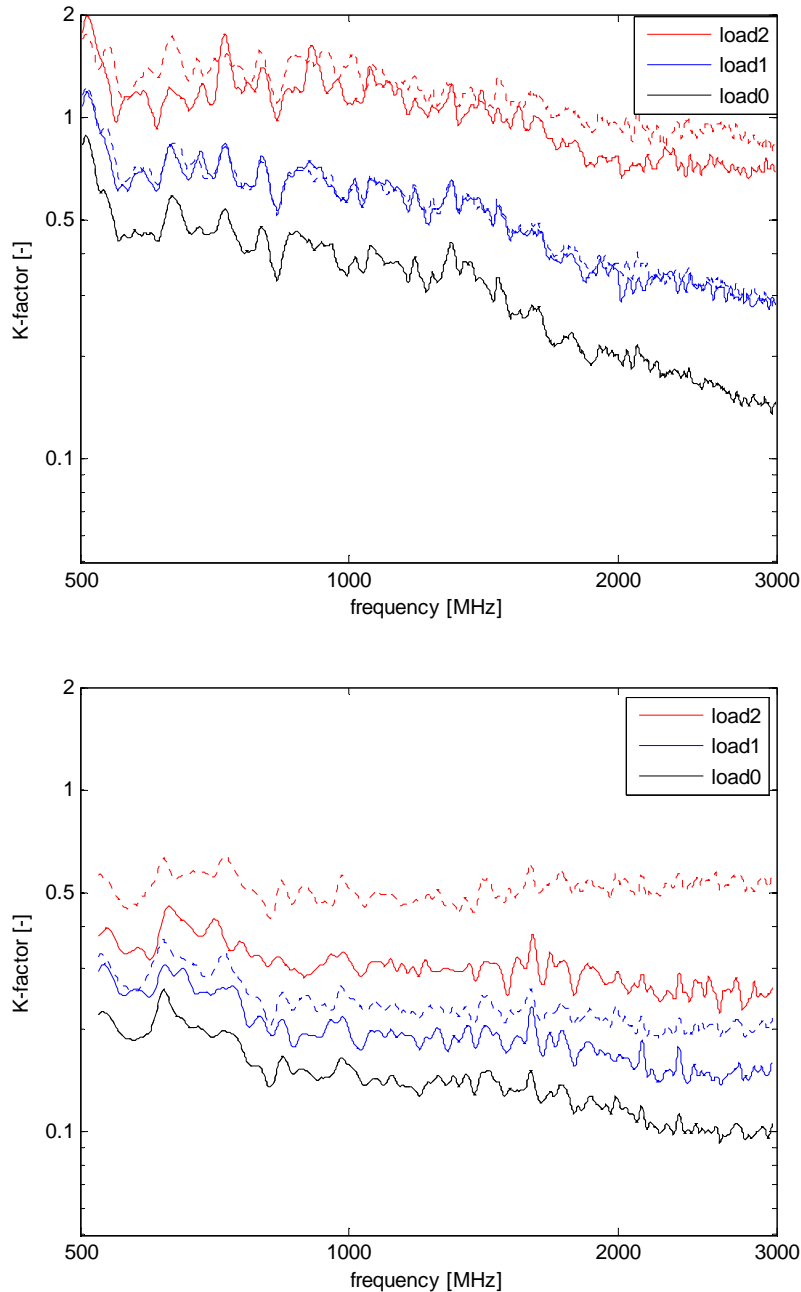
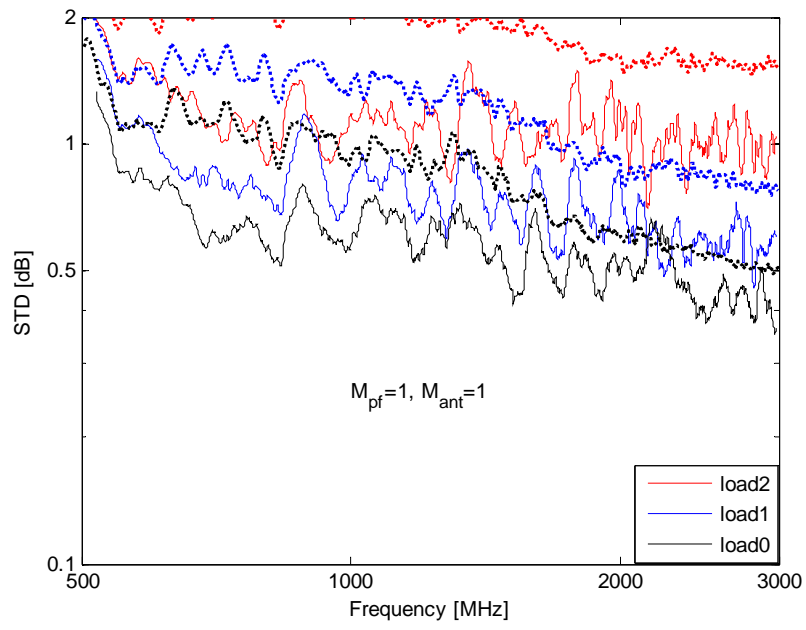
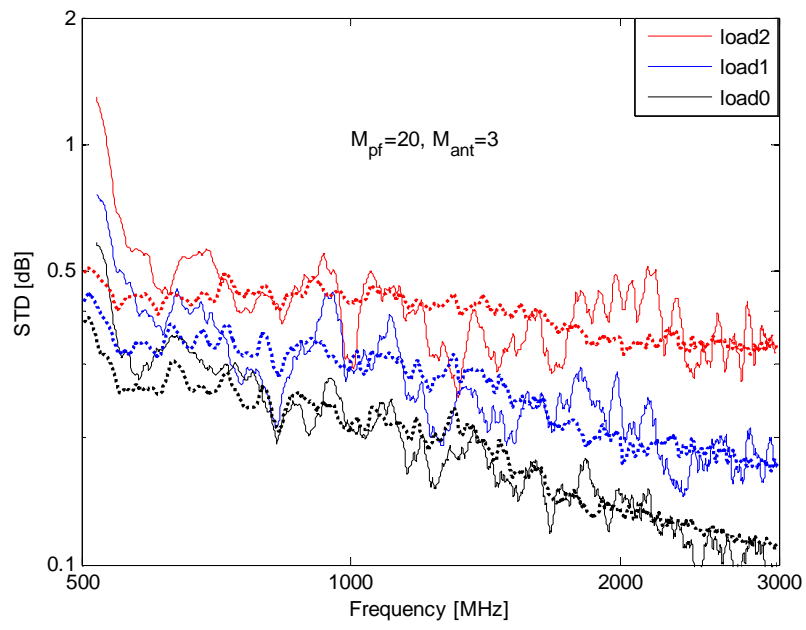


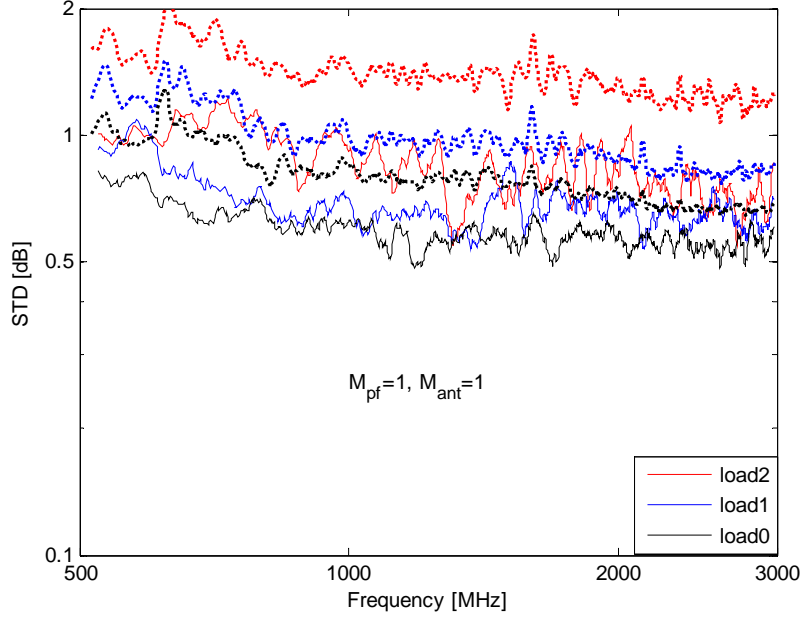
Figure 4.2: Measured average K-factors in Bluetest HP RC (upper) and RTS60 RC (lower). The solid curves are calculated directly from equation (4.9), whereas the dashed curves are calculated by using the average K-factor for the load0 case, and scaling it by the factors $\Delta f_{load1} / \Delta f_{load0}$ and $\Delta f_{load2} / \Delta f_{load0}$ for the load1 and load2 cases, respectively, by using their proportionality to average mode bandwidth [32], [35].



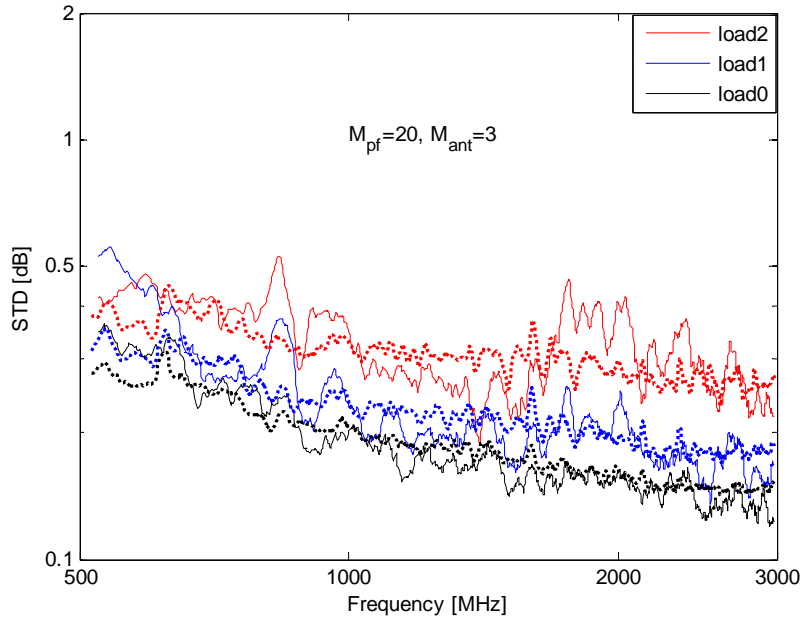
(a)



(b)



(c)

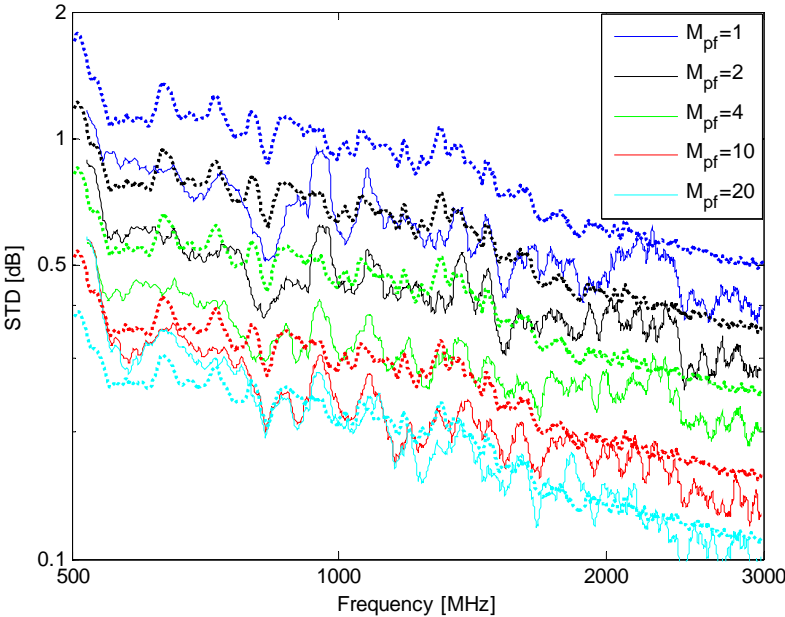


(d)

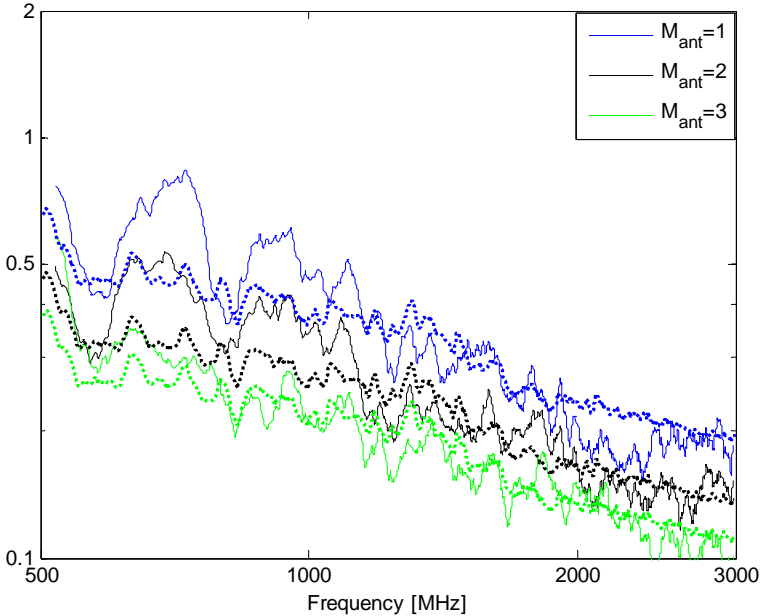
Figure 4.3: Comparison of measured (solid) and modeled (dotted) STDs of the Bluetest HP RC ((a) and (b)) and RTS60 RC ((c) and (d)).

Applying the uncertainty model (cf. Section. 4.2), the modeled STDs can be calculated and compared with the measured ones (see Fig. 4.3). Note that any subset of the total measured samples can be chosen for STD calculations at the post-processing stage. Here the subset of one platform position, one wall antenna, and all the plat positions is chosen (see Figs. 4.3 (a) and (c)), together with the total set of samples (see Figs. 4.3 (b) and (d)). Note that the RTS60 RC has only half of the samples of that of the HP RC in either case. Therefore, these plots are shown not for the sake of measurement accuracy comparisons, but for testing the uncertainty model. It can be seen from Fig. 4.3 that the uncertainty model can well predict the measured STD when $M_{LOS,ind}$ (4.11) is large, and that it overestimates the STD when $M_{LOS,ind} = 1$. This observation makes sense in that when $M_{LOS,ind}$ is small, (4.10) is not a good approximation of

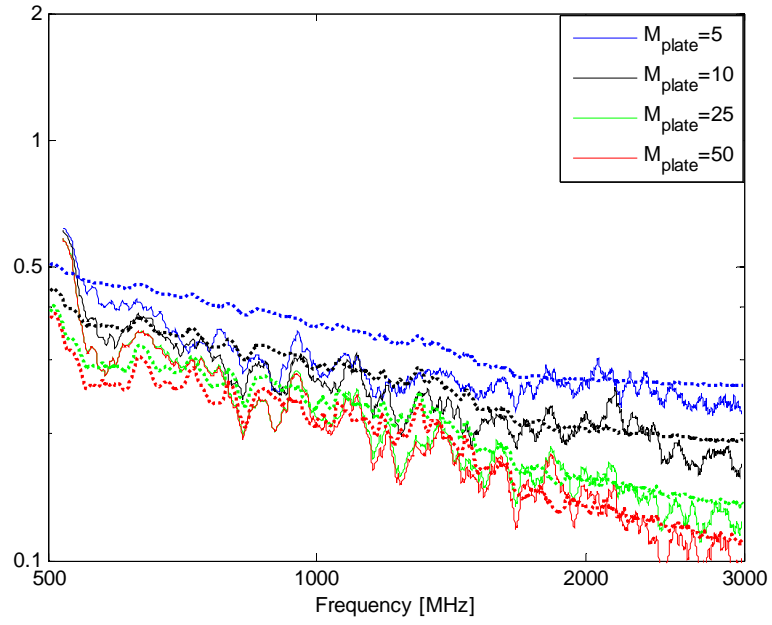
the STD contribution from the random LOS components, which results in mismatches in the prediction. Nevertheless, it is shown that with a sufficient $M_{LOS,ind}$ number, the uncertainty model approximates the true values with great accuracy.



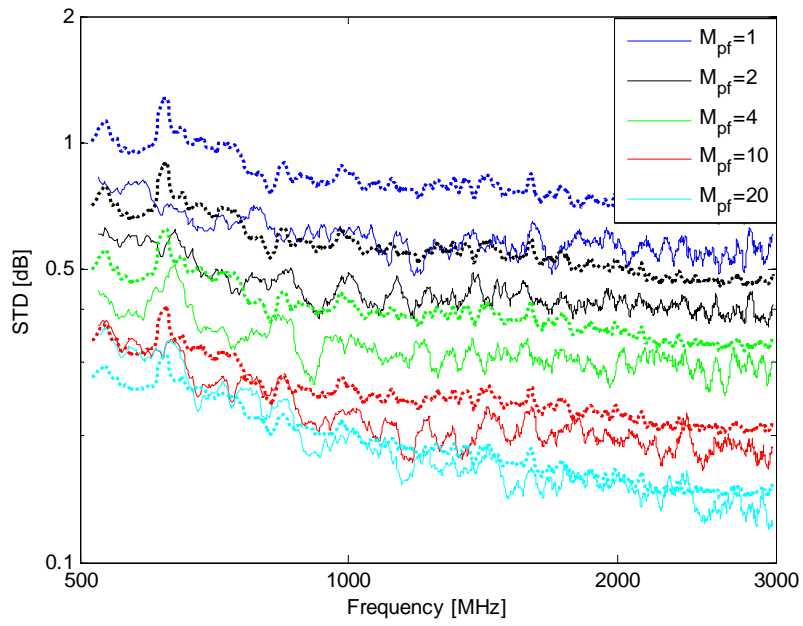
(a)



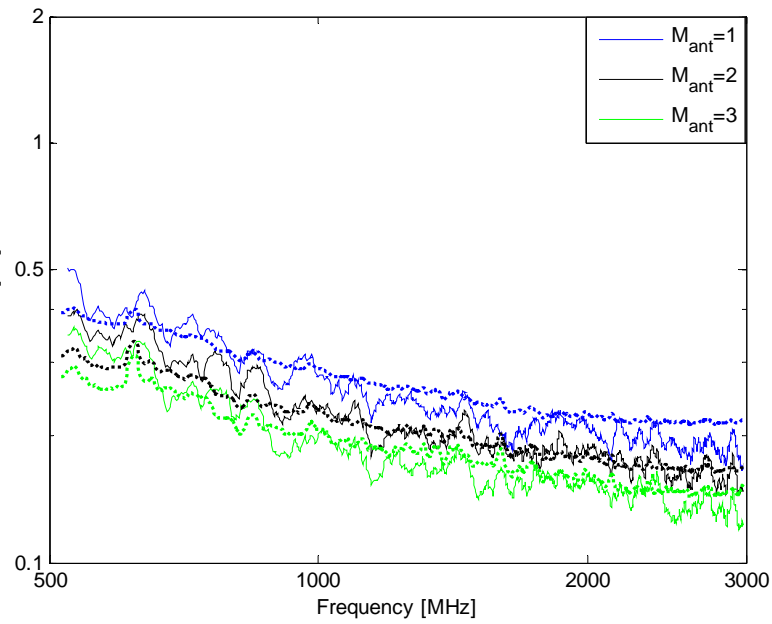
(b)



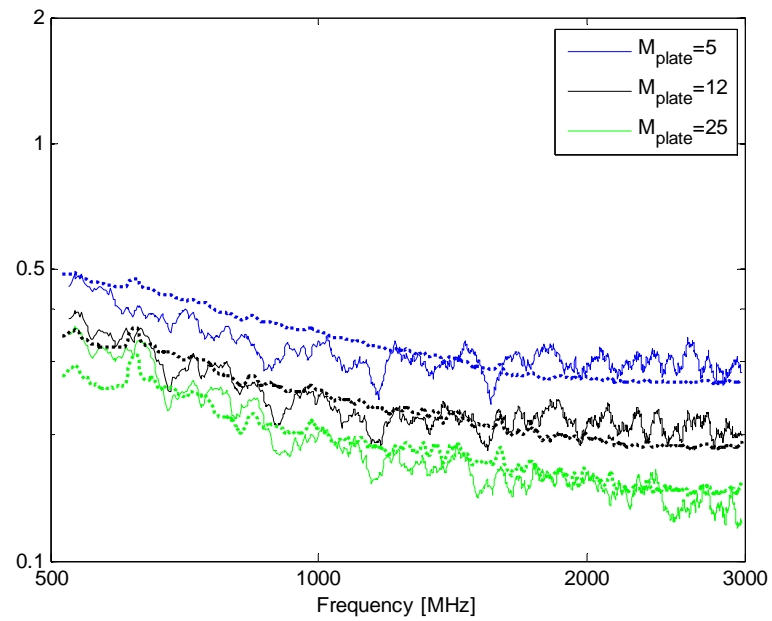
(c)



(d)

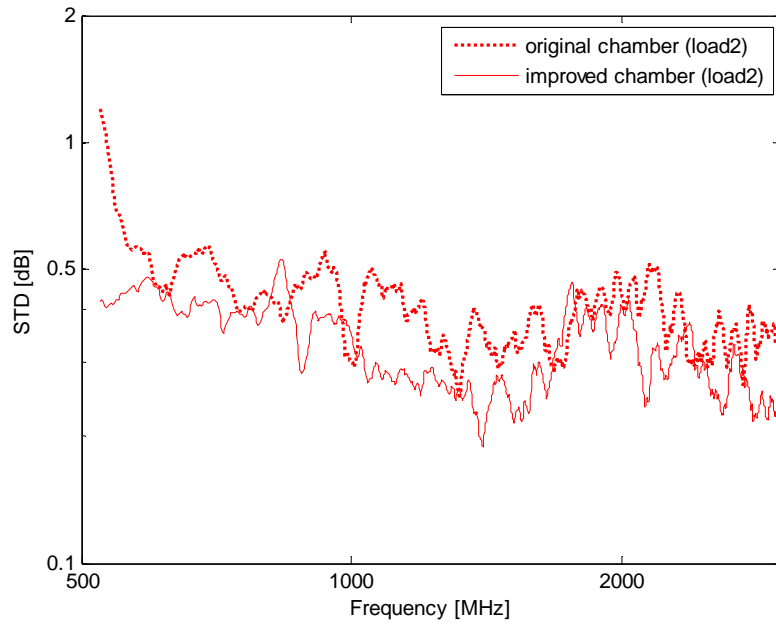


(e)

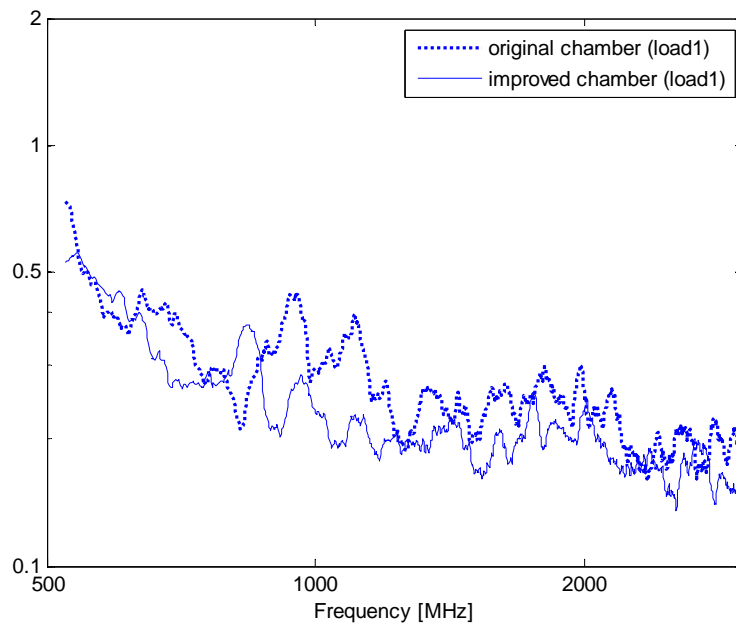


(f)

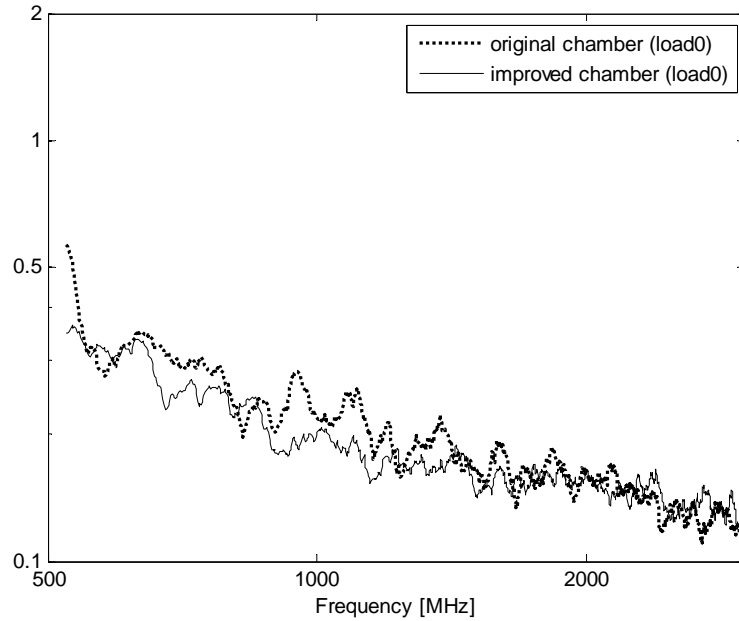
Figure 4.4: Comparison of measured (solid) and modeled (dotted) STDs of the Bluetest HP RC ((a)-(c)) and RTS60 RC ((d)-(f)). The plots show variation of STD with different number of platform positions ((a) and (d)), number of chamber antennas ((b) and (e)), and number of plate positions ((c) and (f)).



(a)



(b)



(c)

Figure 4.5: Uncertainty comparison of RTS60 (solid) and HP (dashed) RCs. Note that for fair comparison, the STDs are calculated using 3 wall antennas, 20 platform positions, and 25 plate positions for both chambers.

Fig. 4.4 shows how sensitive the STD is to decreasing the number of platform positions, wall antennas, and plate positions (with the first two being studied in [124] already). These curves were obtained from the measured samples by selecting every second, third or fourth of the collected samples. Good agreements are observed, in particular for the cases with many stirrer positions and for small loads. Note that for better illustrations, a 50-MHz frequency smoothing is performed to the STDs before plotting.

In order to compare the uncertainties of the two RCs, the plate position number of the HR RC measurements is reduced to 25 by selecting every other plate positions from its total data set. Fig. 4.5 shows the comparisons for all the three loads. The improvement of the improved RTS chamber is clearly observed especially for loaded RCs.

5. Conclusions

In this thesis, reverberation chambers are characterized for various OTA measurements, with MIMO terminal measurements as the main focus. A brief overview of this thesis is given in Chapter 1.

In Chapter 2, channel characterizations are performed in order to estimate the coherence bandwidth, the delay spread, and the Doppler spread [46]-[50] of the RC channel, for applications of active OTA measurements [21]-[24]. It is found that the coherence bandwidth and the average mode bandwidth are approximately the same [27] and that the RMS delay spread is proportional to the decay time in the RC. As the average mode bandwidth and the decay time in a RC can be easily calculated, they turn out to be computationally cheaper alternatives for channel characterizations, compared with the coherence bandwidth and the RMS delay spread, respectively. More importantly, it is found that the channel in a RC can be controlled (to be flat or frequency-selective fading depending on the bandwidth of the operating system) by simply loading the RC [27]. In addition, a method to estimate the Doppler spread using step-wise stationary stirring is presented [30]. With this method, one can predict the Doppler spread at any frequency within the sweeping frequency range based on a one-time measurement (as opposed to the traditional way of Doppler spread detection); and the Doppler spreads corresponding to different stirrer (and/or DUT) speeds can be obtained simply by a scaling factor. Using this method, one can readily determine the actual stirrer (and/or DUT) speed needed to emulate a certain fading channel (slow or fast fading again depending on the operating system bandwidth, or to be precise, the symbol duration) for active OTA tests.

In Chapter 3, it is shown that the RC can be used to measure the antenna radiation efficiency and the free-space reflection coefficient [65], as well as diversity gains and capacities of multi-antenna systems [13], [15]-[17]. It is shown that, with the frequency stirring technique [68], the free-space reflection coefficient of an antenna can be predicted in the RC with good accuracy [61]. In the thesis, two methods are presented for MRC diversity gain (i.e. the covariance-eigenvalue approach) and MIMO capacity (i.e. the embedded far-field function method) calculations. Although the covariance-eigenvalue approach is not a new method (it actually dates back to the 60s, e.g. [2]), its application in RC diversity measurements was recognized in [16] due to its fast convergence rate, as opposed to the traditional empirical CDF reading at 1% level [13]. Applying this method in RC diversity evaluations can either improve measurement accuracy (with the same amount of measured samples) or reduce measurement time (with reduced sample number) while keeping an acceptable accuracy. Moreover, the computational robustness of this method is studied in Section 3.2.1 (see also Appendix B). It is shown that, in spite of the apparent singularity, the method is robust for stochastic measurement-based evaluations. The embedded far-field function method (that is derived heuristically) is introduced mainly for the sake of capacity measurement comparison with that of the AC measurement [17]. Since one can measure the composite channel including overall antenna effect in the RC already, there seems no reason to extract the embedded radiation efficiencies and the correlation coefficients of the multi-port antenna from the measured channel samples in order to apply the embedded far-field method. Thus, this method is mainly for capacity evaluations based on AC measurements. Nevertheless, this method can be applied with slight modification (like the S-parameter method [89]) to test the validity of the assumed Kronecker channel model [90], [91] for a certain multi-antenna system.

Indeed the Kronecker assumption in the RC (for small MIMO-size) is verified to some extent in Section 3.3.3. In the literature, there is a popular method, i.e. the Z-parameter method, for MIMO capacity evaluations including the overall antenna effect. The popularity of the Z-parameter method [83]-[88] arises due to its convenience in analysis. Both methods are compared numerically using the example of parallel dipoles in Section 3.3.2, where excellent agreements are observed. Despite its analytical merit (w.r.t. analysis of antenna matching), the Z-parameter method is not suitable for measurement-based evaluations in that it necessitates the lossless antenna assumption (or antennas with ohmic losses that can be explicitly calibrated out, i.e. all the ohmic losses reside in the feeding cables of the antennas), which is unfortunately a strong assumption, since in practice most antennas have ohmic losses residing in the antenna itself which cannot be calibrated out. Therefore, the far-field function method is used for AC measurement-based capacity evaluations in this thesis. Besides the MRC diversity and MIMO capacity comparisons based on the RC and AC measurements, where good agreements are observed, it is also shown that correlations of a multi-port antenna can be estimated with acceptable accuracy in RC. Throughput measurements of an LTE dongle are also performed in this chapter. Moreover, the throughput model presented in [21] is given with an alternative information-theoretic interpretation [109], [110]. Simple as it is, the throughput model can take the complicated LTE system (in the case of point-to-point communications) into account (as opposed to the study of uncoded systems [114]), yielding excellent predictions of the measured results.

Chapter 4 is dedicated to characterizations of the RC measurement uncertainty [35], [117], [121], [124], because the measurement accuracy is of vital importance for both active and passive OTA measurements. In this chapter, first an uncertainty assessment procedure is proposed and applied later on for the STD calculations of the measured (normalized) power transfer functions. Then an uncertainty model [35] is presented. On contrast to the previous RC uncertainty studies, it is pointed out that the RC uncertainty is not only limited by the maximum number of independent samples, but also by the K-factor (that arises often because of the RC loading), and that the K-factor represents a residual error in a RC measurement. Based on these insights, a new RC (i.e. Bluetest RTS60) is designed to have a reduced K-factor. The uncertainty assessment measurements in the two RCs are performed and compared with the presented uncertainty model. It is shown that the model can predict the measured STD well provided that there are sufficient platform positions and independent wall antennas (w.r.t. LOS components) in the measurement setup.

Appendix A

Relation of Coherence Bandwidth and Delay Spread in RC

The received voltage at the receive antenna in a RC can be expressed as

$$V_r = c_r \sum_{m=1}^M \sum_{n=1}^N \vec{G}(\theta_m, \varphi_m) \cdot \vec{E}_{mn} \quad (\text{A.1})$$

where $\vec{E}_{mn} = E_{mn} \exp\{\varphi_{mn}\}$, with $\varphi_{mn} = j(\beta t(\vec{v} \cdot \hat{r}) - \omega \tau_{mn})$, is the complex amplitude of each plane wave at the origin of the chosen coordinate system of the complex far-field function $\vec{G}(\theta_m, \varphi_m)$ of the antenna, c_r is a constant, $\hat{r} = \sin \theta_m (\cos \varphi_m \hat{x} + \sin \varphi_m \hat{y}) + \cos \theta_m \hat{z}$ is the angle of arrival (AoA) of the wave from m th direction, and φ_{mn} is the phase of the incoming plane wave from m th direction at n th delay time. The phase φ_{mn} is assumed to vary with the velocity vector \vec{v} of the moving receive antenna, and τ_{mn} denotes the n th delay time of the wave from m th direction, with $\omega = 2\pi f$.

Equation (A.1), can be separated into real and imaginary parts as

$$V_r = X + jY. \quad (\text{A.2})$$

Assume two signals at different angular frequencies and delays, and let their amplitudes be denoted respectively as

$$\begin{aligned} r_1 &= |V_r(\omega_1, t)| = \sqrt{X_1^2 + Y_1^2}, \\ r_2 &= |V_r(\omega_2, t + \Delta t)| = \sqrt{X_2^2 + Y_2^2}. \end{aligned} \quad (\text{A.3})$$

The envelope correlation function can be expressed as

$$\begin{aligned} \rho_e &= \frac{R_e - E[r_1]E[r_2]}{\sqrt{\{E[r_1^2] - (E[r_1])^2\}\{E[r_2^2] - (E[r_2])^2\}}}, \\ R_e &= \int_0^\infty \int_0^\infty \int_0^{4\pi} \int_0^{4\pi} r_1 r_2 p(\Omega_1, \Omega_2, r_1, r_2) d\Omega_1 d\Omega_2 dr_1 dr_2 \end{aligned} \quad (\text{A.4})$$

where $p(\Omega_1, \Omega_2, r_1, r_2)$ is the joint probability distribution. While (A.4) is difficult to solve, a good approximation of it is given by [47],

$$\rho_e = \frac{(E[X_1 X_2])^2 + (E[X_1 Y_2])^2}{(E[X_1^2])^2} \quad (\text{A.5})$$

with

$$E[X_1^2] = \int_0^\infty \int_0^{4\pi} E_{\text{mn}}^2 \cos^2[\beta v t \cos(\varphi) \sin(\theta) - \omega \Delta t] d\Omega d\tau = \frac{E_0^2}{2} \int_0^\infty \int_0^{4\pi} p(\theta, \varphi) p(\tau) d\Omega d\tau = \frac{E_0^2}{2}. \quad (\text{A.6})$$

Here it is assumed that the receive antenna is moving in x-direction with scalar speed v . Since X_1 (in the RC) is zero mean Gaussian distributed [12], (A.6) is its variance, which for notational simplicity is denoted as σ^2 .

$$\begin{aligned} E[X_1 X_2] &= \sigma^2 \int_0^\infty \int_0^{4\pi} \cos[\beta v \Delta t \cos(\varphi) \sin(\theta) - \Delta \omega \Delta t] p(\theta, \varphi) p(\tau) d\Omega d\tau \\ &= \sigma^2 \int_0^\infty \int_0^{2\pi} \int_0^\pi \cos[\beta v \Delta t \cos(\varphi) \sin(\theta)] \frac{1}{4\pi} \sin\theta d\theta d\varphi \cos(\Delta \omega \Delta t) \frac{1}{\sigma_\tau} \exp(-\frac{\tau}{\sigma_\tau}) d\tau \\ &= \sigma^2 \frac{\sin(\beta v \Delta t) / (\beta v \Delta t)}{1 + (\Delta \omega)^2 \sigma_\tau^2} \end{aligned} \quad (\text{A.7})$$

where $\Delta \omega = \omega_2 - \omega_1$.

$$\begin{aligned} E[X_1 Y_2] &= \sigma^2 \int_0^\infty \int_0^{4\pi} \sin[\beta v \Delta t \cos(\varphi) \sin(\theta) - \Delta \omega \Delta t] p(\theta, \varphi) p(\tau) d\Omega d\tau \\ &= \sigma^2 \Delta \omega \sigma_\tau \frac{\sin(\beta v \Delta t) / (\beta v \Delta t)}{1 + (\Delta \omega)^2 \sigma_\tau^2}. \end{aligned} \quad (\text{A.8})$$

The term $\sin(\beta d) / (\beta d)$ is the spherical correlation function over the space of a RC [25]. Similarly,

$$\begin{aligned} E[X_1^2] &= E[Y_1^2] = E[X_2^2] = E[Y_2^2] = \sigma^2, \\ E[X_1 X_2] &= E[Y_1 Y_2], \quad E[X_1 Y_2] = -E[X_2 Y_1]. \end{aligned} \quad (\text{A.9})$$

Substituting (A.6)-(A.9) into (A.5),

$$\rho_e = \frac{[\sin(\beta v \Delta t) / (\beta v \Delta t)]^2}{1 + (\Delta \omega)^2 \sigma_\tau^2}. \quad (\text{A.10})$$

In order to observe the relation between $\Delta \omega = 2\pi \Delta f$ and σ_τ , delay Δt is set to zero,

$$\rho_e = \frac{1}{1 + (\Delta \omega)^2 \sigma_\tau^2} \quad (\text{A.11})$$

$\Delta\omega$ and σ_τ determine the envelope correlation value. Thus the 50% coherence bandwidth based on envelop correlation is

$$B_{ce,50\%} = \frac{1}{2\pi\sigma_\tau} \quad (\text{A.12})$$

with $\frac{1}{1+(2\pi B_{ce,50\%})^2\sigma_\tau^2} = \frac{1}{2}$.

The signal correlation function is

$$\begin{aligned} \rho &= \frac{E[(X_1 + jY_1)(X_2 + jY_2)^*]}{(E[X_1^2] + E[Y_1^2])} \\ &= \frac{E[X_1X_2] + E[Y_1Y_2] - j(E[X_1Y_2] - E[X_2Y_1])}{(E[X_1^2] + E[Y_1^2])}. \end{aligned} \quad (\text{A.13})$$

Similarly, the signal correlation function can be expressed as

$$\rho = \frac{\sin(\beta v \Delta t)}{\beta v \Delta t} \frac{1 - j\Delta\omega\sigma_\tau}{1 + (\Delta\omega)^2\sigma_\tau^2}. \quad (\text{A.14})$$

The magnitude of the signal correlation function (when τ is set to zero) is

$$|\rho| = \frac{1}{\sqrt{1 + (\Delta\omega)^2\sigma_\tau^2}}. \quad (\text{A.15})$$

Comparing (A.11) and (A.15), it is shown that the envelop correlation function equals the square of the magnitude of signal correlation function,

$$\rho_e = |\rho|^2. \quad (\text{A.16})$$

With a threshold of $1/\sqrt{2}$ (≈ 0.7), (A.15) reduces to

$$B_{cs,70\%} = \frac{1}{2\pi\sigma_\tau}. \quad (\text{A.17})$$

The 50% coherence bandwidth based on magnitude of signal correlation function is

$$B_{cs,50\%} = \frac{\sqrt{3}}{2\pi\sigma_\tau}. \quad (\text{A.18})$$

A general formula relating coherence bandwidth to different correlation thresholds is

$$B_c = \frac{1}{2\pi\sigma_\tau} \sqrt{\frac{1-|\rho|^2}{|\rho|^2}}. \quad (\text{A.19})$$

Appendix B

Rectangular Doppler Spectrum

In an ideal isotropic-scattering RC, assume that the receive antenna travels along x-axis with a constant speed. The complex envelope of the receive signal can then be modeled as a summation of scattered signals from all directions:

$$V(t) = \sum_{m=1}^N A_m \exp\{j[\beta v t \cos \theta_m \sin \theta_m - \omega \tau_m]\} \quad (\text{B.1})$$

where β is the wave number, (θ_m, φ_m) , τ_m , and A_m are the AoA, delay time, and signal amplitude from the m th path, respectively. With WSS assumption, the time ACF of the received signal is:

$$R(\Delta t) = E[V(t)V^*(t + \Delta t)] / E[|V(t)|^2]. \quad (\text{B.2})$$

Denote the PDF of elevation angle as $p_\Theta(\theta)$, (B.2) can be expressed as

$$R(\Delta t) = \int_{-\infty}^{\infty} J_0(\beta v \Delta t \sin \theta) p_\Theta(\theta) d\theta \quad (\text{B.3})$$

where $J_0(\cdot)$ is the Bessel function of the first kind of the 0th order. The Doppler spectrum is [46]

$$S_d(f_d) = \frac{1}{\pi f_{d,\max}} \int_{-\infty}^{\infty} \frac{p_\Theta(\theta)}{\sqrt{\sin^2 \theta - (f_d / f_{d,\max})^2}} d\theta \quad (\text{B.4})$$

where the maximum Doppler frequency shift $f_{d,\max} = v / \lambda = \beta v / 2\pi$, and $|f_d| < f_{d,\max}$, and the Doppler frequency is

$$f_d = f_{d,\max} \cos \phi \sin \theta. \quad (\text{B.5})$$

The conditional CDF of the f_d provided that θ is known can be expressed as

$$\begin{aligned} F(f_d | \Theta = \theta) &= P(F_d \leq f_d | \Theta = \theta) \\ &= P(F_d \leq f_{d,\max} \cos \Phi \sin \Theta | \Theta = \theta) \\ &= P(\cos \Phi \geq \frac{F_d}{f_{d,\max} \sin \Theta} | \Theta = \theta) \\ &= \int_{-\infty}^{\arccos[f_d / (f_{d,\max} \sin \theta)] + \pi} p_\Phi(\phi) d\phi - \int_{-\infty}^{\arccos[f_d / (f_{d,\max} \sin \theta)]} p_\Phi(\phi) d\phi \end{aligned} \quad (\text{B.6})$$

where $p_\phi(\phi)$ is the PDF of azimuth angle, $\text{acos}(\cdot)$ is inverse cosine function. The conditional PDF of f_d is the derivative of (B.6),

$$\begin{aligned} p(f_d | \theta) &= \frac{2}{f_{d,\max}} \frac{p_\phi(\phi)}{\sqrt{\sin^2 \theta - (f_d / f_{d,\max})^2}} \\ &= \frac{1}{\pi f_{d,\max}} \frac{1}{\sqrt{\sin^2 \theta - (f_d / f_{d,\max})^2}}. \end{aligned} \quad (\text{B.7})$$

The PDF of f_d is

$$\begin{aligned} p(f_d) &= \int_{-\infty}^{\infty} p(f_d | \theta) p_\Theta(\theta) d\theta \\ &= \frac{1}{\pi f_{d,\max}} \int_{-\infty}^{\infty} \frac{p_\Theta(\theta)}{\sqrt{\sin^2 \theta - (f_d / f_{d,\max})^2}} d\theta \end{aligned} \quad (\text{B.8})$$

where $|f_d| < f_{d,\max}$. Comparing (B.4) and (B.8), it is shown that the normalized Doppler spectrum is the same with Doppler frequency PDF, which makes sense, since in the fading channel a higher power in a certain Doppler frequency implies a larger likelihood of that Doppler frequency.

The well-known Jake's Model [46] assumes all AoAs are in the azimuth plane. Substituting $\theta = \pi/2$ and $p_\Theta(\theta = \pi/2) = 1$ into (B.8),

$$p(f_d) = \frac{1}{\pi f_{d,\max}} \frac{1}{\sqrt{1 - (f_d / f_{d,\max})^2}}, \quad |f_d| < f_{d,\max} \quad (\text{B.9})$$

which is identical to the power spectrum density (PSD) of the Jake's Model.

In an ideal RC, i.e. a 3-D isotropic scattering environment where no particular direction is preferred, one can assume that the receive antenna travels along z-axis for simplicity, in which case $f_d = f_{d,\max} \cos \theta$. The CDF and PDF of f_d are respectively

$$F(f_d) = P[\Theta = \theta \geq \text{acos}(f / f_{d,\max})] \quad (\text{B.10})$$

$$p(f_d) = \frac{1}{f_{d,\max}} \frac{p_\Theta[\text{acos}(f_d / f_{d,\max})]}{\sqrt{1 - (f_d / f_{d,\max})^2}} = \frac{1}{2 f_{d,\max}}, \quad |f_d| < f_{d,\max} \quad (\text{B.11})$$

where $p_\Theta(\theta) = \sin \theta / 2$ for isotropic environment. Substituting $p_\Theta(\theta) = \sin \theta / 2$ into (B.3), the autocorrelation function becomes

$$R(\Delta t) = \frac{\sin(\beta v \Delta t)}{\beta v \Delta t} \quad (\text{B.12})$$

The Doppler spectrum, i.e. the Fourier transform of (B.12), is

$$S_d(f_d) = \frac{1}{2 f_{d,\max}}, \quad |f_d| < f_{d,\max} \quad (\text{B.13})$$

Appendix C

Proof of Convergence in Distribution of EDG Obtained Using Covariance-Eigenvalue Approach

To prove the convergence in distribution of EDG obtained using the covariance-eigenvalue approach is equivalent to show that Lee's formula converges to the true CDF when eigenvalues approach to each other.

First we consider the case when $N = 2$, and $\lambda_i \rightarrow \lambda$ ($i = 1, 2$). In this case, Lee's formula reduces to

$$F_{Lee}(\gamma) = 1 - \frac{\lambda_1 \exp(-\gamma/\lambda_1) - \lambda_2 \exp(-\gamma/\lambda_2)}{\lambda_1 - \lambda_2}. \quad (\text{C.1})$$

The true CDF, i.e. the distribution of the MRC output of a two-port antenna with 100% embedded radiation efficiencies and no correlation is

$$F(\gamma) = 1 - \exp\left(-\frac{\gamma}{\lambda}\right) \left(1 + \frac{\gamma}{\lambda}\right). \quad (\text{C.2})$$

Namely, we need to show that $F_{Lee}(\gamma) \rightarrow F(\gamma)$ as $\lambda_i \rightarrow \lambda$.

Proof: Without loss of generality, let $\lambda_2 = \lambda$ and $\lambda_1 = \lambda + \varepsilon$ for any $\varepsilon > 0$ ($\lambda_i \rightarrow \lambda$ is equivalent to $\varepsilon \rightarrow 0$), and substitute these into (C.1),

$$F_{Lee}(\gamma) = 1 - \frac{\lambda}{\varepsilon} \left[\exp\left(-\frac{\gamma}{\lambda + \varepsilon}\right) - \exp\left(-\frac{\gamma}{\lambda}\right) \right] - \exp\left(-\frac{\gamma}{\lambda + \varepsilon}\right). \quad (\text{C.3})$$

Denote $f(\lambda + \varepsilon) = \exp\left(-\frac{\gamma}{\lambda + \varepsilon}\right)$, using the Taylor expansion to the first order,

$$f(\lambda + \varepsilon) = f(\lambda) + \frac{\gamma}{\lambda^2} \exp\left(-\frac{\gamma}{\lambda}\right) \varepsilon + o(\varepsilon) \quad (\text{C.4})$$

where $o(\varepsilon) \rightarrow 0$ as $\varepsilon \rightarrow 0$. Substitute (C.4) into (C.3),

$$\begin{aligned} \lim_{\varepsilon \rightarrow 0} F_{Lee}(\gamma) &= \lim_{\varepsilon \rightarrow 0} \left\{ 1 - \frac{\lambda}{\varepsilon} \left[\frac{\gamma}{\lambda^2} \exp\left(-\frac{\gamma}{\lambda}\right) \varepsilon + o(\varepsilon) \right] - \left[\exp\left(-\frac{\gamma}{\lambda}\right) + \frac{\gamma}{\lambda^2} \exp\left(-\frac{\gamma}{\lambda}\right) \varepsilon + o(\varepsilon) \right] \right\} \\ &= 1 - \frac{\gamma}{\lambda} \exp\left(-\frac{\gamma}{\lambda}\right) - \exp\left(-\frac{\gamma}{\lambda}\right) = F(\gamma). \end{aligned} \quad (\text{C.5})$$

□

It is, however, difficult to prove that Lee's formula converges to the true CDF with arbitrary antenna element number (and therefore arbitrary number of equal eigenvalues) from CDF formula directly. This thesis resorts to characteristic function for a more general proof.

It is self-evident from (3.7) that $\phi(z)$ converges as $\lambda_i \rightarrow \lambda$. Since $\phi(z)$ is the Fourier transform of the PDF of γ , to show that the limit of Lee's formula converges to the true CDF is equivalent to show the convergence of $\phi(z)$.

Proof: Let F_i ($i = 1 \dots N$) be the CDF of γ when i eigenvalues of the covariance matrix of the diversity antenna are equal. Namely, F_1 denotes Lee's formula, and F_N represents the classical MRC output CDF with i.i.d. antenna branches. Due to bijection between CDF and characteristic function, there exists one $\phi_i(z)$ for each F_i uniquely. The Levy's continuity theorem [74] states that if $\phi_1(z)$ converges to $\phi_i(z)$, then F_1 converges to F_i .

□

This is an immediate but general proof, yet it is rather abstract, for this reason, the proof for $N = 2$ case is kept for the sake of better convergence illustration.

Appendix D

Derivation of Z-Parameter Method

A MIMO system can be expressed as [88]

$$\begin{bmatrix} \mathbf{v}_T \\ \mathbf{v}_R \end{bmatrix} = \begin{bmatrix} \mathbf{Z}_T & \mathbf{0} \\ \mathbf{H}^{oc} & \mathbf{Z}_R \end{bmatrix} \begin{bmatrix} \mathbf{i}_T \\ \mathbf{i}_R \end{bmatrix} \quad (\text{D.1})$$

where \mathbf{Z}_T , \mathbf{i}_T , and \mathbf{v}_T are impedance matrix, current and voltage vectors at the transmitter, respectively; and \mathbf{Z}_R , \mathbf{i}_R and \mathbf{v}_R are impedance matrix, current and voltage vectors at the receiver, respectively; $\mathbf{0}$ is zero matrix with proper dimensions, \mathbf{H}^{oc} is channel matrix corresponding to open-circuited antennas at both MIMO sides. Note that for notation simplicity and without loss of generality, the additive noises is omitted for the time being, while the noises can be easily included using similar SNR concept as the one used in Section 3.2.1. The following derivation follows the main line of [83] (some typos therein are corrected). Based on simple circuit theory, the transmit and receive voltage vectors can be expressed respectively as

$$\begin{aligned} \mathbf{v}_T &= \mathbf{Z}_T(\mathbf{Z}_T + \mathbf{Z}_s)^{-1} \mathbf{v}_s \\ \mathbf{v}_R &= -\mathbf{Z}_L \mathbf{i}_R \end{aligned} \quad (\text{D.2})$$

where \mathbf{v}_s is source voltage vector, \mathbf{Z}_s and \mathbf{Z}_L are source and load impedance matrices, respectively. For coupled impedance matching, both \mathbf{Z}_s and \mathbf{Z}_L are full matrices, whereas for uncoupled impedance matching, \mathbf{Z}_s and \mathbf{Z}_L are diagonal matrices. \mathbf{v}_R is related to \mathbf{v}_T as

$$\mathbf{v}_R = \mathbf{Z}_L(\mathbf{Z}_L + \mathbf{Z}_R)^{-1} \mathbf{H}^{oc}(\mathbf{Z}_T + \mathbf{Z}_s)^{-1} \mathbf{v}_s. \quad (\text{D.3})$$

The factor $\mathbf{Z}_L(\mathbf{Z}_L + \mathbf{Z}_R)^{-1} \mathbf{H}^{oc}(\mathbf{Z}_T + \mathbf{Z}_s)^{-1}$ is voltage transfer function. To relate the Z-parameter model (D.3) to the information-theoretic input-output relation, $\mathbf{y} = \mathbf{H}_{eff} \mathbf{x}$, the voltage transfer function has to be properly normalized such that the received power satisfies

$$E\{tr[\text{Re}(\mathbf{Z}_L \mathbf{i}_R \mathbf{i}_R^H)]\} = E[tr(\mathbf{y} \mathbf{y}^H)] = E[tr(\mathbf{H}_{eff} \mathbf{K}_x \mathbf{H}_{eff}^H)] \quad (\text{D.4})$$

where $\mathbf{K}_x = \mathbf{I}_{N_t} P_T / N_t$ is covariance matrix of transmit signals. The total radiated power is $P_T = E\{tr[\text{Re}(\mathbf{Z}_T \mathbf{i}_T \mathbf{i}_T^H)]\}$. Using simple algebra, and denoting $\mathbf{R}_L = \text{Re}\{\mathbf{Z}_L\}$ and $\mathbf{R}_T = \text{Re}\{\mathbf{Z}_T\}$, the effective channel can be written as

$$\mathbf{H}_{eff} = \sqrt{N_t} \mathbf{R}_L^{1/2} (\mathbf{Z}_L + \mathbf{Z}_R)^{-1} \mathbf{H}^{oc} \mathbf{R}_T^{-1/2}. \quad (\text{D.5})$$

Accordingly, the effective channel should be normalized to the average channel gain of a

SISO system with antennas at both side conjugate matched, i.e. $z_L = z_R^*$ and $z_s = z_T^*$ where superscript * is conjugate operator, z_T and z_R are antenna transmit and receive impedance respectively, and z_L and z_s are load and source impedances at transmit and receive sides, respectively. It is easy to derive the effective SISO channel, i.e. h_{eff} , as

$$h_{eff} = \sqrt{\frac{N_t}{r_R r_T}} \frac{h}{2} \quad (\text{D.6})$$

where $r_T = \text{Re}\{z_T\}$, $r_R = \text{Re}\{z_R\}$ and $E[|h|^2] = 1$. Dividing \mathbf{H}_{eff} with $\sqrt{E[|h_{eff}|^2]}$, the normalized MIMO channel that includes overall antenna effect is

$$\mathbf{H} = 2\sqrt{r_R r_T} \mathbf{R}_L^{1/2} (\mathbf{Z}_L + \mathbf{Z}_R)^{-1} \mathbf{H}^{oc} \mathbf{R}_T^{-1/2} \quad (\text{D.7})$$

where $\mathbf{H}^{oc} = \mathbf{\Phi}_R^{oc,1/2} \mathbf{H}_w \mathbf{\Phi}_T^{oc,1/2}$, with $\mathbf{\Phi}_R^{oc}$ and $\mathbf{\Phi}_T^{oc}$ denoting the open-circuit correlation matrix.

References

- [1] R. G. Vaughan and J. B. Andersen, "Antenna diversity in mobile communications," *IEEE Trans. Veh. Technol.* vol. 36, no. 4, pp. 149-172, Nov. 1987.
- [2] J. N. Pierce and S. Stein, "Multiple diversity with nonindependent fading," *Proc. IRE*, pp. 89-104, 1960.
- [3] C. J. Foschini, "Layered space-time architecture for wireless communication in a fading environment when using multi-element antennas," *Bell Labs Tech. Journal*, vol. 1, pp. 41-59, 1996.
- [4] G. J. Foschini and M. J. Gans, "On limits of wireless communications in a fading environment when using multiple antennas," *Wireless Personal Communications*, vol. 6, no. 3, pp. 311-335, Mar. 1998.
- [5] I. E. Telatar, "Capacity of multi-antenna Gaussian channels," *Europ. Trans. Telecommun.*, vol. 10, no. 6, pp. 585-596, Nov. 1999.
- [6] A. Paulraj, R. Nabar and D. Gore, *Introduction to Space-time Wireless Communication*, Cambridge University Press, 2003.
- [7] O. Norklit, P. D. Teal, and R. G. Vaughan, "Measurement and evaluation of multi-antenna handsets in indoor mobile communication," *IEEE Trans. Antennas Propagat.*, vol. 49, no. 3, pp. 429-437, Mar. 2001.
- [8] K. Yu, M. Bengtsson, B. Ottersten, D. McNamara, P. Karlsson, and M. Beach, "Modeling of wide-band MIMO radio channels based on NLoS indoor measurements," *IEEE Trans. Veh. Technol.* vol. 53, no. 3, pp. 655-665, May 2004.
- [9] D. Chizhik, J. Ling, P. W. Wolniansky, R. A. Valenzuela, N. Costa, and K. Huber, "Multiple-input-multiple-output measurements and modeling in Manhattan," *IEEE J. Sel. Areas Commun.*, vol. 21, no. 3, pp. 321-330, Apr. 2003.
- [10] J. P. Kermoal, L. Schumacher, K. I. Pedersen, P. E. Mogensen, and F. Frederiksen, "A stochastic MIMO radio channel model with experimental validation," *IEEE J. Sel. Areas Commun.*, vol. 20, pp. 1211-1226, Aug. 2002.
- [11] H. Ozelik, M. Herdin, W. Weichselberger, J. Wallace, and E. Bonek, "Deficiencies of 'Kronecker' MIMO radio channel model," *Electron. lett.*, vol. 39, no. 16, pp. 1209-1210, Aug. 2003.
- [12] J. G. Kostas and B. Boverie, "Statistical model for a mode-stirred chamber," *IEEE Trans. Electromagn. Compat.*, vol. 33, no. 4, pp. 366-370, Nov. 1991.
- [13] K. Rosengren and P.-S. Kildal, "Radiation efficiency, correlation, diversity gain and capacity of a six-monopole antenna array for a MIMO system: theory, simulation and measurement in reverberation chamber," *IEE Proc. Microw. Antennas Propag.* vol. 152, pp. 7-16, 2005. See also Erratum published in August 2006.
- [14] K. Rosengren, *Characterization of Terminal Antennas for Diversity and MIMO Systems by Theory, Simulations and Measurements in Reverberation Chamber*, PhD thesis, Chalmers University of Technology, 2005.
- [15] P.-S. Kildal and K. Rosengren, "Correlation and capacity of MIMO systems and mutual coupling, radiation efficiency and diversity gain of their antennas: Simulations and measurements in reverberation chamber," *IEEE Commun. Mag.*, vol. 42, no. 12, pp. 102-112, Dec. 2004.
- [16] X. Chen, P.-S. Kildal, and J. Carlsson, "Fast converging measurement of MRC diversity gain in reverberation chamber using covariance-eigenvalue approach," *IEICE Trans. Electron.*, vol. E94-C, no.10, pp.1657-1660, Oct. 2011.

- [17] X. Chen, P.-S. Kildal, J. Carlsson, and J. Yang, "Comparison of ergodic capacities from wideband MIMO antenna measurements in reverberation chamber and anechoic chamber," *IEEE Antennas Wireless Propag. Lett.*, vol. 10, pp. 446-449, 2011.
- [18] X. Chen, P.-S. Kildal, J. Carlsson, and J. Yang, "MRC diversity and MIMO capacity evaluations of multi-port antennas using reverberation chamber and anechoic chamber," submitted to *IEEE Trans. Antennas Propag.*, April, 2012.
- [19] O. Delangre, P. D. Doncker, M. Lienard, and P. Degauque, "Coupled reverberation chamber for emulating MIMO channels," *C. R. Physique* 11, pp. 30-36, 2010.
- [20] L. Garcia-Garcia, B. Lindmark, N. Jalden, and C. Orlenius, "MIMO capacity of antenna arrays evaluated using radio channel measurements, reverberation chamber and radiation patterns," *IET Microw. Antennas Propag.*, vol. 1, pp. 1160-1169, 2007.
- [21] P.-S. Kildal, A. Hussain, X. Chen, C. Orlenius, A. Skårbratt, J. Asberg, T. Svensson, and T. Eriksson, "Threshold receiver model for throughput of wireless devices with MIMO and frequency diversity measured in reverberation chamber," *IEEE Antennas Wireless Propag. Lett.*, vol. 10, pp. 1201-1204, 2011.
- [22] P.-S. Kildal, C. Orlenius, and J. Carlsson, "OTA testing in multipath of antennas and wireless devices with MIMO and OFDM," accepted for publication in special issue of *Proceedings of the IEEE*, 2012.
- [23] G. Ferrara, M. Migliaccio, and A. Sorrentino, "Characterization of GSM non-line-of-sight propagation channels generated in a reverberating chamber by using bit error rates," *IEEE Trans. Electromagn. Compat.*, vol. 49, no. 3, pp. 467-473, Aug. 2007.
- [24] K. A. Remley, H. Fielitz, C.L. Holloway, Q. Zhang, Q. Wu, and D. W. Matolak, "Simulation of a MIMO system in a reverberation chamber," In *Proc. IEEE EMC Symp.* Aug. 2011.
- [25] D. A. Hill, "Linear dipole response in a reverberation chamber," *IEEE trans. Electromagn. Compat.*, vol. 41, no. 4, pp. 365-368, Nov. 1999.
- [26] O. Delangre, Ph. De Doncker, M. Lienard, and P. Degauque, "Delay spread and coherence bandwidth in reverberation chamber," *Electron. Lett.*, vol. 44, no. 5, Feb. 2008.
- [27] X. Chen, P.-S. Kildal, C. Orlenius, and J. Carlsson, "Channel sounding of loaded reverberation chamber for Over-the-Air testing of wireless devices - coherence bandwidth and delay spread versus average mode bandwidth," *IEEE Antennas Wireless Propag. Lett.*, vol. 8, pp. 678-681, 2009.
- [28] X. Chen and P.-S. Kildal, "Theoretical derivation and measurements of the relationship between coherence bandwidth and RMS delay spread in reverberation chamber," *EuCAP 2009*, Mar. 2009.
- [29] H. Fielitz, K. A. Remley, C. L. Holloway, Q. Zhang, Q. Wu, and D. W. Matolak, "Reverberation-chamber test environment for outdoor urban wireless propagation studies," *IEEE Antennas Wireless Propag. Lett.*, vol. 9, pp. 52-56, 2010.
- [30] K. Karlsson, X. Chen, P.-S. Kildal, and J. Carlsson, "Doppler spread in reverberation chamber predicted from measurements during step-wise stationary stirring," *IEEE Antennas Wireless Propag. Lett.*, vol. 9, pp. 497-500, 2010.
- [31] X. Chen, P.-S. Kildal, and J. Carlsson, "Determination of maximum Doppler shift in reverberation chamber using level crossing rate," *EuCAP 2011*, Rome, Italy, 11-15 April 2011.
- [32] C. L. Holloway, D. A. Hill, J. M. Ladbury, P. F. Wilson, G. Koepke, and J. Coder, "On the use of reverberation chamber to simulate a Rician radio environment for the testing of wireless devices," *IEEE Trans. Antennas Propag.*, vol. 54, No. 11, pp. 3167-3177, Nov. 2006.

- [33] C. Lemoine, E. Amador, and P. Besnier, "On the K-factor estimation for Rician channel simulated in reverberation chamber," *IEEE Trans. Antennas Propag.*, vol. 59, no. 3, pp. 1003-1012, Mar. 2011.
- [34] X. Chen, P.-S. Kildal, and S.-H. Lai, "Estimation of average Rician K-factor and average mode bandwidth in loaded reverberation chamber," *IEEE Antennas Wireless Propag. Lett.*, vol. 10, pp. 1437-1440, 2011.
- [35] P.-S. Kildal, X. Chen, C. Orlenius, M. Franzén, and C. Lötbäck Patané, "Characterization of reverberation chambers for OTA measurements of wireless devices: physical formulations of channel matrix and new uncertainty formula", accepted for publication in *IEEE Trans. Antennas Propag.*, 2012.
- [36] D. I. Wu and D. C. Chang, "The effect of an electrically large stirrer in a mode-stirred chamber," *IEEE Trans. Electromagn. Compat.*, vol. 31, no. 2, pp.164-169, May. 1989.
- [37] R. Vaughan and J. B. Andersen, *Channels, Propagation and Antennas for Mobile Communications*. London, U.K.: The Institution of Electrical Engineers, 2003.
- [38] U. G. Schuster, *Wireless Communication over Wideband Channels*, PhD thesis, ETH, 2009.
- [39] D. A. Hill, "Plane wave integral representation for fields in reverberation chambers," *IEEE Trans. Electromagn. Compat.*, vol. 40, no. 3, pp. 209–217, 1998.
- [40] X. Chen, P.-S. Kildal, and J. Carlsson, "Spatial correlations of incremental sources in isotropic environment such as reverberation chamber," *EuCAP 2011*, Rome, Italy, April 2011.
- [41] E. Amador, C. Lemoine, and P. Besnier, "Numerical study of spatial correlation in reverberation chamber," *Electron. Lett.*, vol. 47, no. 24, pp. 1319-1320, 2011.
- [42] G. L. Turin, "A statistical model of urban multipath propagation," *IEEE Trans. Veh. Technol.*, vol. 21, no.1, pp. 1-8, 1972.
- [43] A. A. M. Saleh and R. A. Valenzuela, "A statistical model for indoor multipath propagation," *IEEE J. Sel. Areas Commun.*, vol. 5, pp. 128-137, 1987.
- [44] P. A. Bello, "Characterization of randomly time-variant linear channels," *IEEE Trans. Commun. Syst.*, 360-393, Dec. 1963.
- [45] B. H. Fleury, "First- and second-order characterization of direction dispersion and space selectivity in the radio channel," *Trans. Inf. Theory*, vol. 46, no. 6, pp. 2027-2044, Sep. 2000.
- [46] W.C. Jakes, *Microwave Mobile Communications*, 2nd ed., Wiley, 1994.
- [47] W. C. Y. Lee, *Mobile Communications Engineering*. 2nd ed., New York: McGraw-Hill, 1997.
- [48] M. J. Gans, "A power-spectral theory of propagation in the mobile-radio environment," *IEEE Trans. Veh. Technol.*, vol. 21, no. 1, Feb. 1972.
- [49] T. S. Rappaport, *Wireless Communications—Principles and Practice*. 2nd ed., Prentice Hall PTR, 2002, pp.196-202.
- [50] A. Goldsmith, *Wireless Communications*, Cambridge University Press, 2005.
- [51] G. J. M. Janssen, P. A. Stigter, and R. Prasad, "Wideband indoor channel measurements and ber analysis of frequency selective multipath channels at 2.4, 4.75, and 11.5 GHz," *IEEE Trans. Commun.*, vol. 44, no. 10, pp. 1272-1288, Oct. 1996.
- [52] B. Sklar, "Rayleigh fading channel in mobile digital communication systems, Part I: characterization," *IEEE Commun. Mag.*, pp. 136-146, Sep., 1997.
- [53] M. H. Hayes, *Statistical Digital Signal Processing and Modeling*, John Wiley & Sons, Inc., 1996.
- [54] D. A. Hill, M. T. Ma, A. R. Ondrejka, B. F. Riddle, M. L. Crawford, and R. T. Johnk, "Aperture excitation of electrically large, lossy cavities," *IEEE Trans. Electromagn. Compat.*, vol.36, no. 3, pp.169-178, Aug. 1994.

- [55] X. Chen and P.-S. Kildal, "Relations between coherence bandwidth and average mode bandwidth in reverberation chamber for wireless device measurement," *ISAP'08*, Taipei, Oct. 27-30, 2008.
- [56] S. Stein, "Fading channel issues in system engineering," *IEEE J. Sel. Areas Commun.*, vol. 5, no. 2, pp. 68-89, Feb. 1987.
- [57] S. J. Howard and K. Pahlavan, "Doppler spread measurement of indoor radio channel," *Electron. Lett.*, vol. 26, no. 2, pp. 107-109, Jan. 1990.
- [58] Mehrez Souden, Sofiène Affes, Jacob Benesty, and Rim Bahroun, "Robust Doppler Spread Estimation in the Presence of a Residual Carrier Frequency Offset," *IEEE Trans. Signal Process.*, vol. 57, no. 10, Oct. 2009.
- [59] P. Hallbjörner and A. Rydberg, "Maximum Doppler frequency in reverberation chamber with continuously moving stirrer," *Loughborough Antenna Propag. Conf.*, 2007.
- [60] J. Yang, X. Chen, N. Wadefalk, and P.-S. Kildal, "Design and realization of a linearly polarized Eleven feed for 1-10 GHz," *IEEE Antennas Wireless Propag. Lett.*, vol. 8, pp. 64-68. 2009.
- [61] X. Chen and P.-S. Kildal, "Accuracy of antenna mismatch factor and input reflection coefficient measured in reverberation chamber," *EuCAP 2009*, Berlin, Germany, 23-27 Mar. 2009.
- [62] P.-S. Kildal, *Foundations of Antennas: A Unified Approach*, Studentlitteratur, 2000.
- [63] Y. Huang, R. M. Narayanan, and G. R. Kadambi, "Electromagnetic coupling effects on the cavity measurement of antenna efficiency," *IEEE Trans. Antennas Propag.*, vol. 51, no. 11, pp. 30647-3071, Nov. 2003.
- [64] L. K. Warne, K. S. H. Lee, H. G. Hudson, W. A. Johnson, R. E. Jorgenson, and S. L. Stronach, "Statistical properties of linear antenna impedance in an electrically large cavity," *IEEE Trans. Antennas Propag.*, vol. 51, no. 5, pp. 978-992, May. 2003.
- [65] P. -S. Kildal, C. Carlsson, and J. Yang, "Measurement of free-space impedance of small antennas in reverberation chamber," *Micro. Opt. Tech. Lett.*, vol. 32, no. 2, pp. 112-115, Jan. 20, 2002.
- [66] J. M. Ladbury and D. A. Hill, "Enhanced backscatter in a reverberation chamber: inside every complex problem is a simple solution struggling to get out," *IEEE Int. Symp. Trans. Electromagn. Compat.*, 2007, pp. 1-5.
- [67] S. M. Kay, *Fundamentals of Statistical Signal Processing: Estimation Theory*, volumn I: Estimation Theory, Prentice Hall, 1993.
- [68] D. A. Hill, "Electronic mode stirring for reverberation chamber," *IEEE trans. Electromagn. Compat.*, vol. 36, no. 4, pp. 294-299, Nov. 1994.
- [69] M. Schwartz, W. R. Bennet, and S. Stein, *Communication Systems and Techniques*. IEEE press, 1996.
- [70] D. G. Brennan, "Linear diversity combining techniques," *Proceedings of the IRE*, vol. 47, pp. 1075-1102, June, 1959.
- [71] W. C. Y. Lee, "Mutual coupling effect on maximum-ratio diversity combiners and application to mobile ratio," *IEEE Trans. Commun. Technol.*, vol. COM-18, pp. 779-791, Dec. 1970.
- [72] J. W. Wallace and M. A. Jensen, "Termination-dependent diversity performance of coupled antennas: network theory analysis," *IEEE Trans. Antennas Propag.*, vol. 52, no. 1, pp. 98-105, Jan. 2004.
- [73] J. Luo, J. R. Zeidler, and S. McLaughlin, "Performance analysis of compact antenna arrays with MRC in correlated Nakagami Fading channels," *IEEE Trans. Veh. Technol.*, vol. 50, no. 1, pp. 267-277, Jan. 2001.
- [74] D. Williams, *Probability with Martingales*. Cambridge University Press, 1991.

- [75] G. L. Turin, "The characteristics function of Hermitian quadratic forms in complex normal variables," *Biometrika*, vol. 47, 199-201, 1960.
- [76] T. M. Cover and J. A. Thomas, *Elements of Information Theory*, John Wiley & Sons, Inc., 1991.
- [77] A. Lapidoth, *A Foundation in Digital Communications*, Cambridge University Press, 2009.
- [78] S. Boyd and L. Vanderberghe, *Convex Optimization*, Cambridge University Press, 2004.
- [79] J. Yang, M. Pantaleev, P.-S. Kildal, Y. Karadikar, L. Helldner, B. Klein, N. Wadefalk, and C. Beaudoin, "Cryogenic 2-13 GHz Eleven feed for reflector antennas in future wideband radio telescopes," *IEEE Trans. Antennas Propag.*, vol. 59, no. 6, pp. 1918-1934, June, 2011.
- [80] M. T. Ivrlac and J. A. Nossek, "Diversity and correlation in Rayleigh fading MIMO channels," in *Proc. IEEE VTC*, May 2005, pp. 151-155.
- [81] A. J. Laub, *Matrix Analysis for Scientists and Engineers*: SIAM, 2005.
- [82] E. Jorswieck and H. Boche, *Majorization and Matrix-Monotone Functions in Wireless Communications*, Foundations and Trends Communications and Information Theory, vol. 3, no. 6, pp. 553-701, 2006.
- [83] Y. Fei, Y. Fan, B. K. Lau, and J. S. Thompson, "Optimal single-port matching impedance for capacity maximization in compact MIMO arrays," *IEEE Trans. Antennas Propagat.*, vol. 56, no. 11, pp. 3566-3575, Nov. 2008.
- [84] S. Lu, H. T. Hui, and M. Bialkowski, "Optimizing MIMO channel capacities under the influence of antenna mutual coupling," *IEEE Antennas Wireless Propag. Lett.*, vol. 7, pp. 287-290, 2008.
- [85] R. Janaswamy, "Effect of element mutual coupling on the capacity of fixed length linear arrays," *IEEE Antennas Wireless Propag. Lett.*, vol. 1, pp. 157-160, 2002.
- [86] C. Oestges and B. Clerckx, *MIMO Wireless Communications: from Real-World Propagation to Space-Time Code Design*. Academic Press, 2007.
- [87] B. T. Quist and M. A. Jensen, "Optimal antenna radiation characteristics for diversity and MIMO systems," *IEEE Trans. Antennas Propag.*, vol. 57, no. 11, pp. 3474-3481, Nov. 2009.
- [88] M. T. Ivrlac and J. A. Nossek, "Toward a circuit theory of communication," *IEEE Trans. Circuits Syst.*, vol. 57, no. 7, Jul. 2010.
- [89] X. Chen, P.-S. Kildal, and J. Carlsson, "Simple calculation of ergodic capacity of lossless two-port antenna system using only S-parameters – comparison with common Z-parameter approach," *IEEE Int. Symp. Antennas and Propag.*, Spokane, USA, 3-8 July, 2011, pp. 1885-1888..
- [90] D.-S. Shiu, G. J. Foschini, M. J. Gans, and J. M. Kahn, "Fading correlation and its effect on the capacity of multielement antenna systems," *IEEE Trans. Commun.*, vol. 48, pp. 502-513, Mar. 2000.
- [91] C.-N. Chuah, J. M. Kahn, and D. N. C. Tse, "Capacity scaling in MIMO wireless systems under correlated fading," *IEEE Trans. Inf. Theory*, vol. 48, no. 3, pp. 637-650, Mar. 2002.
- [92] D. Gesbert, H. Bölcskei, D. A. Gore, and A. J. Paulraj, "Outdoor MIMO wireless channels: models and performance prediction," *IEEE Trans. Commun.* vol. 50, no. 12, pp. 1926-1934, Dec. 2002.
- [93] R. Janaswamy, *Radiowave Propagation and Smart Antennas for Wireless Communications*, Kluwer Academic Publishers, 2001.

- [94] P.-S. Kildal and K. Rosengren, "Electromagnetic analysis of effective and apparent diversity gain of two parallel dipoles", *IEEE Antennas Wireless Propag. Lett.*, vol. 2, no. 1, pp 9-13, 2003.
- [95] C. A. Balanis, *Antenna Theory: Analysis and Design*, 3rd edition, John Wiley & Sons, 2005.
- [96] W. Wasylkiwskyj and W. K. Kahn, "Theory of mutual coupling among minimum-scattering antennas", *IEEE Trans. Antennas Propag.*, vol. 18, no. 2, pp. 204-216, Mar. 1970.
- [97] X. Chen, P.-S. Kildal, and J. Carlsson, "Comparisons of different methods to determine correlation applied to multi-port UWB eleven antenna," *EuCAP 2011*, Rome, Italy, 11-15 April 2011.
- [98] W. F. Tsen and H.-J. Li, "Uncoupled impedance matching for capacity maximization of compact MIMO arrays," *IEEE Antennas Wireless Propag. Lett.*, vol. 8, pp. 1295-1298, 2009.
- [99] S. Stein, "On cross coupling in multiple-beam antennas," *IRE Trans. Antennas Propag.*, pp. 548-557, Sep. 1962.
- [100] S. Blanch, J. Romeu, and I. Corbella, "Exact representation of antenna system diversity performance from input parameter description," *Electron. Lett.*, vol. 39, no. 9, pp. 705-707, May 2003.
- [101] J. Thaysen and K. B. Jakobsen, "Envelope correlation in (N, N) MIMO antenna array from scattering parameters," *Microw. Opt. Tech. Letters*, vol. 48, no. 5, pp. 832-834, May 2006.
- [102] A.A.H. Azremi, J. Toivanen, T. Laitinen, P. Vainikainen, X. Chen, N. Jamaly, J. Carlsson, P.-S Kildal, and S. Pivnenk, "On diversity performance of two-element coupling element based antenna structure for mobile terminal", *EuCAP 2010*, Barcelona, Spain, 2011.
- [103] P.-S. Kildal and C. Carlsson, *TCP of 20 Mobile Phones Measured in Reverberation Chamber*, Bluetest Technical Report, 2002.
- [104] S. Pivnenko, *Private communications*, Technical University of Denmark, Lyngby, Denmark, 2011.
- [105] G. Levin and S. Loyka, "From multi-keyholes to measure of correlation and power imbalance in MIMO channels: outage capacity analysis," *IEEE Trans. Inf. Theory*, vol. 57, no. 6, pp. 3515-3529, Jun. 2011.
- [106] X. Chen, P.-S. Kildal, and J. Carlsson, "Measurement uncertainties of capacities of multi-antenna system in anechoic chamber and reverberation chamber," *IEEE ISWCS*, Aachen, Germany, Nov. 2011, pp. 216-220.
- [107] C. Orlenius, P. S. Kildal, and G. Poilasne, "Measurements of total isotropic sensitivity and average fading sensitivity of CDMA phones in reverberation chamber," *IEEE Int. Symp. Antennas and Propag.*, 3-8 July 2005.
- [108] E. Genender, C. L. Holloway, K. A. Remley, J. M. Ladbury, G. Koepke, and H. Garbe, "Simulating the multipath channel with a reverberation chamber: application to bit error rate measurements," *IEEE Trans. Electromagn. Compat.*, vol. 52, pp. 766-777, 2010.
- [109] N. Prasad and M. K. Varanasi, "Outage theorems for MIMO block-fading channels," *IEEE Trans. Inf. Theory*, vol. 58, no. 7, pp. 2159-2168, July 2010.
- [110] D. Costello, J. Hagenauer, H. Imai, and S. B. Wicker, "Applications of error-control coding," *Trans. Inf. Theory*, vol. 44, no. 6, pp. 2531-2560, Oct. 1998.
- [111] P. Jung and J. J. Blanz, "Joint detection with coherent receiver antenna diversity in CDMA mobile radio systems," *IEEE Trans Veh. Technol.*, vol. 44, no. 1, pp. 76-88, Feb. 1995.

- [112] L.J. Cimini, Jr., "Analysis and simulation of a digital mobile channel using orthogonal frequency division multiplexing," *IEEE Trans. Commun.*, vol. 33, no. 7, pp. 665–675, Jul. 1985.
- [113] A. Toyserkani, E. Strom, and A. Svensson, "An analytical approximation to the block error rate in Nakagami-m non-selective block fading channels," *IEEE Trans. Wireless Commun.*, vol. 9, pp. 1543-1546, 2010.
- [114] Z. Kang, K. Yao, and F. Lorenzelli, "Nakagami-m fading modeling in the frequency domain for OFDM system analysis," *IEEE Commun. Lett.*, vol. 7, no. 10, pp. 484–486, Oct. 2003.
- [115] S. Alamouti, "A simple transmit diversity technique for wireless communications," *IEEE J. Sel. Areas Commun.*, vol. 16, no. 8, pp. 1451-1458, Oct. 1998.
- [116] K. Madsen, P. Hallbjorner, and C. Orlenius, "Models for the number of independent samples in reverberation chamber measurements with mechanical, frequency, and combined stirring," *IEEE Antennas Wireless Propag. Lett.*, vol. 3, pp. 48-51, 2004.
- [117] P.-S. Kildal, S. Lai, and X. Chen, "Direct coupling as a residual error contribution during ota measurements of wireless devices in reverberation chamber", *IEEE AP-S*, Charleston, USA, June, 2009.
- [118] R. G. Vaughan, "Polarization diversity in mobile communications," *IEEE Trans Veh. Technol.*, vol. 39, no. 3, pp. 177-186, Aug. 1990.
- [119] N. Wellander, O. Lunden, and M. Bäckström, "Experimental investigation and mathematical modeling of design parameters for efficient stirrers in mode-stirred reverberation chambers," *Trans. Electromagn. Compat.*, vol. 49, no. 1, pp. 94-103, 2007.
- [120] P. Corona, G. Ferrara, and M. Migliaccio, "Reverberating chamber electromagnetic field in presence of an unstirred component," *IEEE Trans. Electromagn. Compat.*, vol. 42, no. 2, pp. 111-115, 2000.
- [121] A. Sorrentino, P. S. Kildal, U. Carlberg, and E. Pucci, "Accuracy in reverberation chamber for wireless testing: simple formulas for the number of independent samples," *EuCAP 2009*, Berlin, Germany, Mar. 2009, pp. 2673-2677.
- [122] L. J. Greenstein, D. G. Michelson, and V. Erceg, "Moment-method estimation of the Ricean K-factor," *IEEE Commun. Lett.*, vol. 3, pp. 175-176, June 1999.
- [123] C. Tepedelenlioglu, A. Abdi, and G. B. Giannakis, "The Ricean K-factor: estimation and performance analysis," *IEEE Trans. Wireless Commun.*, vol. 2, no. 4, pp.799-810, July 2003.
- [124] X. Chen and P.-S. Kildal, "Frequency-dependent effects of platform and wall antenna stirring on measurement uncertainty in reverberation chamber", *EuCAP 2010*, Barcelona, Spain, April 2010.